Supporting Information

Chemically Robust Functionalized Covalent Organic Framework for Highly Efficient and Selective Separation of Bromine

Sahel Fajal,[a] Dipayan Ghosh,[a] Kishalay Biswas,[a] Writakshi Mandal,[a] Nayan Sarkar,[a] Gourab K. Dam,[a] Anirban Roy,[a] Antak Roychowdhury,[a] Dipanjan Majumder,[a] Rajashri R. Urkude,[b] Mandar M. Shirolkar,[c,d] Sujit K. Ghosh*[a,e]

[a]Department of Chemistry, Indian Institute of Science Education and Research (IISER) Pune, Dr. Homi Bhaba Road, Pashan, Pune 411 008, India.

[b]Beamline Development and Application Section Bhabha Atomic Research Centre, Mumbai – 400085.

[c]Advanced Bio-Agro Tech Pvt. Ltd, Baner, Pune 411045, India.

[d]Norel Nutrient Bio-Agro Tech Pvt. Ltd, Baner 411045 India.

[e]Centre for Water Research (CWR), Indian Institute of Science Education and Research (IISER) Pune, Dr. Homi Bhabha Road, Pashan, Pune 411 008, India.

Email Corresponding Author: sghosh@iiserpune.ac.in

Table of Contents

Section S1: Materials, General Characterizations and Physical Measurements

S1.1. Materials: All the reagents, starting materials and solvents were commercially purchased from Sigma-Aldrich, TCI Chemicals, depending on their availability and used without further purification.

S1.2. Safety Note: Bromine vapor is carcinogenic in nature and proper protective gear (masks, gloves) is always to be used. The bromine capture protocol described in this article must be carried out under strict safety precautions.

S1.3. General Characterizations and Physical Measurements:

S1.3.1. Powder X-ray diffraction (PXRD): Powder X-ray diffraction (PXRD) experiments were performed on a Bruker D8 Advanced X-ray diffractometer at room temperature using Cu Kα radiation (λ = 1.5406 Å) at a scan speed of 0.5 ° min^{-1} and a step size of 0.01° in 2θ.

S1.3.2. Fourier transform infrared spectroscopy (FT-IR): The FT-IR spectra were acquired by using NICOLET 6700 FT-IR spectrophotometer using KBr pellet in 500-4000 cm^{-1} range. FT-IR data are reported with a wave number (cm^{-1}) scale in 500-4000 cm^{-1} range.

S1.3.3. Thermogravimetric analysis (TGA): Thermogravimetric analyses were recorded on Perkin-Elmer STA 6000 TGA analyzer by heating the samples from 40 to 800 ℃ under N_2 atmosphere with a heating rate of 10 ℃ min^{-1}.

S1.3.4. Field emission scanning electron microscopy (FESEM): The morphology of the materials was recorded with a Zeiss Ultra Plus field-emission scanning electron microscope (FESEM) with an integral charge compensator and embedded EsB and AsB detectors (Oxford X-max instruments 80 mm^2 (Carl Zeiss NTS, GmbH). The samples were sputter-coated with a 5-10 nm Au film to reduce charging. The elemental analysis was carried out using voltage of 15 KV equipped with an EDX detector. Data acquisition was performed with an accumulation time of >600s.

S1.3.5. Transmission electron microscopy (TEM): TEM, High-resolution TEM imaging and STEM-EDS were performed on the HRTEM (JEM-2200FS, JEOL) operating at acceleration voltage of 200 kV. For TEM analysis, all the samples were dispersed in isopropanol (0.5 mg/mL) and sonicated for 15 min. Then, the samples were left for 2 min, and the upper part of the solution was taken for preparing TEM samples on a lacey carbon-coated copper grid (Electron Microscopy Science, 200 mesh).

S1.3.6. Solid-state nuclear magnetic resonance (NMR) spectroscopy: Solid-state ^{13}C cross-polarization-magic angle spinning (CP-MAS) spectra were conducted on a Bruker 500 MHz NMR spectrometer with a CP-MAS probe. Carbon chemical shifts are expressed in parts per million (δ scale).

S1.3.7. Nitrogen adsorption-desorption isotherm measurements: N_2 gas adsorption-desorption measurements were performed using BelSorp-Max instrument (Bel Japan). Prior to adsorption measurements, the activated samples were heated at 120 °C under vacuum for 12 hours using BelPrepvacII. The pore size distributions were calculated using NLDFT model.

S1.3.8. UV-visible absorption spectra: UV-vis absorption studies were performed on a Shimadzu UV 3600 UV /vis /NIR spectrophotometer in an optical quartz cuvette (10 mm path length) over the entire range of 200-800 nm.

S1.3.9. X-ray photoelectron spectroscopy (XPS): As-obtained powder samples was stuck to conductive paste and then measured by X-ray photoelectron spectroscopy using K-Alpha+model (Thermo Fischer Scientific, UK) with Al Kα source.

S1.3.10. Raman measurements: Raman spectra were acquired with an Xplora PLUS Raman microscope (Horiba Company) (785 nm laser and a 1200 lines/mm grating).

S1.3.11. Raman mapping analysis: Raman mapping images were acquired with a Renishaw, UK model-Invia Reflex make Raman microscope. Spectrograph equipped with a research-grade microscope capable of producing Raman (wavenumber transfer 50 to 4000 cm^{-1}) and PL (330 nm to 1.6 microns). Spectral Range of spectrometer: 200 nm – 1600 nm. (Excited with 830 nm laser, objective 50x, exposer time 15 sec. and laser power 10%).

S1.3.12. Conductivity measurement: Four probe DC conductivity measurements were done on pressed pellets of compounds in Keithley 6221 source meter instrument.

S1.3.13. Steady state photoluminescence spectra: The steady-state photoluminescence studies were recorded on a Fluorolog-3 spectrofluorometer (HORIBA Scientific).

S1.2.14 Inductively coupled plasma mass spectrometry (ICP-MS): ICP-MS was performed on Quadrupole inductively coupled plasma mass spectrometry (Q-ICP MS; Thermo Scientific iCAP Q) instrument.

Section S2: Detailed procedures for synthetic preparation

S2.1 Synthesis of 2-hydroxybenzene-1,3,5-tricarbaldehyde (HTA): HTA was synthesized by following a previously reported procedure (Figure S1).[1] A mixture of phenol (3.6 g, 38.2 mmol) and hexamethylenetetramine (11.8 g, 84.2 mmol) was dissolved in trifluoroacetic acid (35 mL) under a nitrogen atmosphere. The mixture was stirred at 130 °C for 16 h, and then heated to 150 °C for 3h. After being cooled to 120 °C, the mixture was treated with HCl (aq., 4 M, 50 mL) and then heated at 105 °C for another 30 min. The crude products were filtered and washed with water. After being recrystallized from dimethyl formamide, HTA was collected as a pink solid. The product was characterized by ^{1}H NMR (DMSO-d6, 400 MHz): δ 10.33 (s, 2H), 10.01 (s, 1H) and 8.54 (s, 2H) (Figures S90).
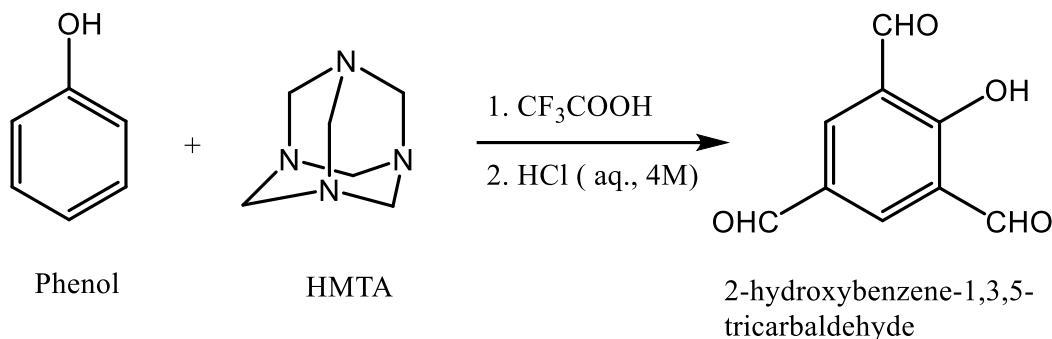
Figure S1: Synthesis scheme of 2-hydroxybenzene-1,3,5-tricarbaldehyde (1-OH).

S2.2 Synthesis 2,4-dihydroxybenzene-1,3,5-tricarbaldehyde (DHTA): DHTA was synthesized by following a previously reported procedure (Figure S2).[1] A mixture of 3.6 g (32.7 mmol) of resorcinol and 10 g (71.3 mmol) of hexamethylenetetramine (HMTA) was dissolved in trifluoroacetic acid (35 mL) under a nitrogen atmosphere. The mixture was stirred at 130 °C for 16 h, and then heated to 150 °C for 3h. After being cooled to 120 °C, the mixture was treated with HCl (aq., 3M, 55 mL) and then heated at 105 °C for another 30 min. The crude products were filtered and washed with water. After being recrystallized from dimethyl formamide, DHTA was collected as a pale yellow solid. The product was characterized by ^{1}H NMR (DMSO-d6, 400 MHz): δ 10.27 (s, 1H), 10.09 (s, 2H) and 8.40 (s, 1H) (Figures S91).
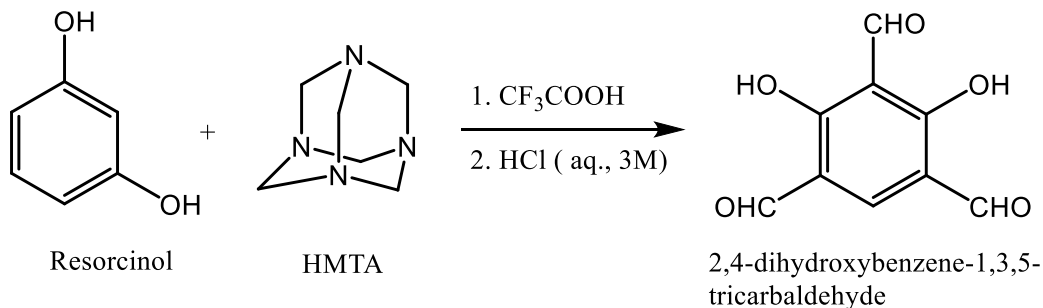
Figure S2: Synthesis scheme of 2,4-dihydroxybenzene-1,3,5-tricarbaldehyde (2-OH).

S2.3 Synthesis of 2,4,6-trihydroxybenzene-1,3,5-tricarbaldehyde (THTA): THTA was synthesized by following a previously reported procedure (Figure S3).[2] A mixture of 10.0 g (79.3 mmol) phloroglucinol 22.3 g (158.6 mmol) hexamethylenetetramine and were dissolved in trifluoroacetic acid (60 mL) under an argon atmosphere. The reaction mixture was heated at 100 °C for 2.5 h, then added HCl (3 M, 200 mL) and heated at 100 °C for another 1 h. After being cooled to room temperature, the solution was filtered through Celite, extracted with dichloromethane (3×150 mL), dried over sodium sulfate, and filtered. Rotary evaporation of the solution afforded an organic powder. The product was characterized by ^{1}H NMR (DMSO-d6, 400 MHz): δ 10.02 (s, 3H), (Figures S92).
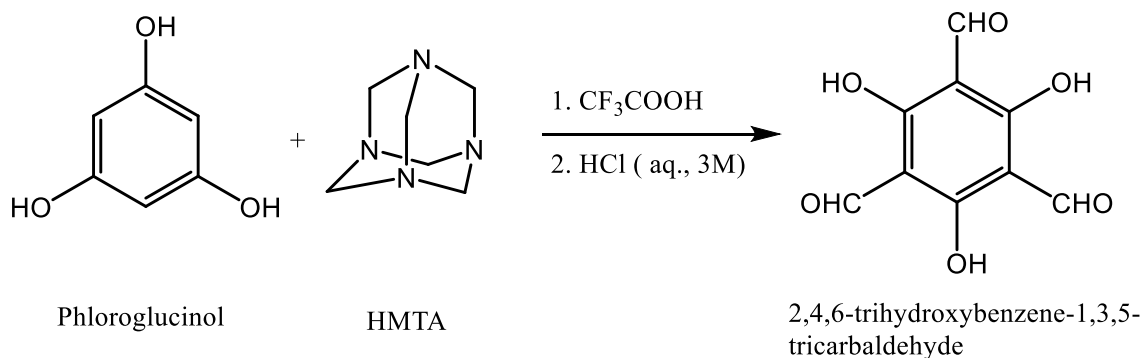
Figure S3: Synthesis scheme of 2,4,6-trihydroxybenzene-1,3,5-tricarbaldehyde (3-OH).

S2.4 Synthesis of 2,4,6-tris(4-aminophenyl)-1,3,5-triamine (TAPT): 2,4,6-tris(4-aminophenyl)-1,3,5-triamine was synthesized from 4-aminobenzonitrile via an acid catalyzed trimerization reaction by following a previously reported protocol (Figure S4).[3] In a typical synthesis, 0.772 g (6.538 mmol) 4-aminobenzonitrile was taken in a round bottom flask at 0 ºC. Then 2 mL (22.2 mmol) trifluoromethanesulfonic acid was added dropwise for 20 min maintaining the temperature at 0 ºC. The resultant mixture was stirred for 24 h at room temperature in inert atmosphere. After that, 20 mL distilled water was added to the mixture and it was neutralized by adding 2M NaOH solution until the pH reaches to 7. Initially, with increase in pH, the orange precipitate dissolves to give a bright orange solution, which upon further increase in pH gives a pale-yellow precipitate. The resultant pale-yellow product was filtered and washed several times with distilled water. The product was characterized by ^{1}H NMR (DMSO-d6, 400 MHz): δ 8.34 (d J = 4 Hz, 6H), 6.67 (d J = 4 Hz, 6H), 5.91 (6H) (Figures S93).
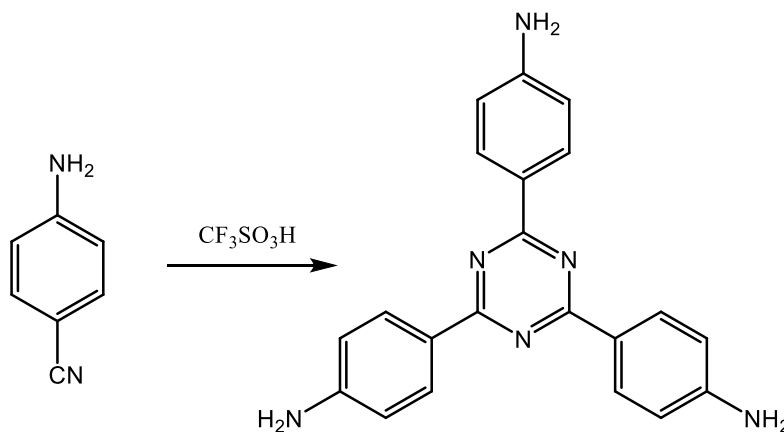
Figure S4: Synthesis scheme of 4,4',4''-(1,3,5-triazine-2,4,6-triyl)trianiline.

S2.5 Synthesis of COF-1: COF-1 was synthesized by following a previously reported procedure with slight modification.[4] In a typical synthetic procedure a 20 mL of pyrex tube was charged with 26.72 mg (0.15 mmol) of 2-hydroxybenzene-1,3,5-tricarbaldehyde (HTA) and 53.17 mg (0.15 mmol) of 2,4,6-tris(4-aminophenyl)-1,3,5-triamine (TAPT). Then 2.5 mL of mesitylene and 2.5 mL of dioxane along with 0.5 mL of 6 M acetic acid were added to the mixture. After that, the tube was sonicated for 15 minutes in order to get a homogenous dispersion. Then the tube was flash frozen at 77 K (liquid N_2 bath) and degassed. Thereafter, the tube was sealed and heated at 120 °C for 3 days. After 3 days, the sealed tube was taken out to obtain deep red-color material. The collected product was then washed with dry solvents like methanol, acetone and THF (each for three times with ~10 mL) for a certain period. Again, it was washed with THF in a Soxhlet extractor for 12-18 h. Finally, the product dried at 120 °C for 6 hours.
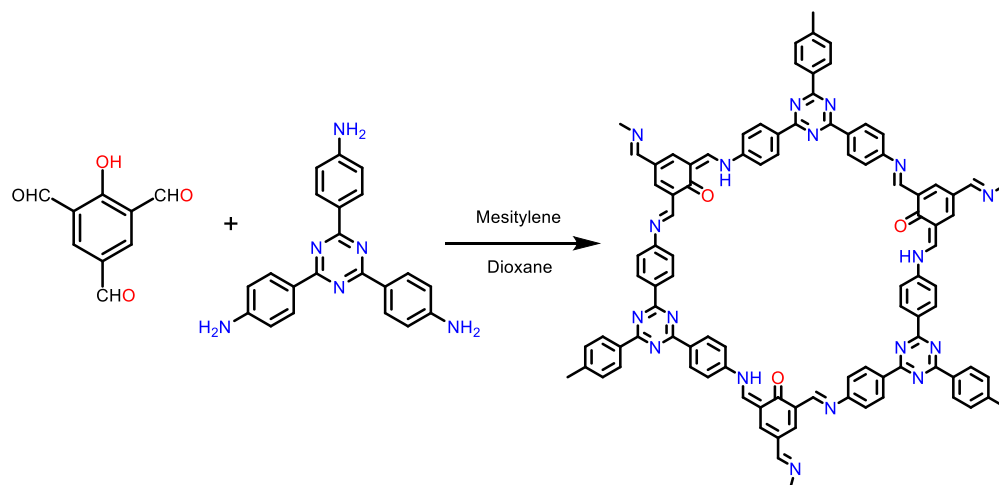
Figure S5: Synthesis scheme of COF-1.

S2.6 Synthesis of COF-2: COF-2 was synthesized by following a previously reported procedure with slight modification.[4] In a typical synthetic procedure a 20 mL of pyrex tube was charged with 29.12 mg (0.15 mmol) of 2,4-dihydroxybenzene-1,3,5-tricarbaldehyde (DHTA) and 53.17 mg (0.15 mmol) of 2,4,6-tris(4-aminophenyl)-1,3,5-triamine (TAPT). Then 2.5 mL of mesitylene and 2.5 mL of dioxane along with 0.5 mL of 6 M acetic acid were added to the mixture. After that, the tube was sonicated for 15 minutes in order to get a homogenous dispersion. Then the tube was flash frozen at 77 K (liquid N_2 bath) and degassed. Thereafter, the tube was sealed and heated at 120 °C for 3 days. After 3 days, the sealed tube was taken out to obtain red-brown color material. The collected product was then washed with dry solvents like methanol, acetone and THF (each for three times with ~10 mL) for a certain period. Again, it was washed with THF in a Soxhlet extractor for 12-18 h. Finally, the product dried at 120 °C for 6 hours.
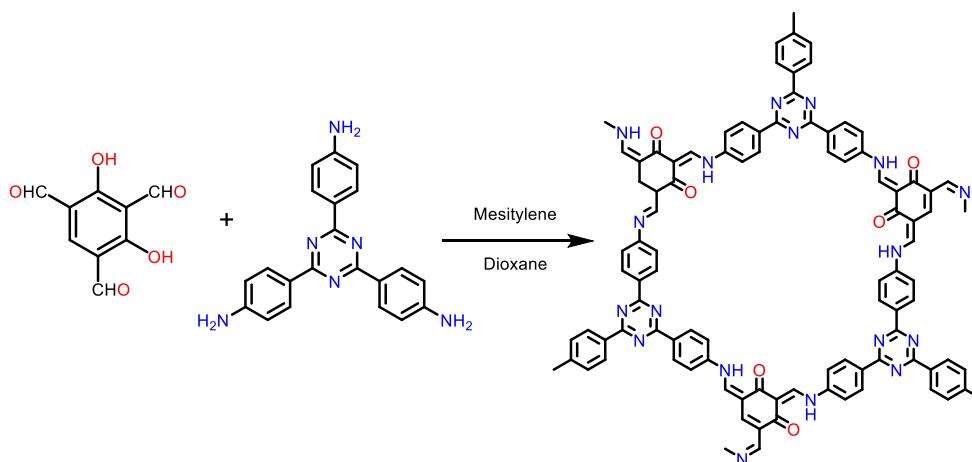
Figure S6: Synthesis scheme of COF-2.

S2.7 Synthesis of COF-3: COF-3 was synthesized by following a previously reported procedure with slight modification.[5] In a typical synthetic procedure a 20 mL of pyrex tube was charged with 31.52 mg (0.15 mmol) of 2,4,6-trihydroxybenzene-1,3,5-tricarbaldehyde (THTA) and 53.17 mg (0.15 mmol) of 2,4,6-tris(4-aminophenyl)-1,3,5-triamine (TAPT). Then 2.5 mL of mesitylene and 2.5 mL of dioxane along with 0.5 mL of 6M acetic acid were added to the mixture. After that, the tube was sonicated for 15 minutes in order to get a homogenous dispersion. Then the tube was flash frozen at 77 K (liquid N_2 bath) and degassed. Thereafter, the tube was sealed and heated at 120 °C for 3 days. After 3 days, the sealed tube was taken out to obtain brown color material. The collected product was then washed with dry solvents like methanol, acetone and THF (each for three times with ~10 mL) for a certain period. Again, it was washed with THF in a Soxhlet extractor for 12-18 h. Finally, the product dried at 120 °C for 6 hours.
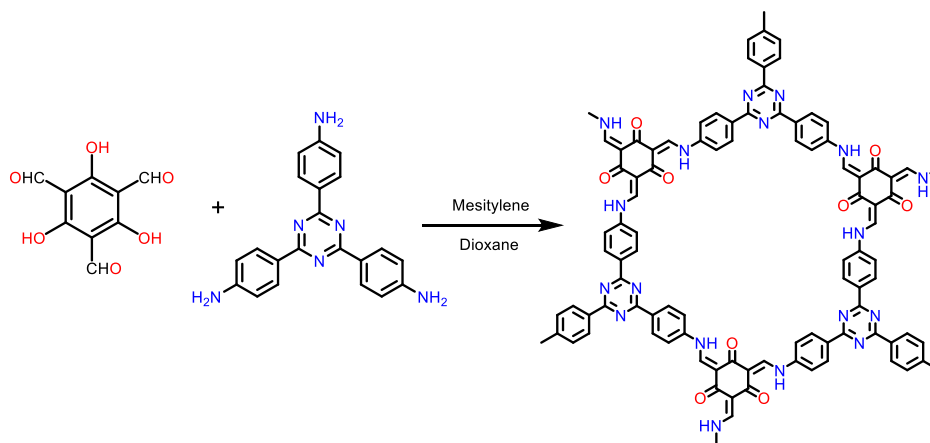
Figure S7: Synthesis scheme of COF-3.

Section S3: Characterizations of the materials
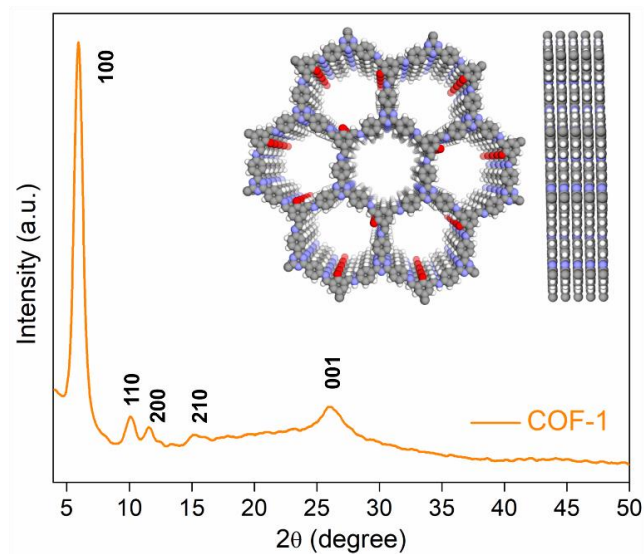
Figure S8: PXRD profile of COF-1. The crystallinity of COF-1 was verified through PXRD analysis, revealing a distinct peak at $2\theta = 5.9$, followed by small peaks at 10.1, 11.5, 15.2, and 26 which corresponds to the reflection from 100, 110, 200, 210, and 001 facets, respectively.
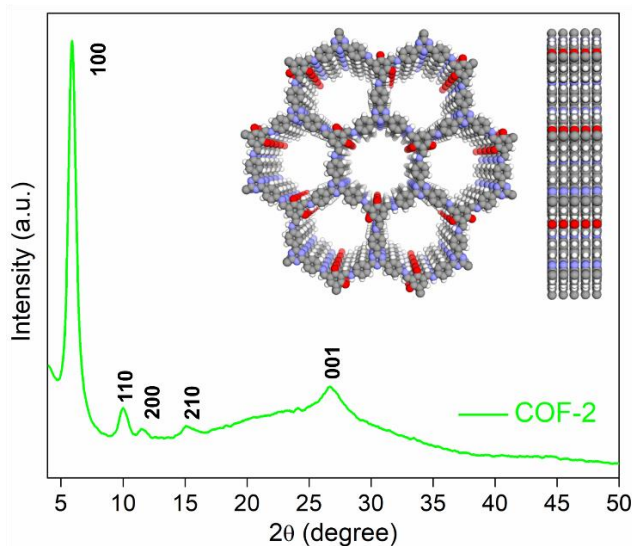
Figure S9: PXRD profile of COF-2. PXRD analysis of COF-2 revealed a distinct peak at $2\theta = 5.57$, followed by small peaks at 9.71, 11.19, 14.68, and 26.49, which corresponds to the reflection from 100, 110, 200, 210, and 001 facets, respectively.
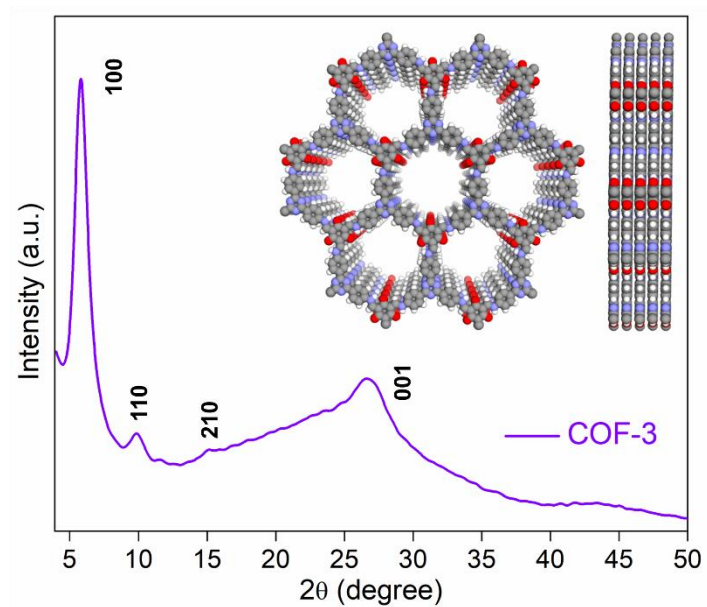
Figure S10: PXRD profile of COF-3. PXRD analysis of COF-3 also revealed a distinct peak at 2θ = 5.8, followed by small peaks at 9.9, 11.5, 15, and 26.6, which corresponds to the reflection from 100, 110, 200, 210, and 001 facets, respectively.

Supporting note 1: Furthermore, the formation of the covalently linked insoluble frameworks via successful Schiff-base condensation reaction was verified by Fourier transform infrared spectroscopy (FT-IR), solid-state ^{13}C cross-polarization magic-angle-spinning nuclear magnetic resonance (CP-MAS NMR), and X-ray photoelectron spectroscopy (XPS) analysis. FT-IR spectra of these COFs indicated appearance of signal at ~1676 cm^{-1} (characteristic peak for imine –C=N- stretching bands) and disappearance of signals at 1687 cm^{-1} and 3212-3468 cm^{-1}, corresponds to aldehyde and primary amine groups, respectively (Figure S11-S13).[6,7] This result suggests the formation of extended polymeric networks via covalent bond formation between the aldehydes and amines.
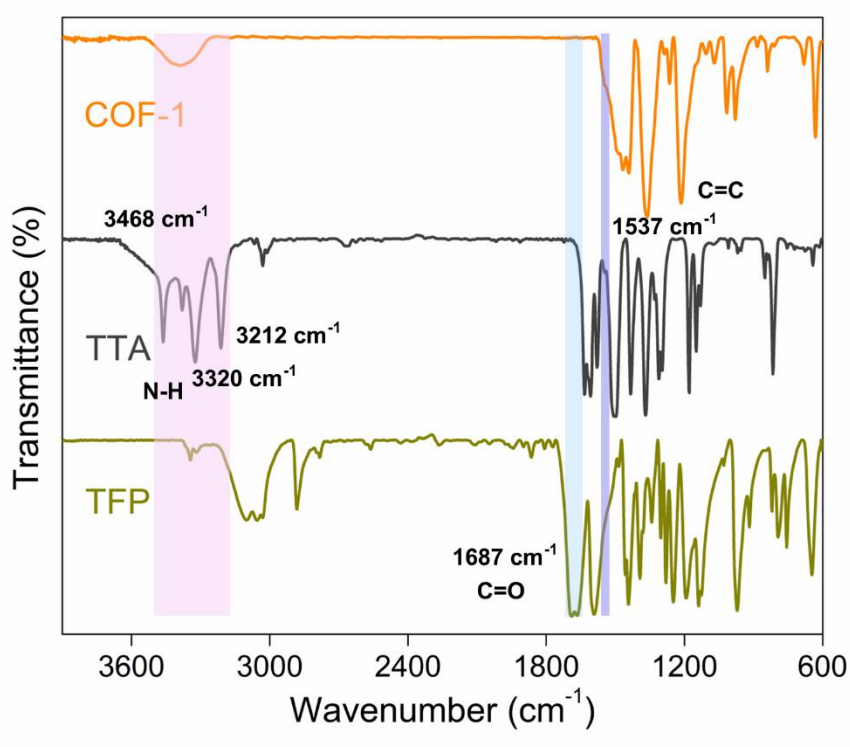
Figure S11: The FT-IR spectra of COF-1 with its corresponding precursors. The disappearance of N–H stretching signals (primary amine –NH$_2$) at ~3468, ~3320, and ~3212 cm^{-1}, coupled with the disappearance of aldehyde (-C=O) stretching signals at ~1687-1640 cm^{-1}, alongside the emergence of imine bond signal at ~1676 cm^{-1}, indicating that the condensation reactions between tri-aldehyde and tri-amines. The newly formed C=O and C=C stretching bands were merged into a single peak at near ~1610-1540 cm^{-1} for COF-1, whereas the C=O peak at ~1606 cm^{-1} was merged with the C=C stretching band at ~1585.6 cm^{-1} to give a shoulder peak for COF-1.
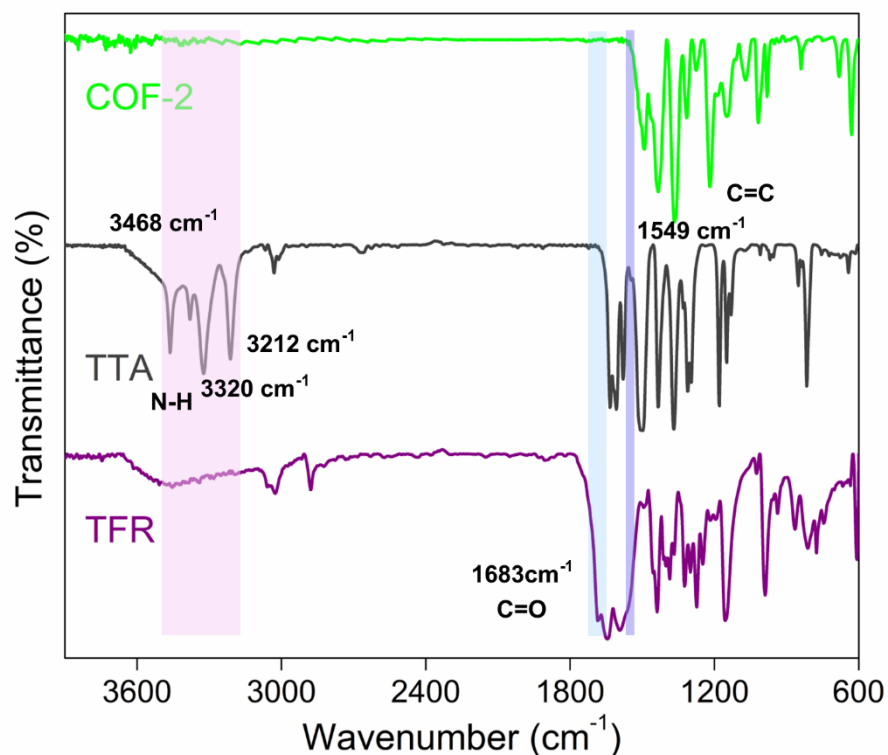
Figure S12: The FT-IR spectra of COF-2 with its corresponding precursors. The disappearance of N–H (primary amine –NH_2) stretching at ~3468, ~3320, and ~3212 cm^{-1}, along with the disappearance of aldehyde stretching signals (-C=O) stretching signals at ~1683-1641 cm^{-1}, alongside the emergence of imine bond signal at ~1676 cm^{-1}, indicating that the condensation reactions between tri-aldehyde and tri-amines. The newly formed C=O and C=C stretching bands were merged into a single peak at near ~1610-1540 cm^{-1} for COF-2, whereas the C=O peak at ~1605.8 cm^{-1} was merged with the C=C stretching band at ~1584.7 cm^{-1} to give a shoulder peak for COF-2.
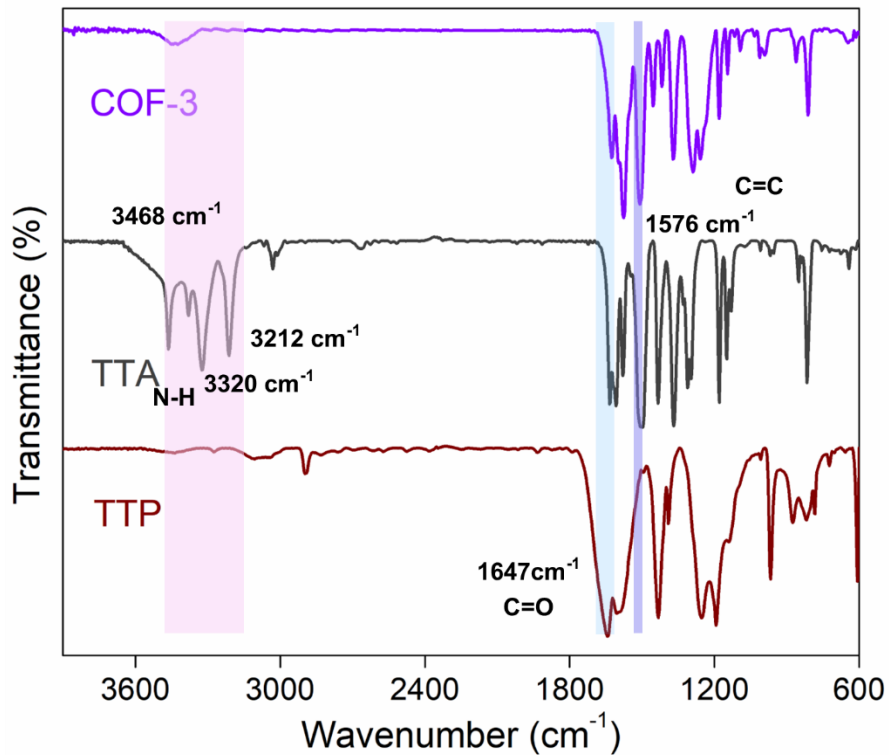
Figure S13: The FT-IR spectra of COF-3 with its corresponding precursors. The disappearance of N–H (primary amine –NH$_2$) stretching at ~3468, ~3320, and ~3212 cm^{-1}, along with the disappearance of aldehyde stretching signals (-C=O) stretching signals at ~1683-1641 cm^{-1}, alongside the emergence of imine bond signal at ~1676 cm^{-1}, indicating that the condensation reactions between tri-aldehyde and tri-amines. In addition, the appearance of stretching frequency at ~1626 cm^{-1} originates from the carbonyl group, which reveals its existence in the keto form.

Supporting note 2: The appearance of distinctive resonance peaks of imine carbons at ~158.9 and ~156.1 ppm and the absence of peaks at about ~190 ppm corresponding to the aldehyde carbon in the solid-state ^{13}C CP-MAS NMR spectra of the COFs further validated their formation of the proposed structures (Figure S14-S17).[4] Furthermore, to verify the construction of β-ketoenamine COFs, and the incorporation of all the desired functional groups within the backbone of these COFs, in-details FT-IR and ^{13}C CP-MAS NMR discussion has been provided in Figure S11-S17.
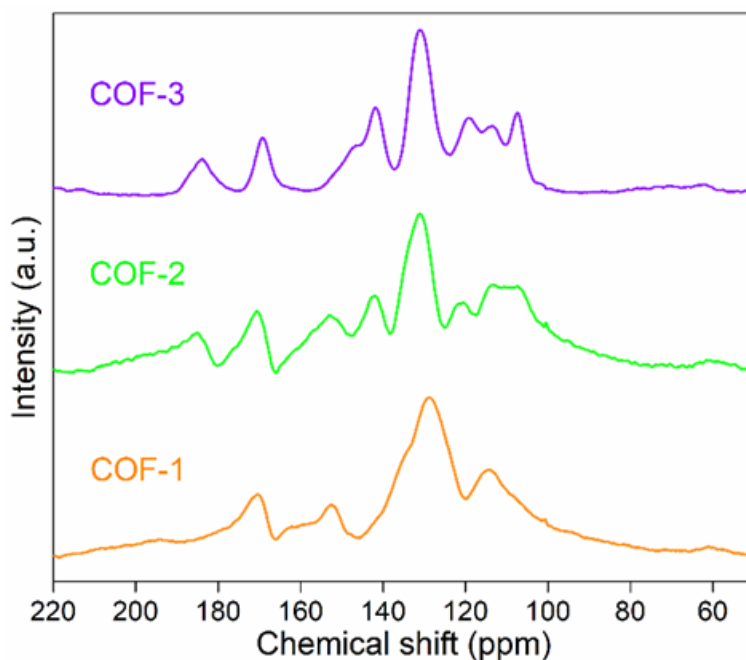
Figure S14: The solid-state ^{13}C CP-MAS NMR spectra of COF-1, COF-2 and COF-3.
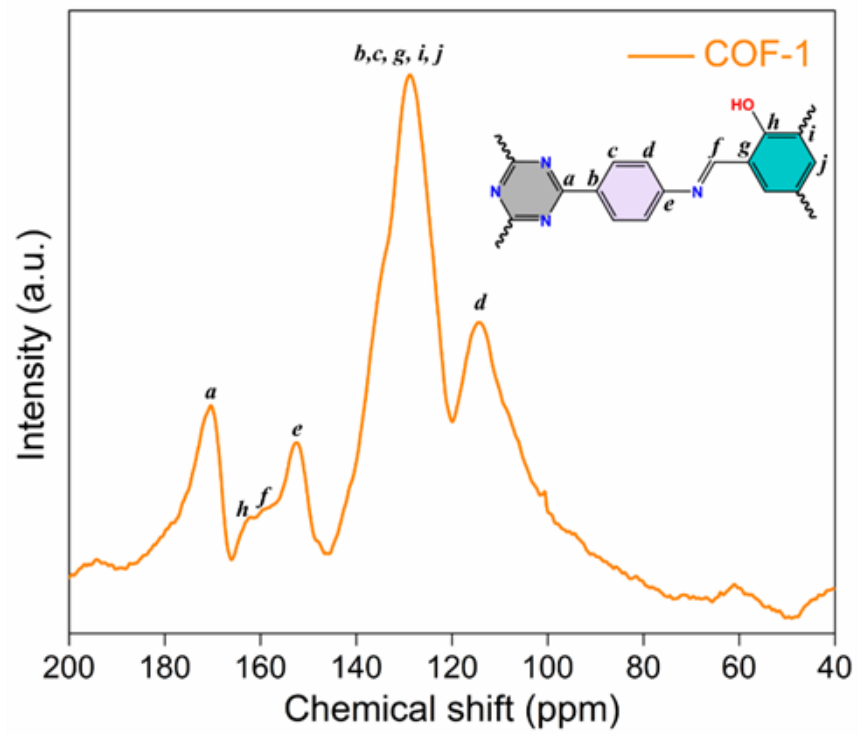
Figure S15: The solid-state ^{13}C CP-MAS NMR spectra of COF-1 exhibit distinct peaks, ~158.9 and ~161.1 ppm, attributed to the resonance peaks of imine carbon (-C=N) and Csp^2-OH carbons, respectively. Additionally, peaks at ~170 ppm originate from the triazine core of the frameworks, while the absence of aldehyde (-CH=O) resonance peaks at ~190 ppm validate the formation of COF.[1,3-5]
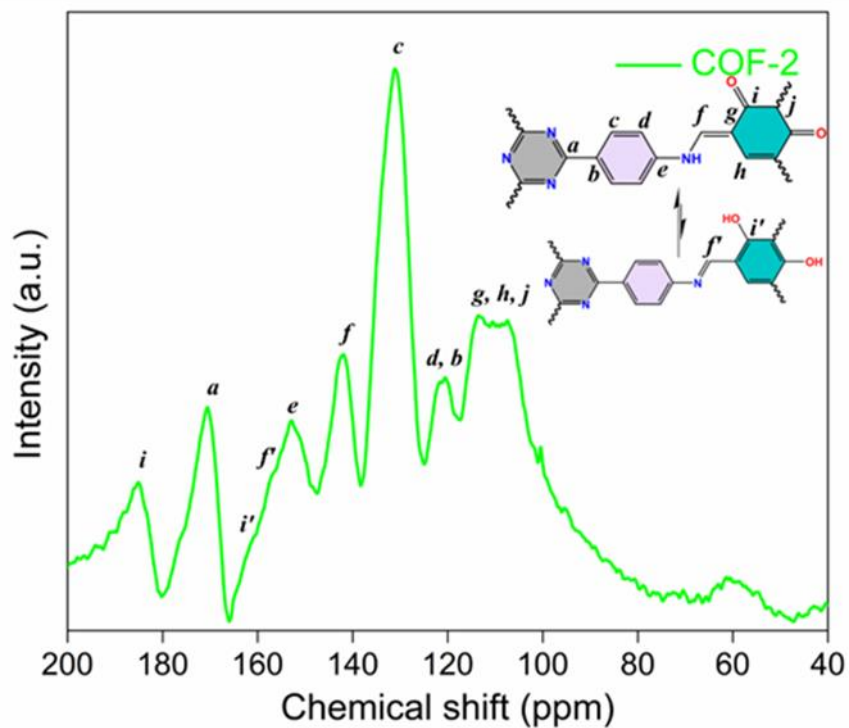
Figure S16: The solid-state ^{13}C CP-MAS NMR spectra of COF-2 exhibit sharp peaks at ~142 ppm, attributed to the enamine carbon (=C-NH-), and peaks ~184 ppm, which corresponds to carbonyl carbon (-C=O). Additionally, lower-intensity peaks corresponding to imine carbon (~156 ppm) and Csp^2-OH carbon (~169 ppm) are also observed. Also, peaks at ~170 ppm originate from the triazine core of the frameworks, while the absence of aldehyde (-CH=O) resonance peaks at ~190 ppm validate the formation of the COF.[1,3-5]
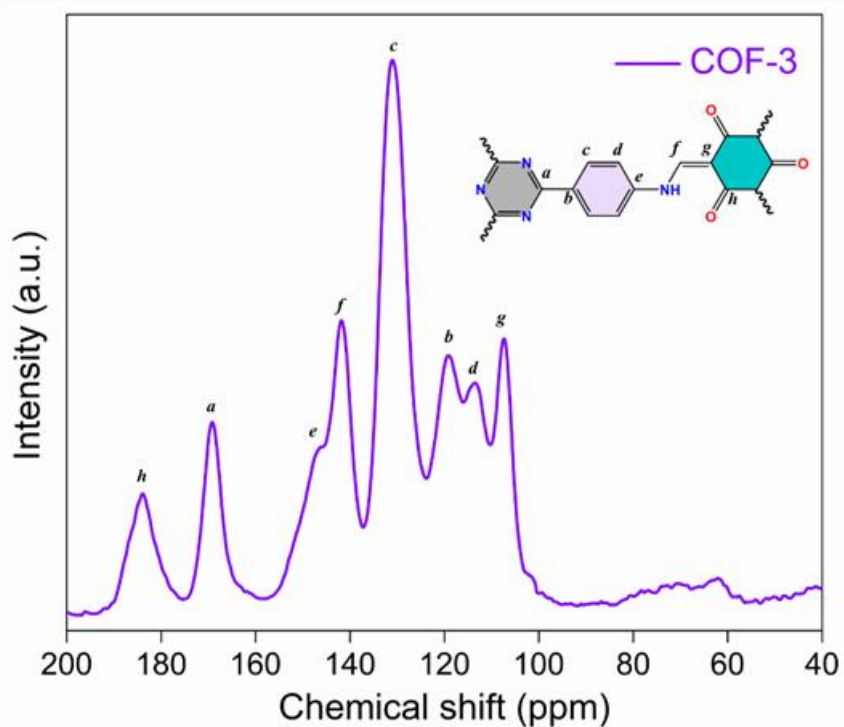
Figure S17: The solid-state ^{13}C CP-MAS NMR spectra of COF-3 confirm that it also predominantly exists in keto form, as evident by the presence of peaks corresponding to enamine carbon (=C-NH-) and carbonyl carbon (C=O) at ~142 and ~184 ppm, respectively. Furthermore, peaks at ~169 ppm originate from the triazine core of the frameworks, while the absence of aldehyde (-CH=O) resonance peaks at ~190 ppm validate the formation of the COF.[1-5]

Supporting note 3: The XPS study results provided information about the elemental constitution of these β-ketoenamine COFs, primarily indicating the existence of key elements (C, N, and O) (Figure S18-S20). The deconvoluted XPS spectra of N 1s and C 1s of the COFs indicated the formation of imine (-C=N-) bonded structures.[5] The XPS survey spectra displayed the characteristic peaks of different element present in the all the COFs, near about at ~285 eV, ~399 eV and ~532 eV corresponds to C 1s, N 1s and O 1s core energy levels, respectively. The high resolution deconvoluted C 1s XPS spectra exhibited the peak around ~284.2 eV, ~284.8 eV, ~286.2 eV and ~290.2 eV, corresponding to the aromatic -C=C bond, -C-C bond form the imine bond connected to the triazine moiety, -C-N bond from imine linkage (-C=N) or from enol bond (-C-O) and -C=O bond form the keto linkage, respectively in the structure of COF-1. Moreover, deconvoluted spectra of N 1s revealed the peak around ~398.3 eV and ~398.9 eV, corresponding to -C=N bond from triazine moiety and -C-NH bond from the iminol bond respectively. In case of COF-2, the deconvoluted C 1s XPS spectra exhibited the peaks at ~284.5 eV, ~285.1 eV, ~286.5eV and ~290.2 eV, corresponding to the aromatic -C=C bond, -C-C bond form the imine bond connected to the triazine moiety, -C-N bond from imine linkage (-C=N) or from enol bond (-C-O) and -C=O bond form the keto linkage, respectively. The high-resolution N 1s spectra showed peaks at ~398.6 eV and ~400.3 eV, corroborated to -C=N bond from triazine moiety and -C-NH bond from the iminol bond respectively. In case of COF-3, the deconvoluted C 1s spectra exhibited the peaks at ~284.1 eV, ~284.7 eV, ~286.1eV and ~290.2 eV, corresponding to the aromatic -C=C bond, -C-C bond form the imine bond connected to the triazine moiety, -C-N bond from imine linkage (-C=N) or from enol bond (-C-O) and -C=O bond form the keto linkage, respectively. Also, the high resolution N 1s spectra showed peaks at ~398.3 eV and ~399.7 eV, corroborated to -C=N bond from triazine moiety and -C-NH bond from the iminol bond respectively. The keto-enol tautomerism was clearly explained by the high-resolution O 1s spectra. C=O (keto form) and the -C-OH (enol form) are represented by deconvoluted O 1s spectra with peak at ~531.7 eV and ~532.8 eV for COF-1, at ~531.8 eV and ~533.5 eV for COF-2, and at ~530.9 eV and ~532.8 eV for COF-3, respectively. It is worth mentioning that the enol form is dominating form in the COF-1 when there is one -OH group present in the aldehyde and with increasing number of -OH group in the aldehyde the keto-enol tautomerism got irreversible with the keto as a stable form. A benzene ring with less –OH groups often exhibits a stronger aromatic dominance, which leads to a higher fraction of enol forms in the produced COFs. The ketoamine forms that are created when the enolimine form is converted start to exist in the backbone of COFs with the addition of the −OH group on the benzene ring. Furthermore, when the number of −OH groups is 3, the

predominant factor is the basicity of the imine nitrogen, resulting in the primary keto form being detected in their structures. The O 1s spectra of COF-1 and COF-2 show higher ratios of the enol-imine form to the ketoamine form than COF-3, indicating more reversible proton tautomerism.
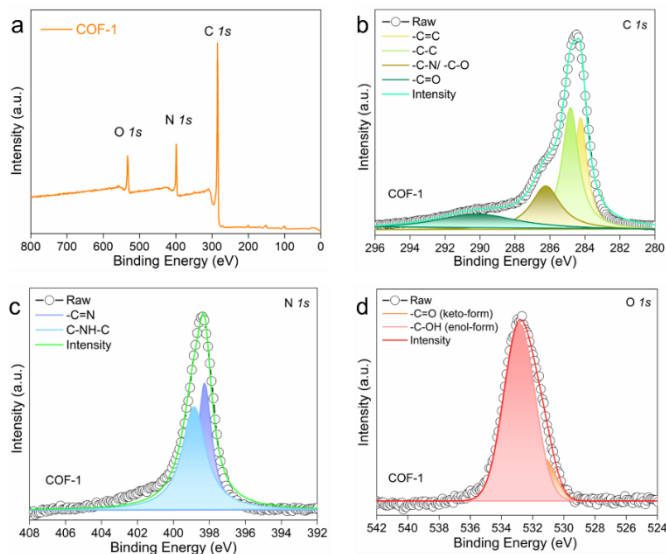
Figure S18: (a) XPS survey spectra, (b) C 1s XPS spectra, (c) N 1s XPS spectra, and (d) O 1s XPS spectra of COF-1.
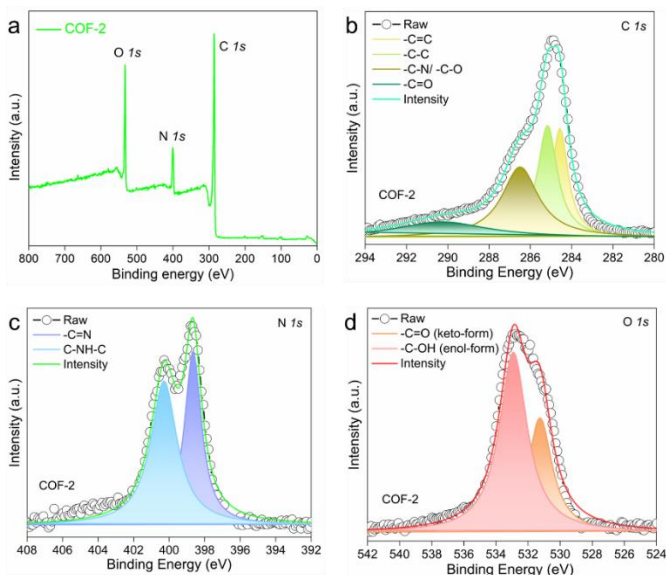
Figure S19: (a) XPS survey spectra, (b) C 1s XPS spectra, (c) N 1s XPS spectra, and (d) O 1s XPS spectra of COF-2.
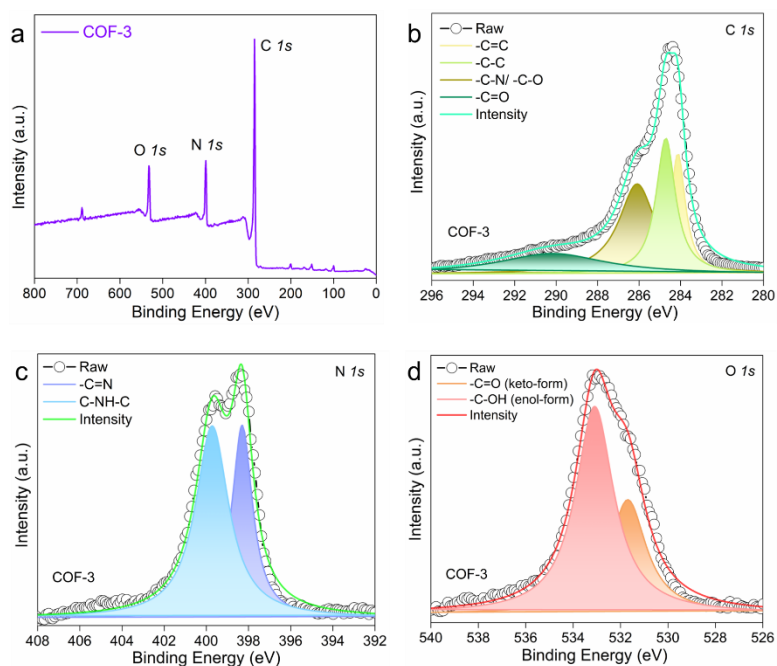
Figure S20: (a) XPS survey spectra, (b) C 1s XPS spectra, (c) N 1s XPS spectra, and (d) O 1s XPS spectra of COF-3.

Supporting note 4: Thermogravimetric analysis (TGA) was used to evaluate the thermal stability of these COFs, and the results confirmed that there was no discernible weight loss up to ~350 to ~550°C, further indicating high thermal stabilities (Figure S21).
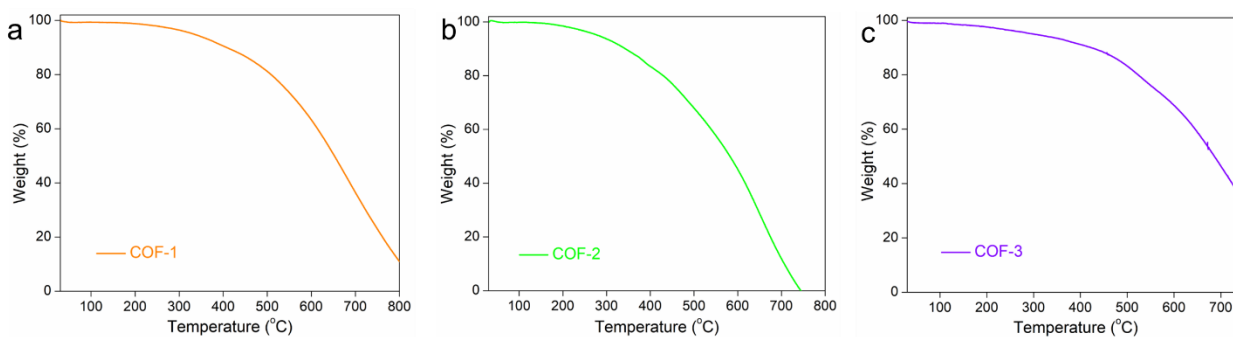
Figure S21: TGA profile of (a) COF-1, (b) COF-2 and (c) COF-3.

Supporting note 5: Afterward, using low-temperature (77 K) N_2 gas adsorption-desorption experiments, the permanent porosity, specific surface area, and pore size of these synthesized COFs were assessed. The N_2 sorption data of these COFs showed type-I adsorption isotherms, which are indicative of microporous structures (Figure S22). Nevertheless, it was discovered that the overall gas uptake was different, going in the following order: COF-2 > COF-1 > COF-3. Furthermore, for each of these COFs, the Brunauer–Emmett–Teller (BET) surface area was determined to be 1160 m^2 g^{-1}, 1331 m^2 g^{-1}, and 1017 m^2 g^{-1} for COF–1, COF–2, and COF–3, respectively. Additionally, nonlocal density functional theory (NLDFT) was used to determine the pore size distributions, revealing the distribution of micropores with an average pore width of ~1.61, 1.65 and ~1.58 nm for COF–1, COF–2, and COF–3, respectively, further indicating eclipsed AA stacking structure of these COFs (Figure S23).[4]
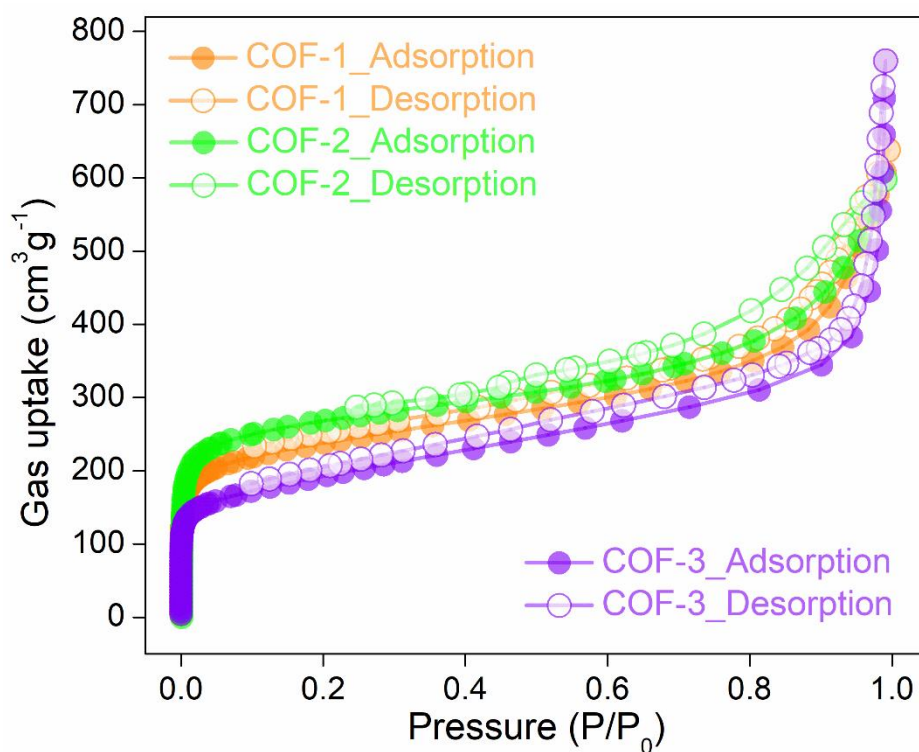
Figure S22: Nitrogen gas adsorption-desorption data of COF-1, COF-2 and COF-3 at 77K.
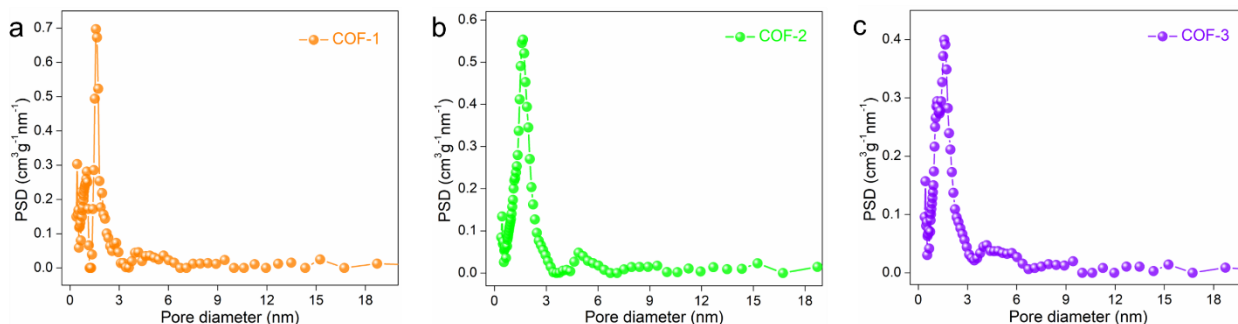
Figure S23: NLDFT pore size distribution of (a) COF-1, (b) COF-2 and (c) COF-3.

Supporting note 6: Following these structural characterizations, field emission scanning electron microscopy (FESEM) and transmission electron microscopy (TEM) were used to investigate the surface morphologies and microstructures of these COFs. A spherical aggregates surface morphology was observed for COF-1 in the FESEM images, whereas, COF-2 and COF-3 revealed nano-flakes-like and porcupine-like surface morphology, respectively (Figure S24).[3, 4] The TEM images of these COFs revealed a similar morphological finding (Figure S25). High resolution TEM (HR-TEM) images of the COFs reveal the long-range ordered stacking of the layers as well as arrangement of lattice fringes and pores in the crystalline microstructures (Figure S25).[4] The lattice fringes were measured to be ~1.49 and ~1.41 nm (corresponds to 100 diffractions) for COF-1 and COF-2, respectively. Moreover, elemental analysis, energy-dispersive X-ray spectroscopy (EDS), and the associated mapping from both FESEM and TEM experiments were used to identify the elemental compositions of the COFs. The existence and uniform distributions of the elements C, N, and O were seen in all of the COFs (Figure S26, S27). All these characterizations validated the detailed structures of the three COFs.
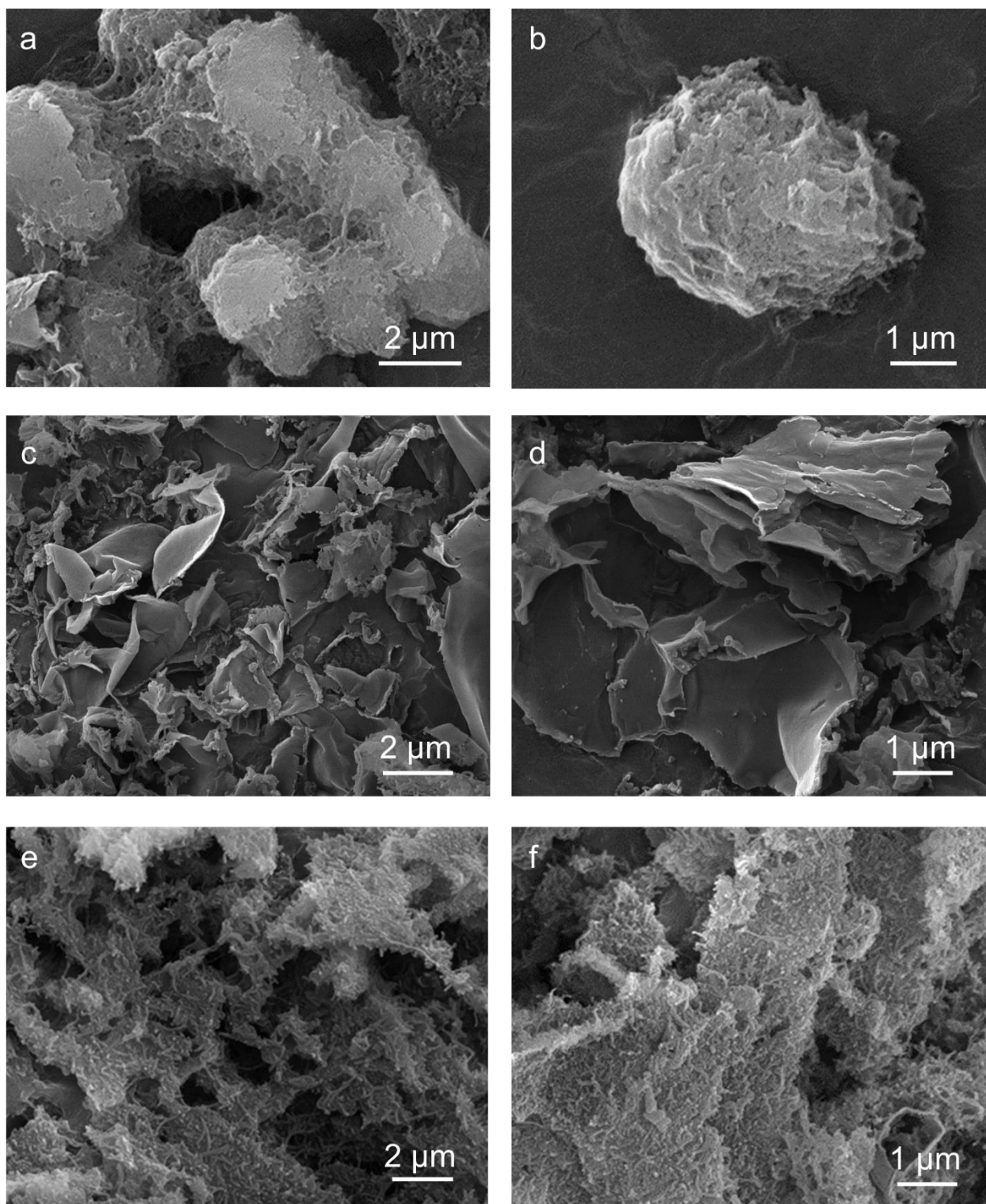
Figure S24: FESEM images of COF-1 (a, b), COF-2 (c, d), and COF-3 (e, f).
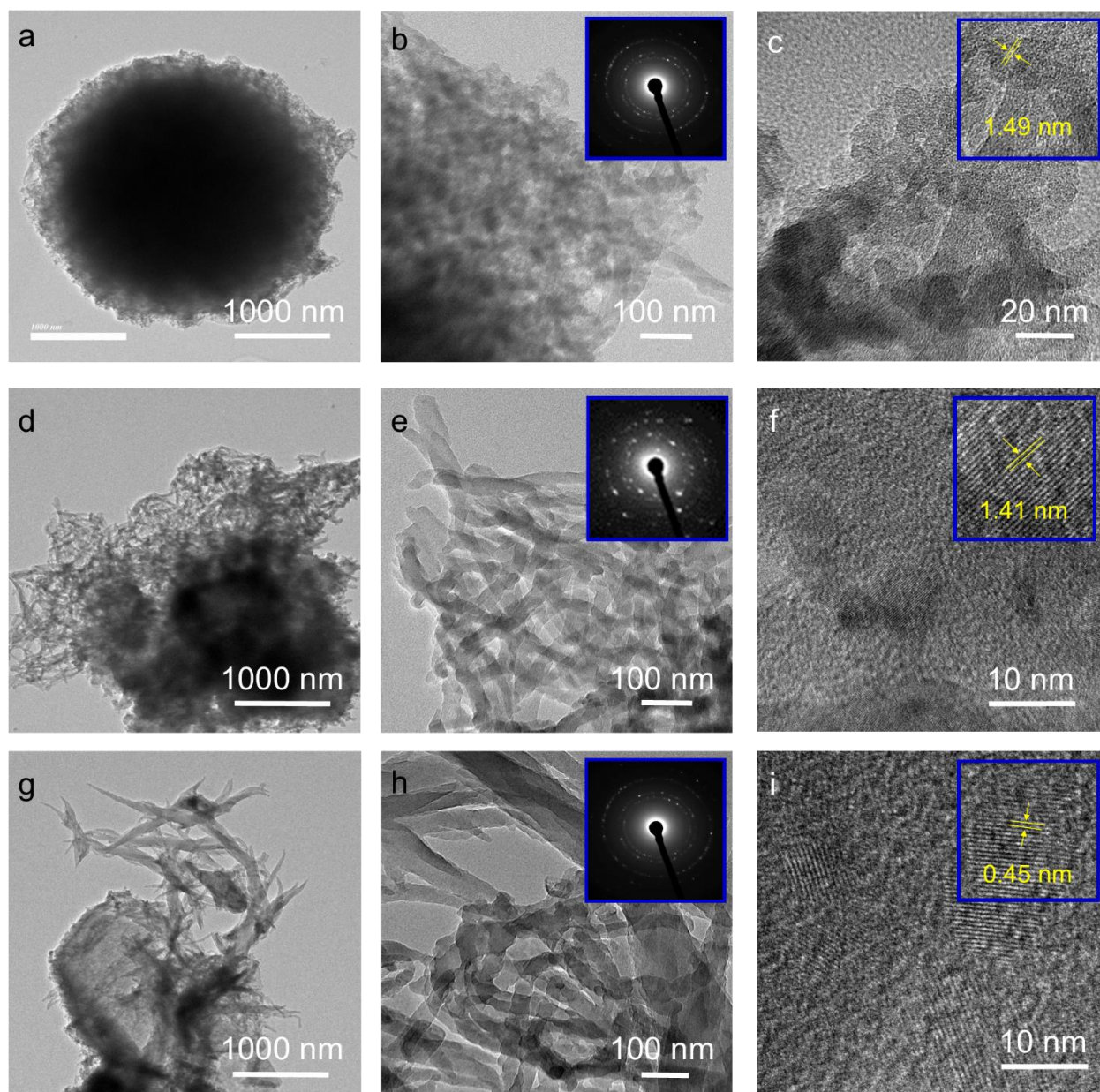
Figure S25: TEM & HRTEM images of COF-1 (a-c), COF-2 (d-f), and COF-3 (g-i).

Element	Weight%	Atomic%
C K	52.25	57.51
N K	25.75	24.31
O K	22.00	18.18
Totals	100.00	

Element	Weight%	Atomic%
C K	49.49	54.97
N K	24.59	23.42
O K	25.92	21.61
Totals	100.00	

Element	Weight%	Atomic%
C K	55.67	60.84
N K	23.93	22.43
O K	20.39	16.73
Totals	100.00	
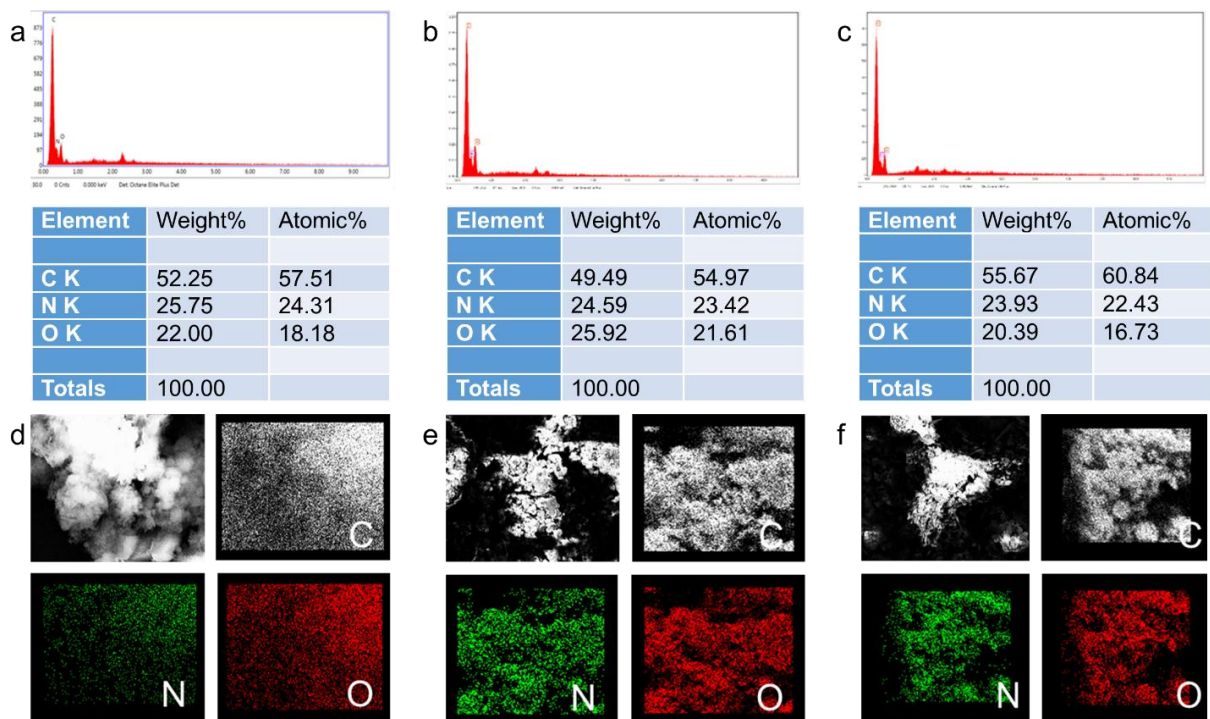
Figure S26: EDX data (a, b, c) and corresponding elemental mapping images (d, e, f) of COF-1 (a, d), COF-2 (b, e), and COF-3 (c, f) from FESEM experiment.
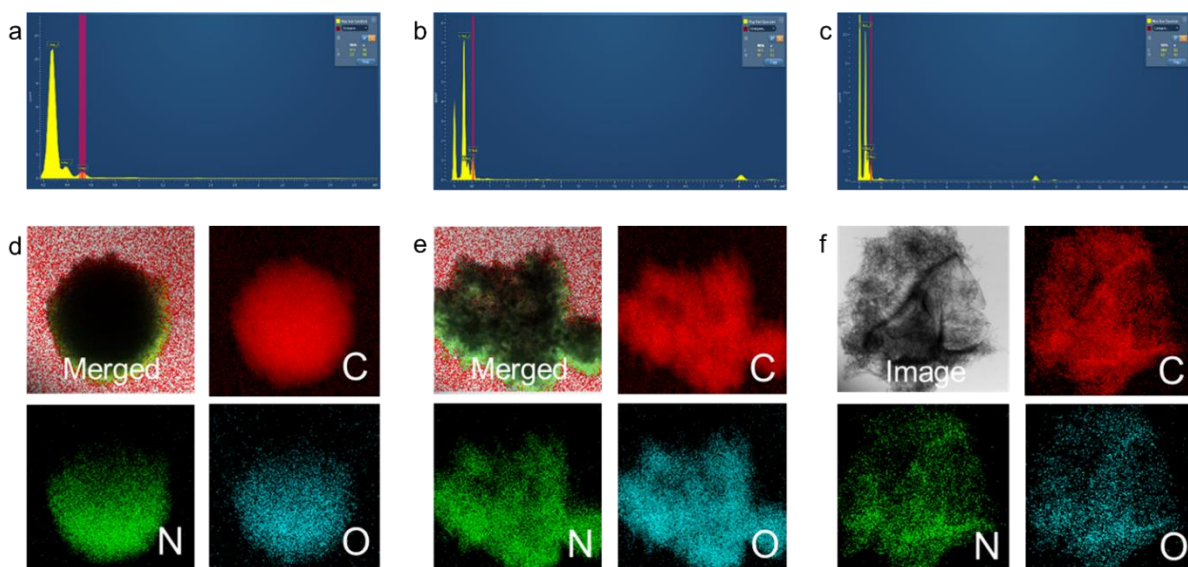
Figure S27: EDX profile (a, b, c) and corresponding elemental mapping images (d, e, f) of COF-1 (a, d), COF-2 (b, e), and COF-3 (c, f) from TEM experiment.

Supporting note 7: In addition, these COFs were found to demonstrate high chemical stability in both acidic and basic conditions. To perform the chemical stability test of these COFs under acidic and basic condition, we exposed certain amount of each COFs to pH =1 (aqueous HCl solution) and pH = 14 (aqueous NaOH solution), individually for 24 h. After one day, the pH solution treated COF samples were separated, washed and dried under vacuum. These dried samples were then characterized with PXRD analysis (Figure S28-S30).
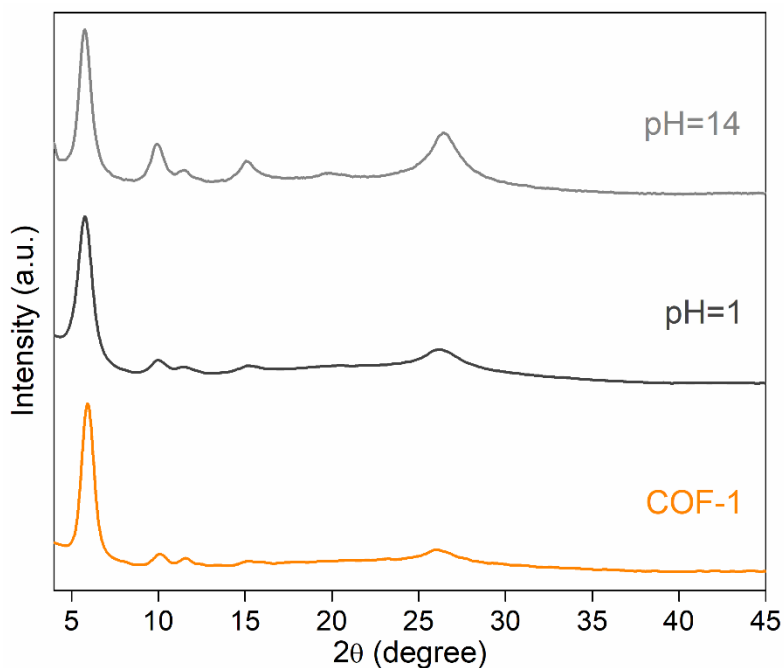
Figure S28: PXRD profile of COF-1 after treatment with various chemical conditions.
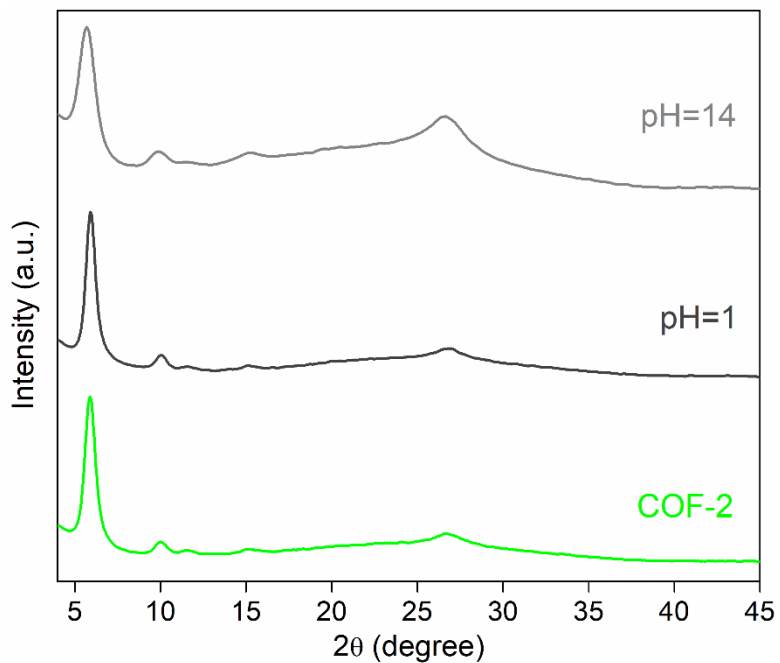
Figure S29: PXRD profile of COF-2 after treatment with various chemical conditions.
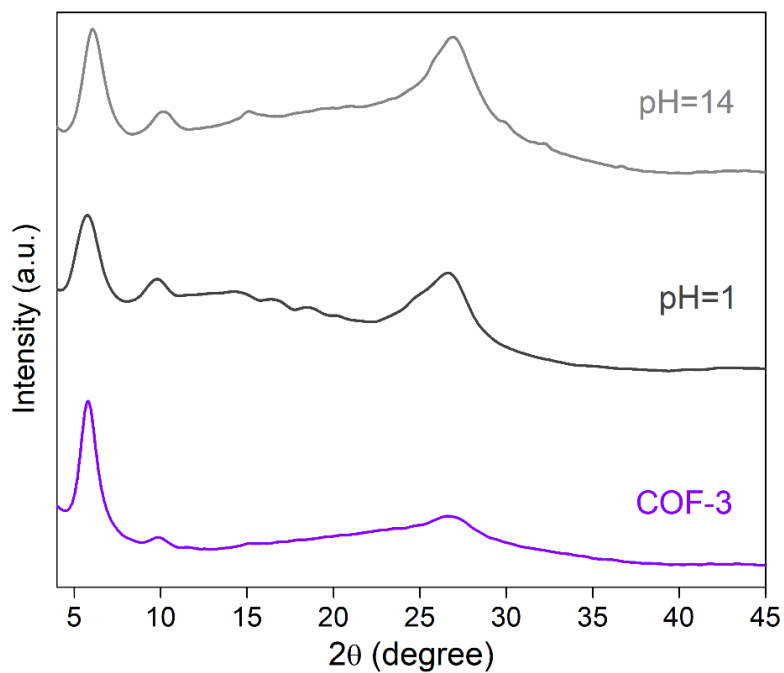
Figure S30: PXRD profile of COF-3 after treatment with various chemical conditions.

Section S4: Bromine sequestration studies

S4.1 General Consideration: The aqueous or organic solution of bromine (Br_2) was prepared by dissolving a certain amount of liquid bromine into deionized water (10 mmol for kinetics and 30 mmol for capacity) or cyclohexane (4 mmol for kinetics and 10 mmol for capacity) solution and the different concentrations were obtained by diluting the stock solution with the proper amount of distilled water/cyclohexane unless otherwise indicated. The concentrations of Br_2 during all the experiments were detected by UV-vis spectroscopic analysis. All the adsorption experiments were performed at ambient conditions. All the data has been collected three times through UV-vis analysis to plot the final adsorption results. All the solution phase Br_2 capture tests were performed under dark condition in order to avoid the degradation of bromine molecules in the presence of light (Figure S30).
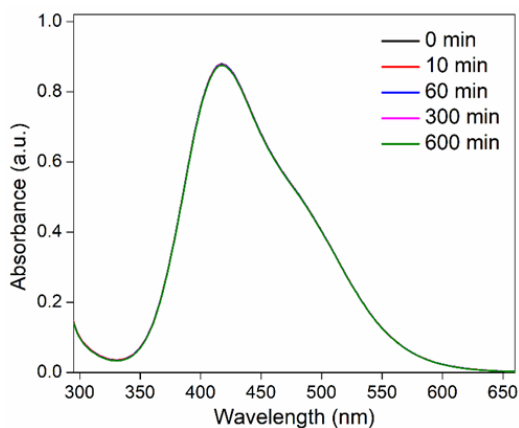
Figure S31: UV-vis profile of bromine in water under dark condition with incremental time.

S4.2 Vapor phase static bromine uptake studies: COF-1-3 (~15 mg) was weighted in a glass vial, and this vial was exposed to molecular bromine for variable time at 25 °C under dry condition in a closed system. After the corresponding adsorption time, the glass vial was taken out, exposed to air for some time and weighed. Bromine uptake capacity of the compound was calculated by the weight difference of glass vials before and after adsorption, using the formula:

$$w = \frac{(m_2 - m_1)}{m_1} x100\%$$
............(1)

Where, w (g.g^{-1}) is the adsorption capacity of iodine uptake, m_1 (g) and m_2 (g) are the mass of compounds with the glass vial before and after being exposed to bromine vapor. The static adsorption of bromine

under humid condition was performed applied the same procedure as for dry condition, except that a glass vial containing excess water was introduce separately into an another chamber connected with the sample container. The values of uptake capacity are the average values of at least three experiments.

S4.3 Retention ability test: To study the adsorption stability for bromine-loaded material in static system, a certain amount of bromine-loaded material (Br_2@COF-1-3) was taken in an open glass vial, and the vial was placed in an empty large bottle, which was placed at room temperature and ambient pressure. After one day, the weight of the vial containing bromine-adsorbed material was recorded and the vial was placed back into the empty large bottle. The large bottle was opened to further continue the experiment for next 7 days.

S4.4 Bromine (Br_2) release studies in dimethyl sulfoxide: Time-dependent UV-Vis measurements were carried out in dimethyl-sulfoxide to record the Br_2 releasing efficiency from the Br_2@COF. In a typical experiment, 2 mg of Br_2@COF was immersed in ~4 mL of dimethyl-sulfoxide in a reaction vial with mild shaking. The UV-Vis adsorptions were recorded periodically removing a 2 mL of dimethyl-sulfoxide solution from the mother solution and then transferred back.

S4.5 Vapor phase dynamic bromine uptake studies: The gaseous bromine adsorption in dynamic system was performed in a home-built setup (Figure S37). 20 mg COF-1-3 was packed into a glass tube with glass wool filling the void space of both ends, which served as the adsorption cell and valve 1 and valve 2 were opened and valve 3 was closed. A nitrogen flow (10 ± 3 cm^3/min) passed through the generator to blow the bromine vapor into the COFs in the adsorption cell. In addition, the flow rate of Br_2 gas was measure as 16 ± 4 mg/h, which was determined through trial and error of repeating measurement. The effluent from the adsorption cell was treated with 0.1 M KOH solution in outlet. After 12 h, the adsorption capacity for bromine was calculated from the weight difference of compound containing glass tubes before and after adsorption.

S4.6 Aqueous phase static molecular bromine (Br_2) capture studies: To study the bromine adsorption performance in aqueous solution system, we first prepared 30 mmol of the molecular bromine (Br_2) solutions in water. To prepare the saturated bromine aqueous solution, an excess of bromine was added into 1 L deionized water, and after stirred for ~6 h.

S4.7 Static bromine (Br₂) capture studies in cyclohexane: To study the bromine adsorption performance in cyclohexane solution system, we first prepared 10 mmol of the molecular bromine (Br₂) solutions in cyclohexane.

S4.8 Solution phase adsorption kinetic studies: For the time-dependent study for Br₂ removal, we took 2 mL of 10 mmol stock aqueous Br₂ solution in a cuvette. We recorded the initial absorbance value with the help of UV−visible (UV−vis) spectroscopy. Then, 2 mg of COF was added to the cuvette. After treating the compound, we recorded the absorbance spectra of the supernatant solution at regular time intervals. We calculated the % removal data of Br₂, decrease in the concentration of the Br₂ vs time, and uptake of Br₂ from this study using the following equations:

$$\mathbf{Dt = \frac{(C_0 - C_{-L})}{C_0} x100\% = \frac{(A_0 - A_t)}{A_0} x\ 100\%} \qquad \text{………(2)}$$

$$\mathbf{\frac{C_0 - C_t}{C_0} = \frac{A_0 - A_t}{Ao}} \qquad \text{…………………………(3)}$$

$$\mathbf{C_t = C_0\ x\ [1 - (A_0 - A_t/A_0)]} \qquad \text{………………………….(4)}$$

$$\mathbf{Q_t = (C_t - C_0)x\frac{v}{m}} \qquad \text{……………………………..(5)}$$

D_t is the exchange capacity, C_0 and A_0 are the initial concentration and absorbance of the Br₂ solution, respectively, and C_t and A_t are the concentration and absorbance of the Br₂ solution at specific times, respectively. Q_t is the uptake amount in time t in mg g^{-1}, V is the volume of the solution in mL, and m is the mass of the compound in g. The kinetics data were fitted to a pseudo-second-order kinetic model using the following equation.

S4.9 Pseudo-second-order model fitting: To investigate the kinetic adsorption behavior towards iodine, pseudo-second-order kinetic model was used to evaluate the adsorption data, and its linear form can be expressed as follow:

$$\mathbf{\frac{t}{Qt} = \frac{1}{k_2 Q_e^2} + \frac{t}{Q_e}} \qquad \text{…………………………...(6)}$$

Where, Q_t and Q_e represent the adsorbed amount (mg.g^{-1}) at time and at equilibrium t (min), respectively, k_2 represent the Pseudo-second-order rate constant of adsorption (g mg^{-1} min^{-1}). The experimental data

was fitted using Pseudo-second-order kinetic model, and R^2 is the correlation coefficient of the fitting curve.

S4.10 Bromine uptake capacity studies: 2.5 mg of COF was kept in contact with 5 mL of Br_2 solutions with concentrations 30 mmol for 24 h under stirring conditions. After 24 h, compounds were filtered out, and the filtrate was analyzed by UV−vis studies. The absorbance was recorded by diluting the solution, and the uptake amount was calculated from the initial and final absorbance value of the filtrate using equations (2−5).

Langmuir model, $Q_e = Q_m.C_e/(K_d+C_e)$; Where, C_e(ppm) and Q_e(mg g^{-1}) are the Br_2 concentration at equilibrium and amount of Br_2 adsorbed at equilibrium respectively. Q_m (mg g^{-1}) is the maximum amount of Br_2 per mass of adsorbent to form a complete monolayer. K_d (mg L^{-1}) is a constant to the affinity of the binding sites.

S4.11 Distribution coefficient (K_d) value calculation: The distribution coefficient (K_d) value as used for the determination of the affinity and selectivity of sorbents for Br_2, is given by the equation:

$$k_d = \left(\frac{C_0 - C_e}{C_e}\right) x \frac{v}{m}$$

.........................(7)

Where, v is the volume of the testing solution (mL), m is the amount of solid adsorbent (g), C_o is the initial concentration of Br_2, and C_e is the equilibrium concentration of Br_2.

S4.12 Selectivity test in presence of other competing ions: For testing the influence of competing ions, in this study, 2 mg each of COF-2 was kept in contact separately with a binary solution containing 1 mL of Br_2 solution and 1 mL each of various competing anions solution (NO_3^-, Cl^-, Br^-, ClO_4^-, SO_4^{2-}) with equal concentration for 24 h under stirring conditions. Then, after 24 h, the compounds were filtered, and the filtrate was analyzed by UV−vis studies using the protocol discussed above. The efficiency of the capture process in the presence of competing anions was measured with respect to a blank where 1 mL of water is used instead of the competing anion solution. The absorbance was recorded by diluting the solution, and the uptake amount was calculated from the initial and final absorbance value of the filtrate using equations 2−5.

S4.13 Dynamic column-based flow-through Br_2 capture study: We conducted a dynamic column-based flow-through Br_2 capture experiment with the flow of bromine aqueous and cyclohexane solution.

The membrane of COF-2 was installed in to a separation chamber (Figure S80), and a certain concentration of Br_2 aqueous or cyclohexane solution was passed through the cell. The bromine concentrations of filtrate and the original solution were detected by UV-Vis spectrophotometer.

Section S5: Vapor phase bromine capture studies
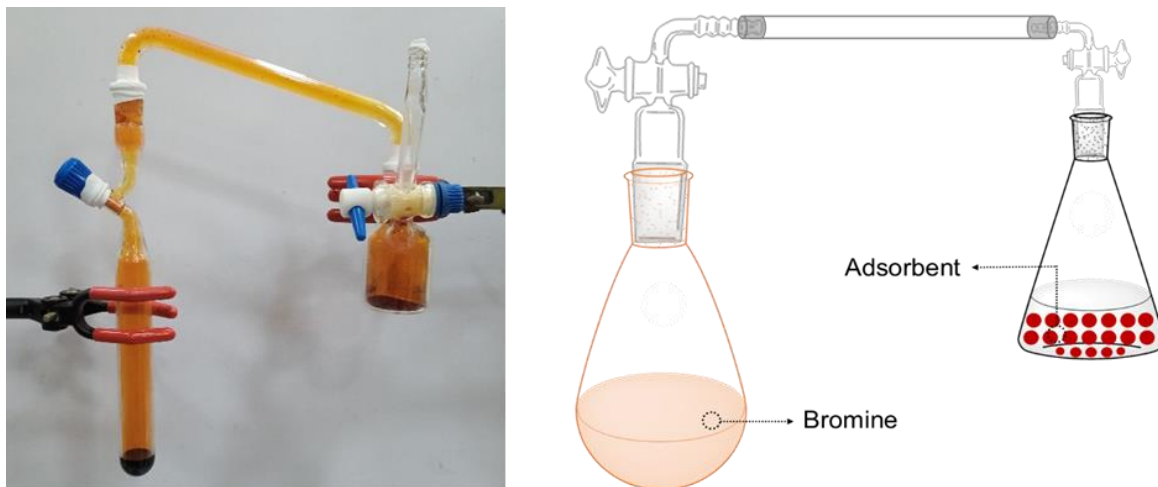
Figure S32: Digital image and schematic diagram of the experimental setup for performing the vapor phase Br_2 capture test under static condition.

Table S1: Comparison table of vapor and solution phase bromine adsorption capacities of various adsorbents in static condition.

Adsorbents	Type of material	Capacity $(g.g^{-1})$	Reference
COF-1	**COF**	**4.7**	**This work**
COF-2	**COF**	**5.1**	**This work**
COF-3	**COF**	**4.1**	**This work**
TAEDP-TA-OMe	COF	4.6	*Angew. Chem. Int. Ed.* 2024, **63**, e202403658.
TAP-TA-OMe	COF	3.4	*Angew. Chem. Int. Ed.* 2024, **63**, e202403658.
COF-2H1	COF	3.79	*ACS Appl. Nano Mater.* 2024, **7**, **14**, 16413–16421.
C4P-POP	POP	3.6	*J. Am. Chem. Soc.* 2022, **144**, 16755-16760.

UiO-67	MOF	1.9	*Angew. Chem. Int. Ed.* 2017, **56**, 14622-14626.
PCN-700	MOF	2.6	*Angew. Chem. Int. Ed.* 2017, **56**, 14622-14626.
PCN-605-H	MOF	4.2	*Angew. Chem. Int. Ed.* 2017, **56**, 14622-14626.
PCN-606-OME	MOF	3.7	*Angew. Chem. Int. Ed.* 2017, **56**, 14622-14626.
TCuCN	MOF	0.16	*J. Solid State Chem.* 2021, **302**, 122458.
Co_2Cl_2BTDD	MOF	0.25	*J. Am. Chem. Soc.* 2017, **139**, 5992-5997.
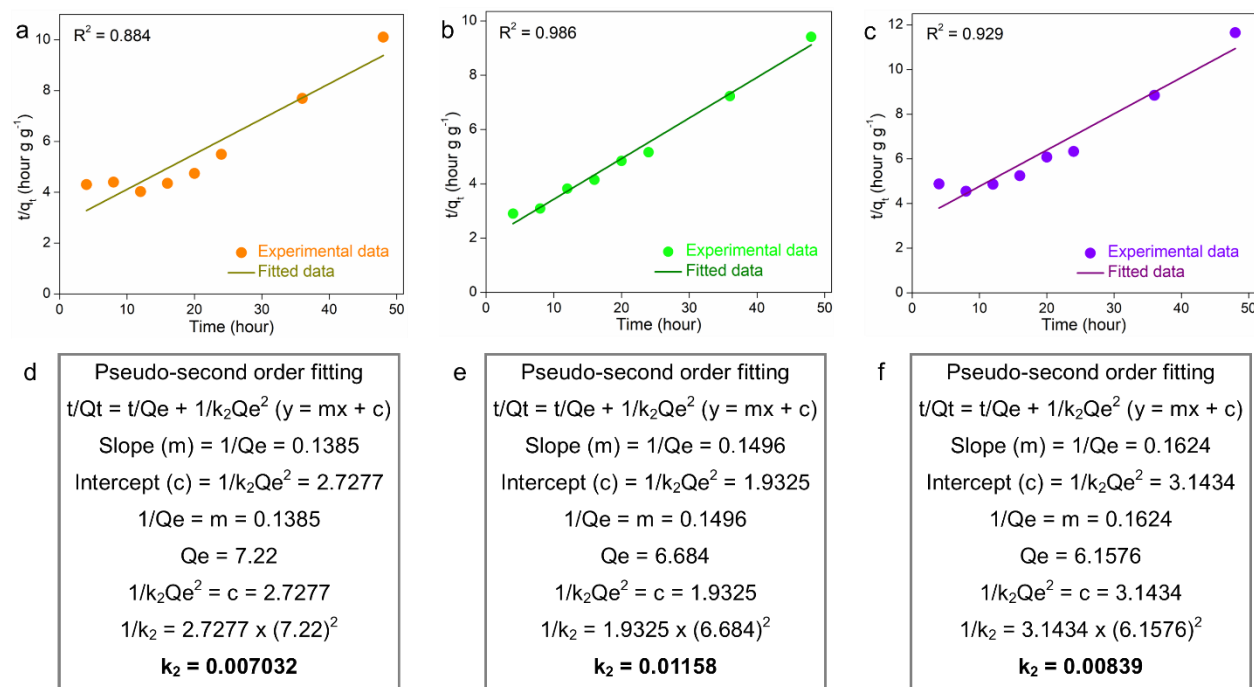
Figure S33: Pseudo-second-order model fitting and their corresponding rate constant values for vapor phase bromine capture tests under static condition by (a, d) COF-1, (b, e) COF-2 and (c, f) COF-3, respectively, at room temperature.
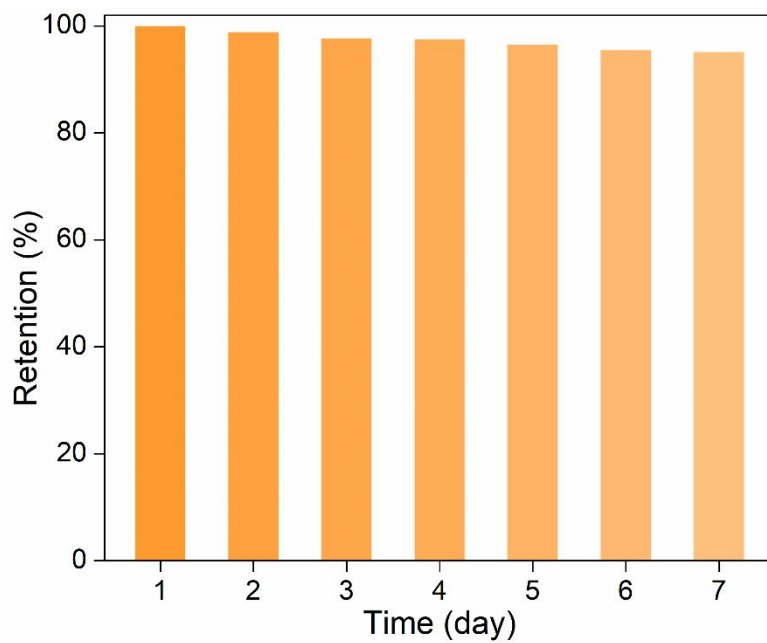
Figure S34: Bromine retention efficiency result of COF-1.
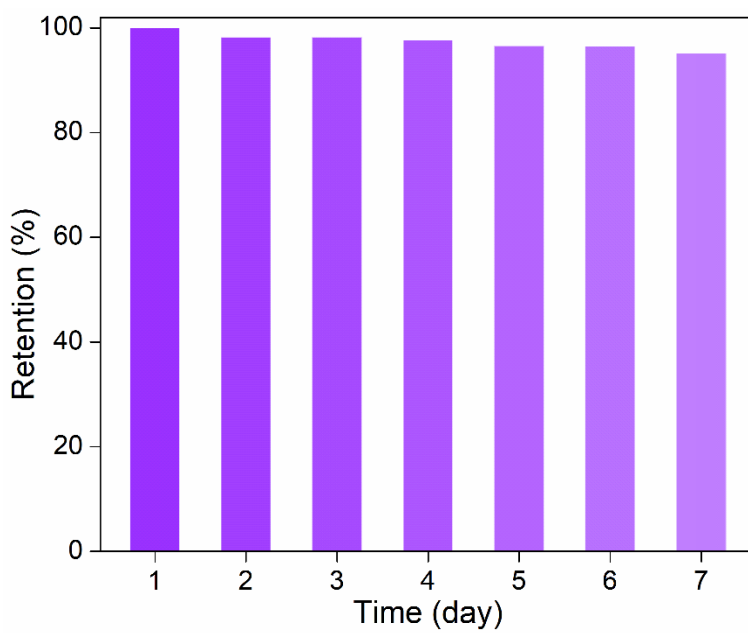
Figure S35: Bromine retention efficiency result of COF-3.
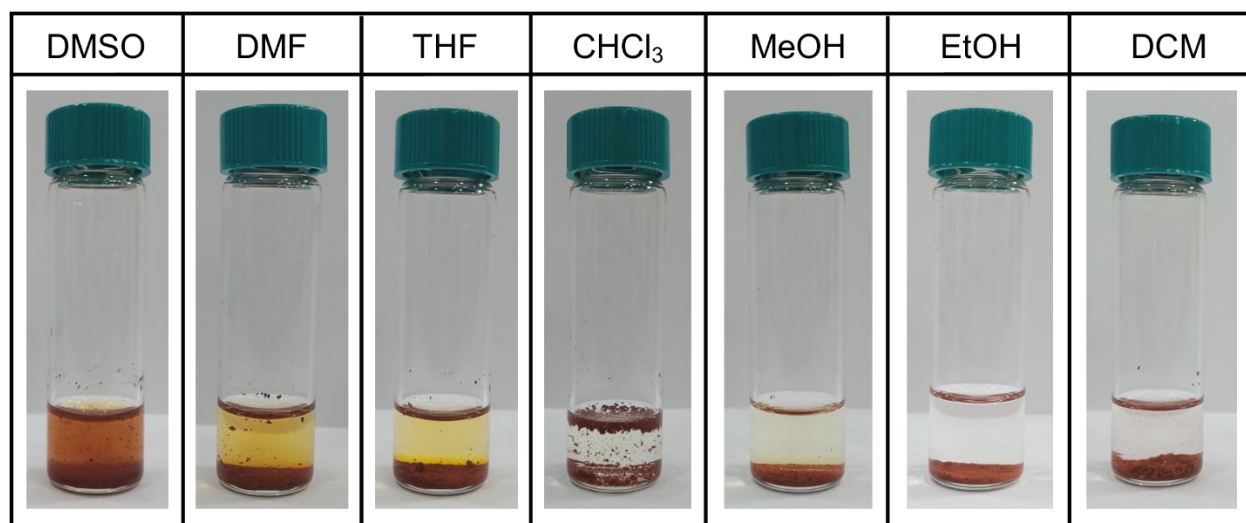
Figure S36: Digital images of release of bromine from Br$_2$@COF-2 in different solvents.
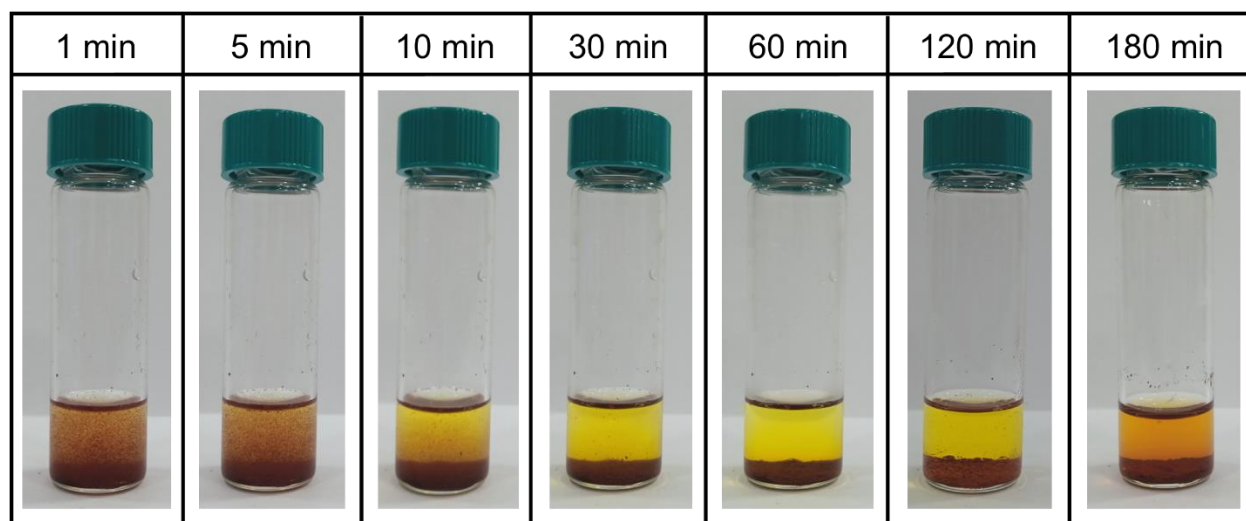
Figure S37: Digital images of release of bromine from Br$_2$@COF-2 in DMSO with incremental time.
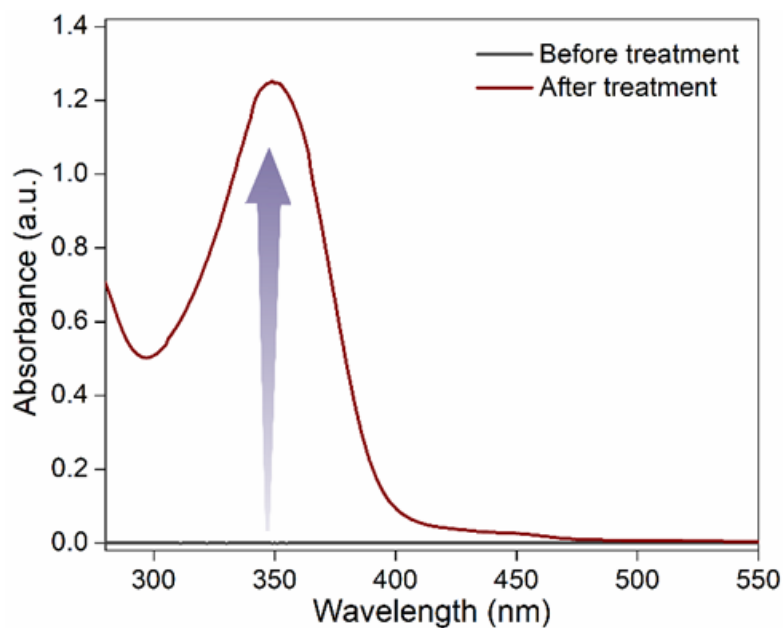
Figure S38: UV-vis spectra of bromine release from Br$_2$@COF-2 in DMSO.
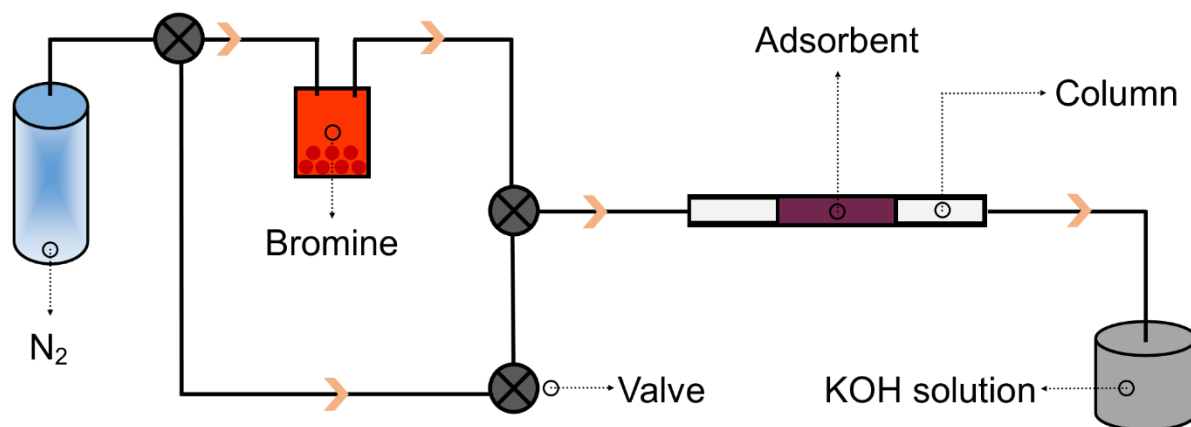
Figure S39: Schematic representation of the instrument setup for dynamic gaseous bromine adsorption experiment.

Section S6: Bromine adsorption mechanism

Element	Weight %	Atomic %	Error %
C K	41.81	64.92	9.76
N K	12.05	16.04	11.65
O K	8.87	10.34	10.76
Br L	37.27	8.70	1.47

Element	Weight %	Atomic %	Error %
C K	39.17	63.20	9.95
N K	12.08	16.71	11.71
O K	8.54	10.34	10.84
Br L	40.21	9.75	1.45

Element	Weight %	Atomic %	Error %
C K	49.32	69.74	10.16
N K	10.96	13.30	16.17
O K	10.04	10.65	13.17
Br L	29.68	6.31	1.95
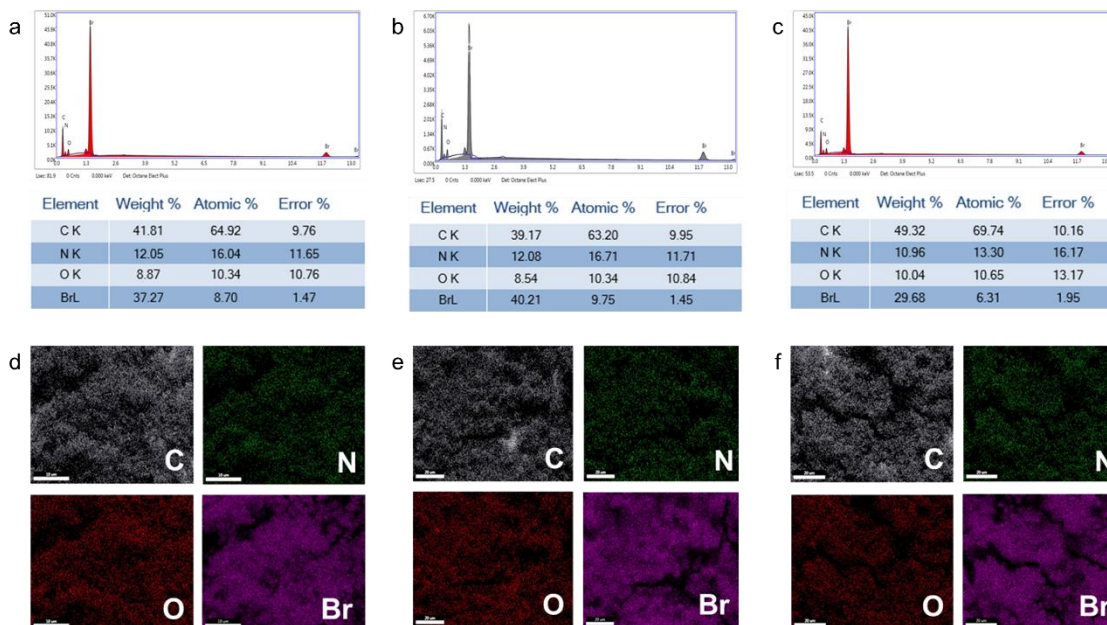
Figure S40: EDX data (a, b, c) and corresponding elemental mapping images (d, e, f) of Br$_2$@COF-1 (a, d), Br$_2$@COF-2 (b, e), and Br$_2$@COF-3 (c, f) from FESEM experiment.
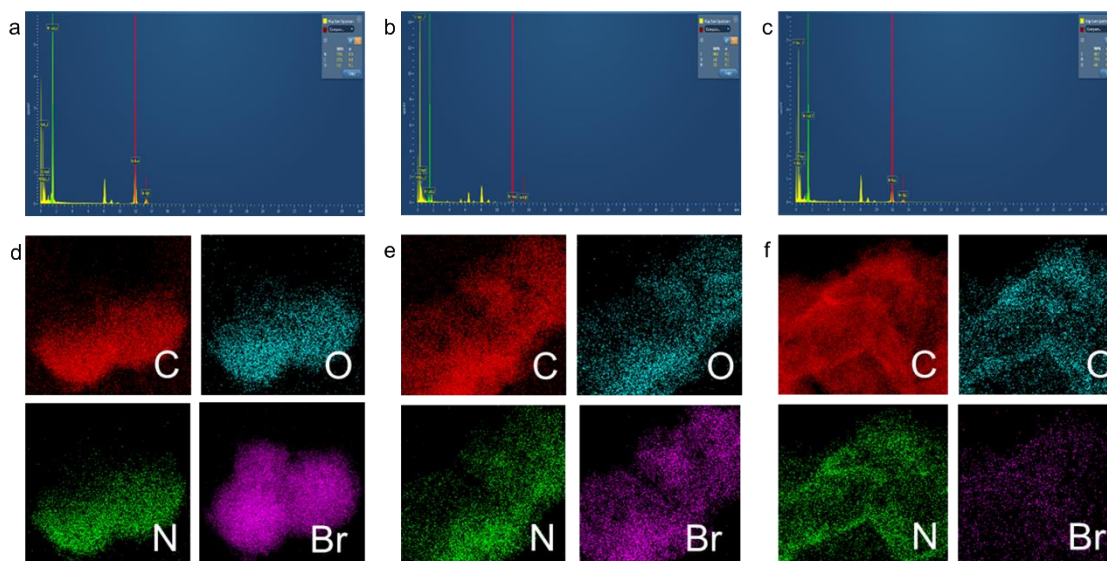
Figure S41: EDX data (a, b, c) and corresponding elemental mapping images (d, e, f) of Br$_2$@COF-1 (a, d), Br$_2$@COF-2 (b, e), and Br$_2$@COF-3 (c, f) from TEM experiment.
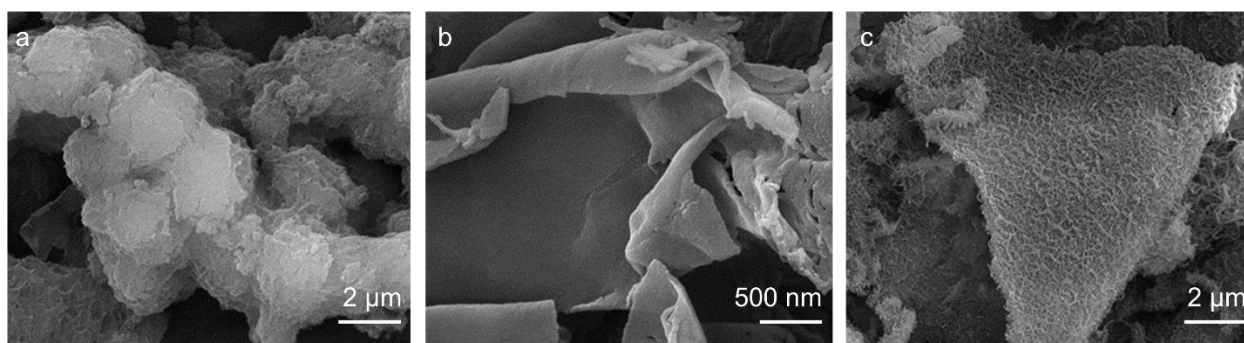
Figure S42: FESEM images of (a) Br$_2$@COF-1, (b) Br$_2$@COF-2, and (c) Br$_2$@COF-3.
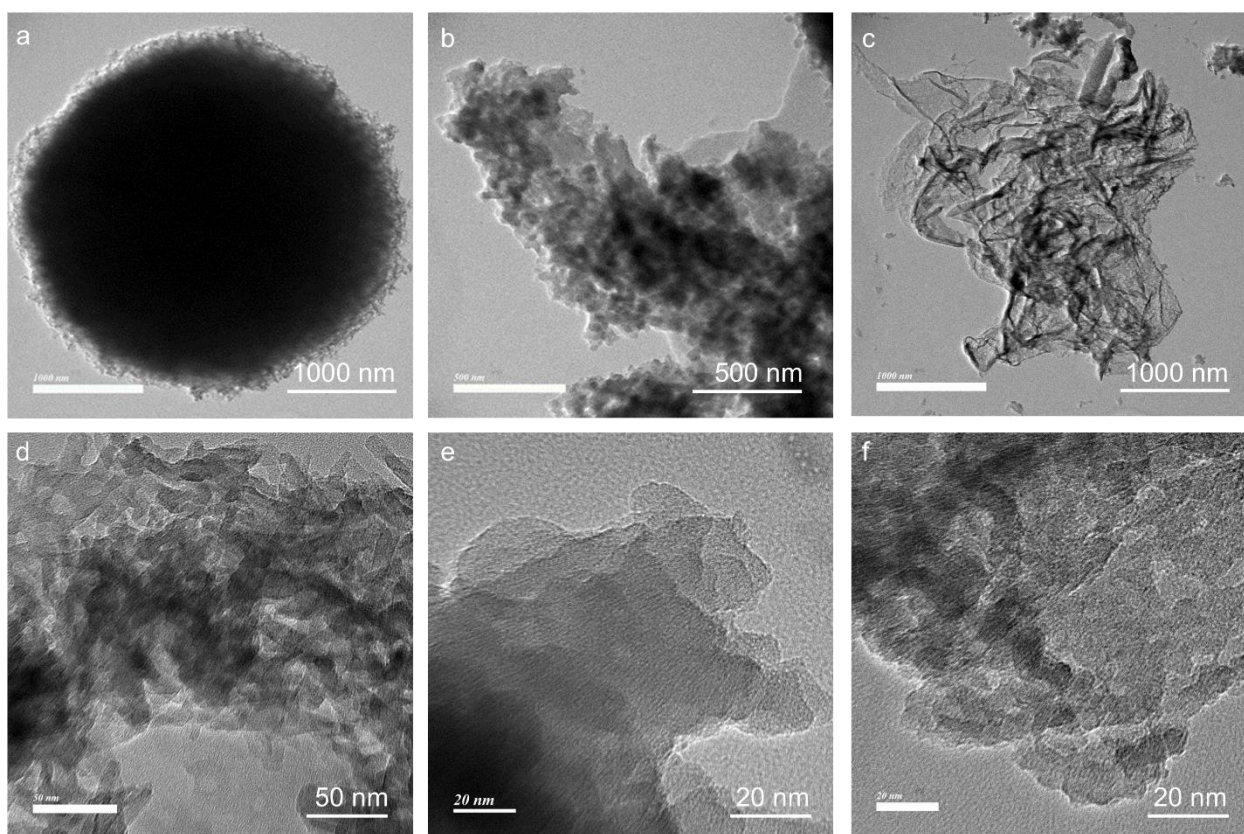
Figure S43: TEM and HRTEM images of (a, d) Br$_2$@COF-1, (b, e) Br$_2$@COF-2, and (c, f) Br$_2$@COF-3.
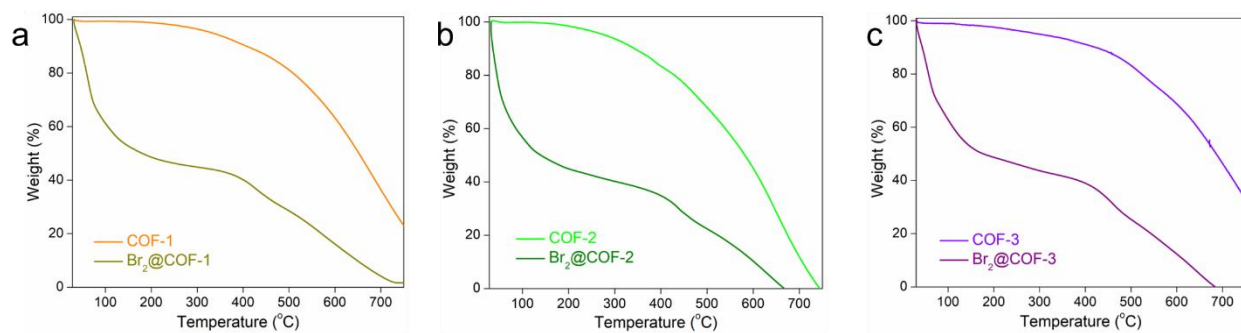
Figure S44: TGA profiles of (a) Br$_2$@COF-1, (b) Br$_2$@COF-2, and (c) Br$_2$@COF-3.
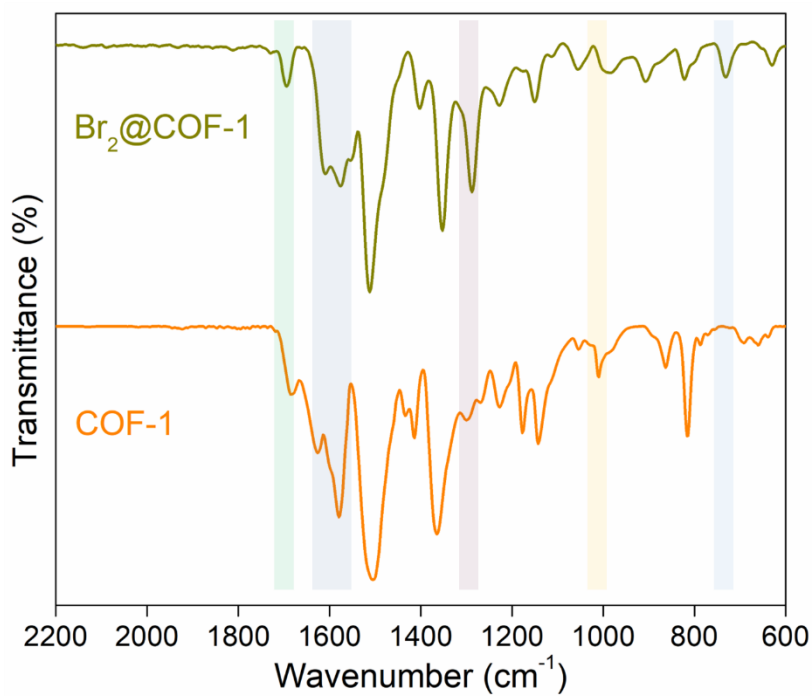
Figure S45: FT-IR spectra of COF-1 before and after Br$_2$ absorption test.
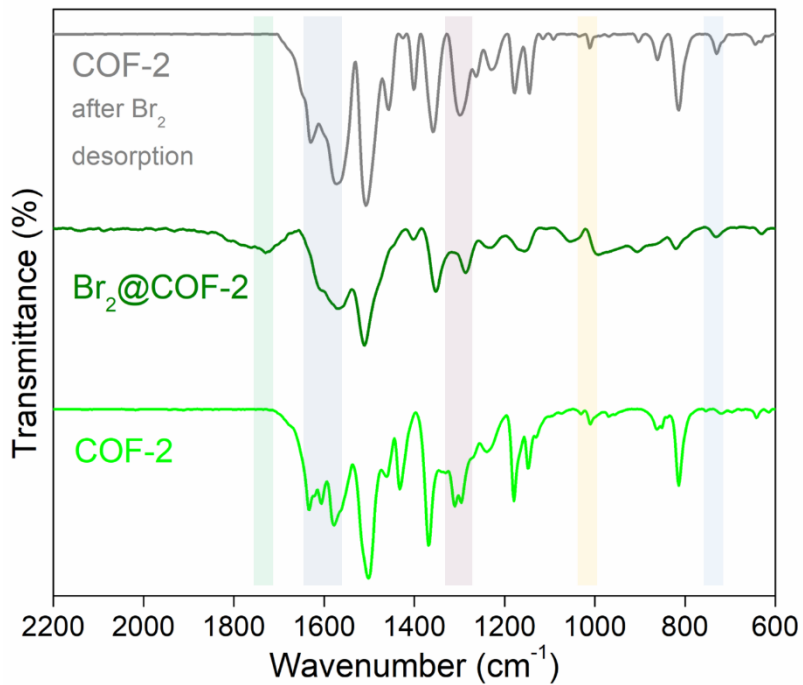
Figure S46: FT-IR spectra of COF-2, Br_2@COF-2 and COF-2 after Br_2 desorption test.
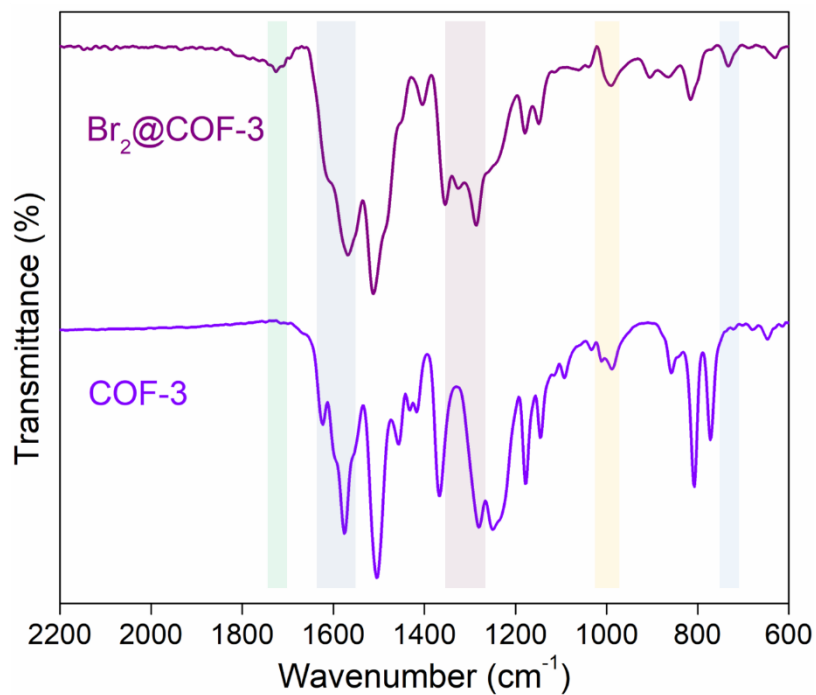
Figure S47: FT-IR spectra of COF-3 before and after Br_2 absorption test.

Supporting note 8: We have recorded the FT-IR spectra of the COFs before and after bromine adsorption, and further compare with each other. In general, the FT-IR signals of the bromine loaded COFs were found to shift as well as found to appear a few of new peaks with compare to the pristine COFs. For example, in case of COF-2 and Br_2@COF-2, the intensities of FT-IR signals at ~1435 and 997 cm^{-1}, associated with C-H bond, ~1178 cm^{-1} associated with C-N bond, and ~1634 cm^{-1} associated with –C=N bond were found to reduce. Furthermore, there was a progressive redshift of the peak at 1605 cm^{-1} corresponding to the C=C bond. A few new vibration bands corresponding to C–Br and N–Br interactions have been observed in the range of 627 to 732 cm^{-1} and in 1607–1643 cm^{-1} range, respectively. Gradual peak broadening in the wavenumber range of 2300–3200 cm^{-1} was noted. This suggests that the benzene and triazine rings on the COF structures and adsorbate molecules interact with one another intermolecularly. These spectrum shifts show that the triazine, imine, and phenyl rings functional groups of the COFs all had a role in the creation of charge-transfer complexes with bromine molecules.[8-12]
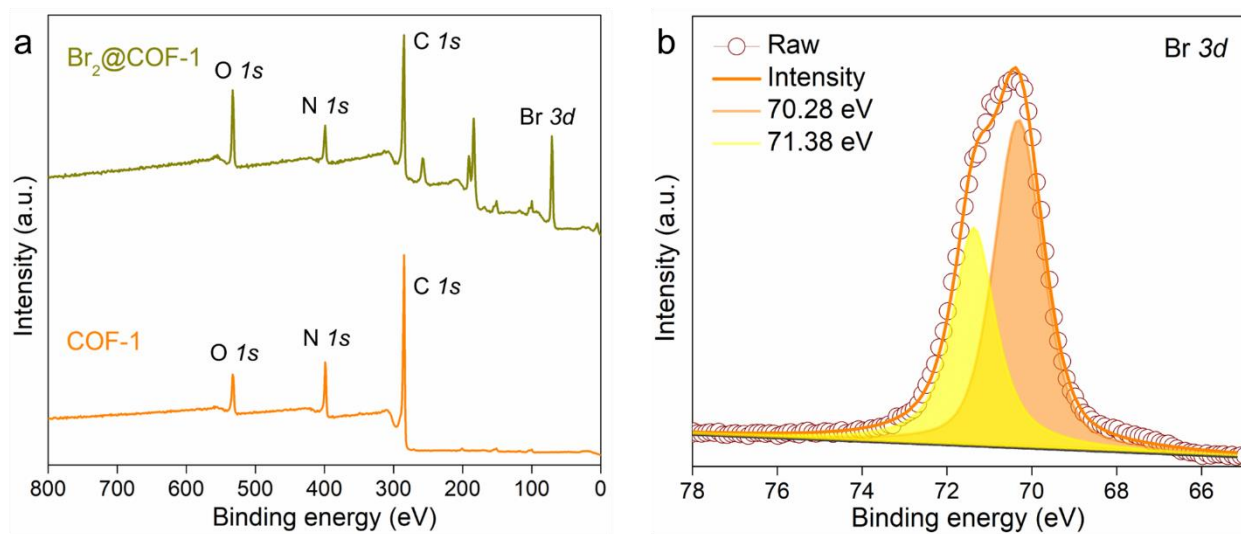
Figure S48: (a) XPS survey spectra of COF-1 and Br_2@COF-1, (b) Br 3d XPS spectra of COF-1 after Br_2 absorption test.
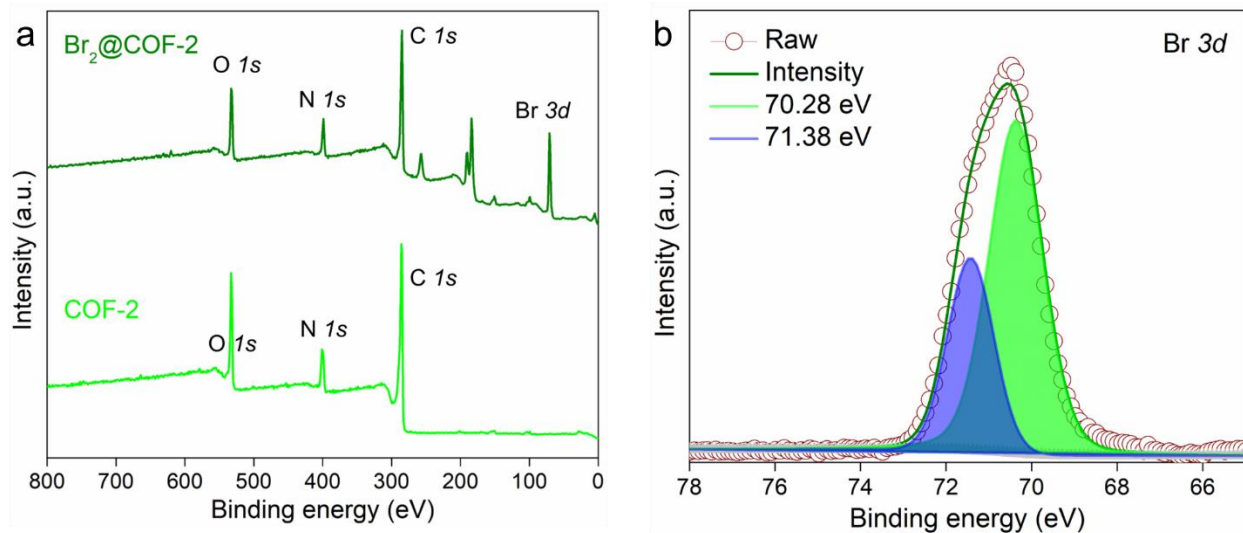
Figure S49: (a) XPS survey spectra of COF-2 and Br$_2$@COF-2, (b) Br 3d XPS spectra of COF-2 after Br$_2$ absorption test.
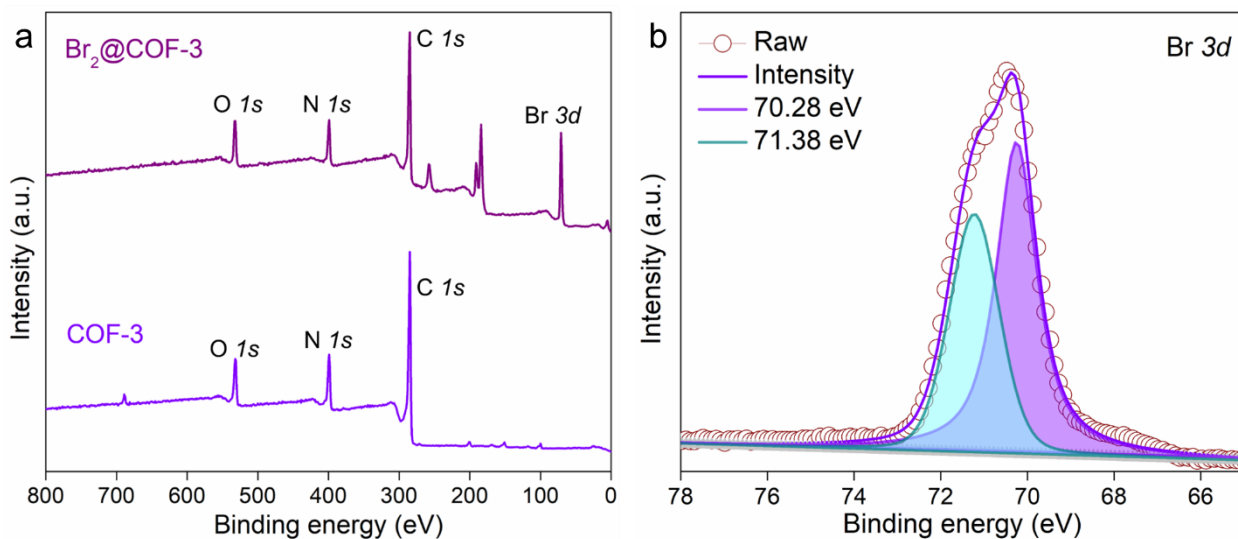
Figure S50: (a) XPS survey spectra of COF-3 and Br$_2$@COF-3, (b) Br 3d XPS spectra of COF-3 after Br$_2$ absorption test.
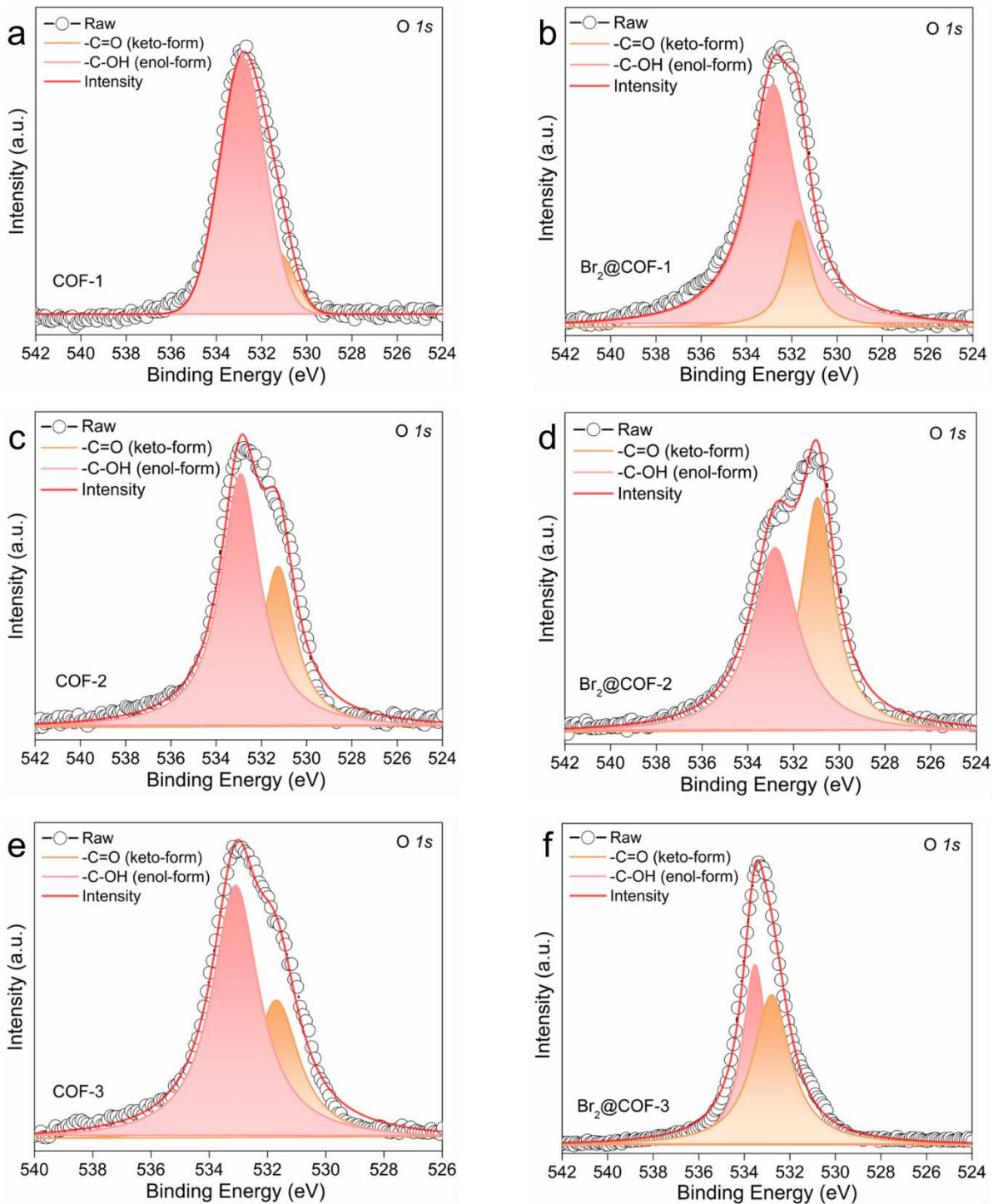
Figure S51: O 1s XPS spectra of COF-1 (a, b), COF-2 (c, d), and COF-3 (e, f) before and after Br_2 absorption test.
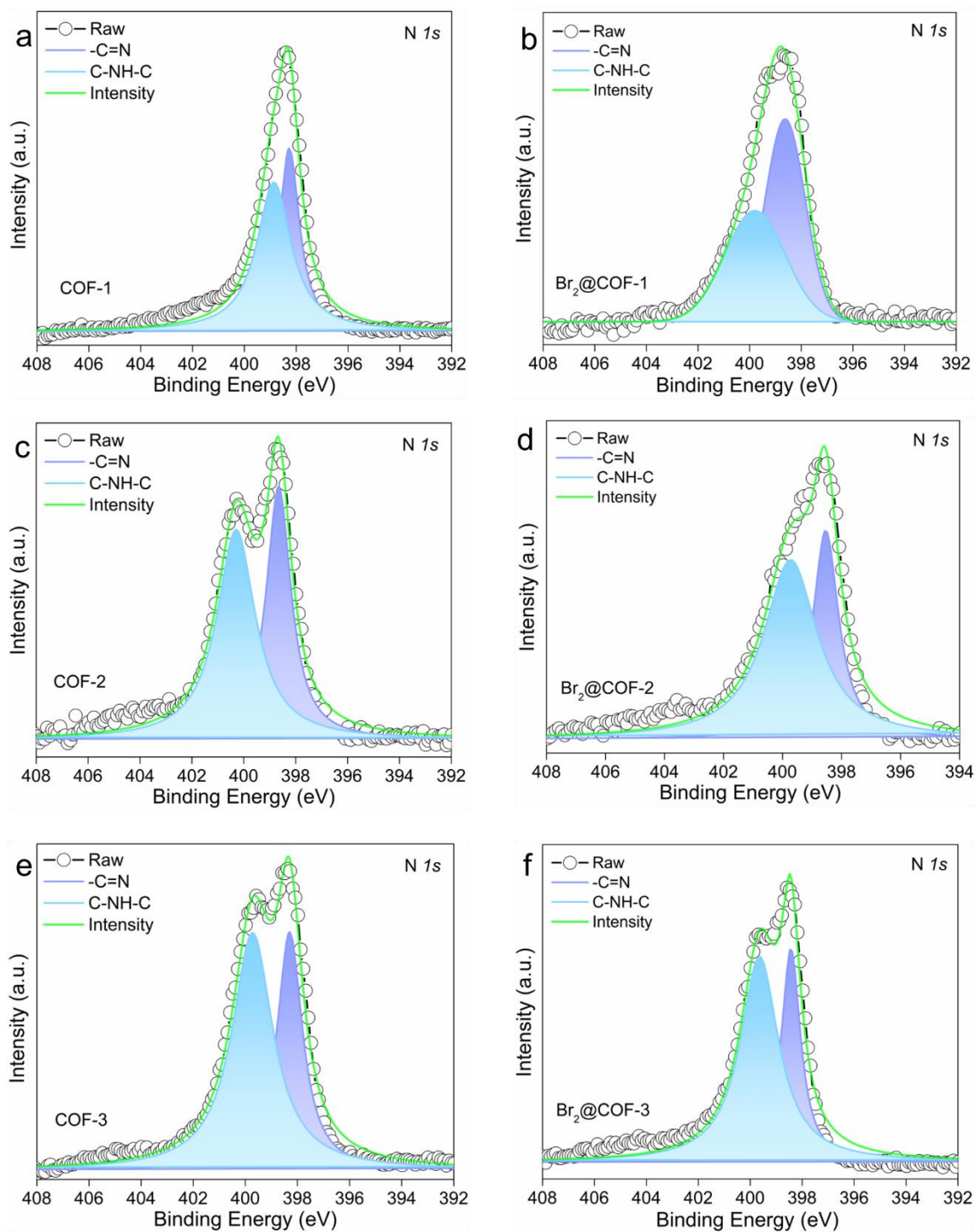
Figure S52: N 1s XPS spectra of COF-1 (a, b), COF-2 (c, d), and COF-3 (e, f) before and after Br_2 absorption test.
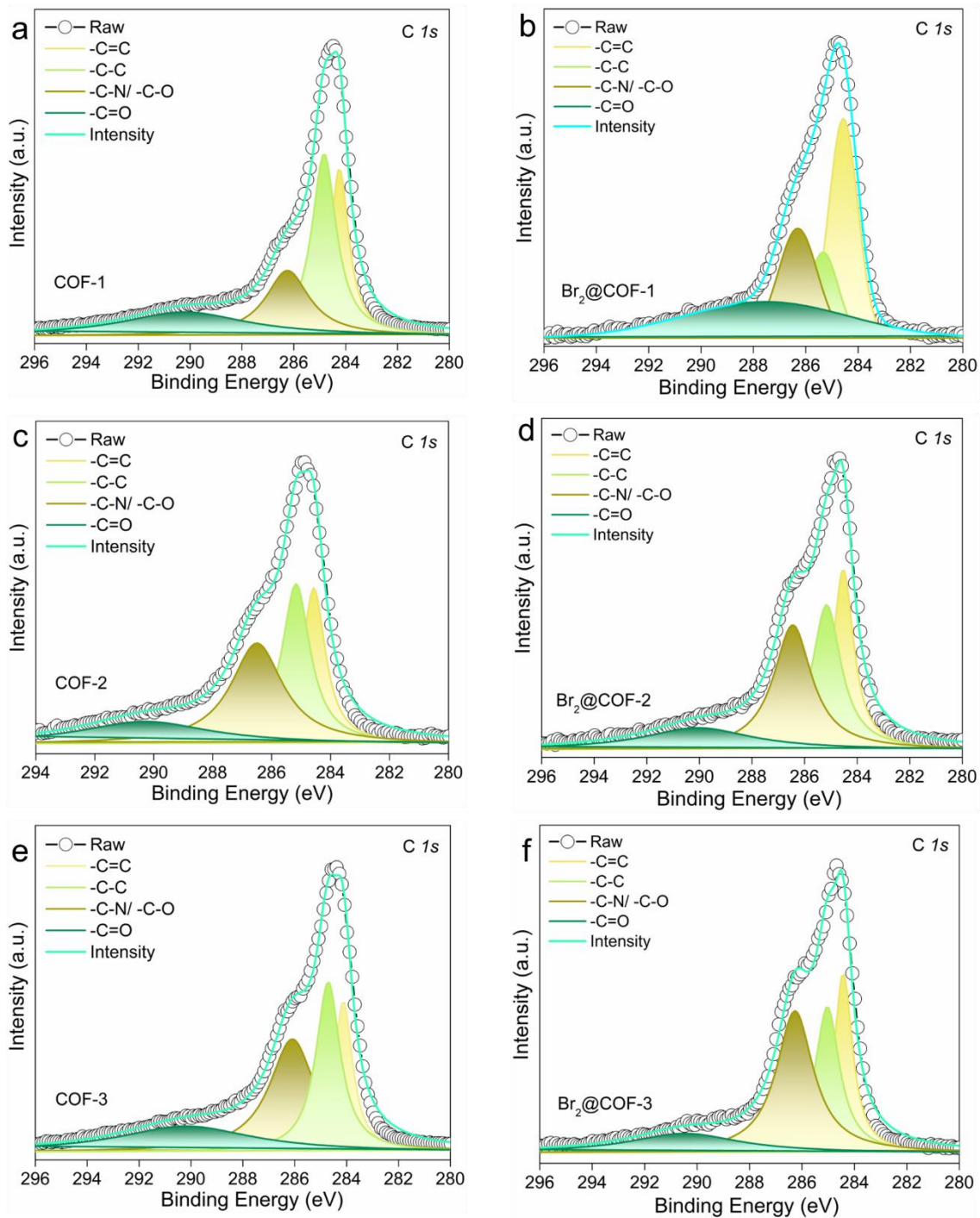
Figure S53: C 1s XPS spectra of COF-1 (a, b), COF-2 (c, d), and COF-3 (e, f) before and after Br_2 absorption test.
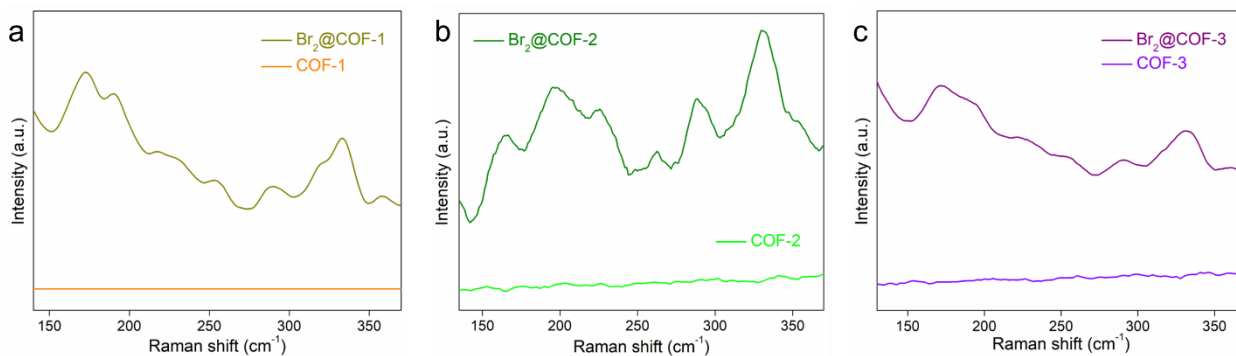
Figure S54: Raman spectra of (a) COF-1, (b) COF-2, and (c) COF-3 before and after Br_2 absorption test. The spectra of Br_2@COF-2 (as an example) exhibited major bands at 173, 190, 229, and 256 cm^{-1}, which are associated with symmetric stretching vibration of polybromide Br_3^- (173 cm^{-1}), asymmetric stretching vibration of polybromide Br_3^- (190 cm^{-1}), symmetric stretching vibration of polybromide Br_5^- and Br_2 molecules which have confinement effect (256 cm^{-1}).[13-16]
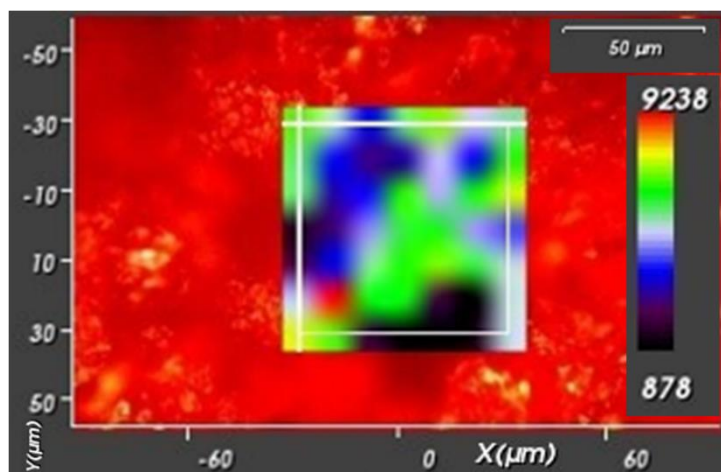
Figure S55: Raman spectroscopy image for mapping of COF-2 after Br_2 absorption test.
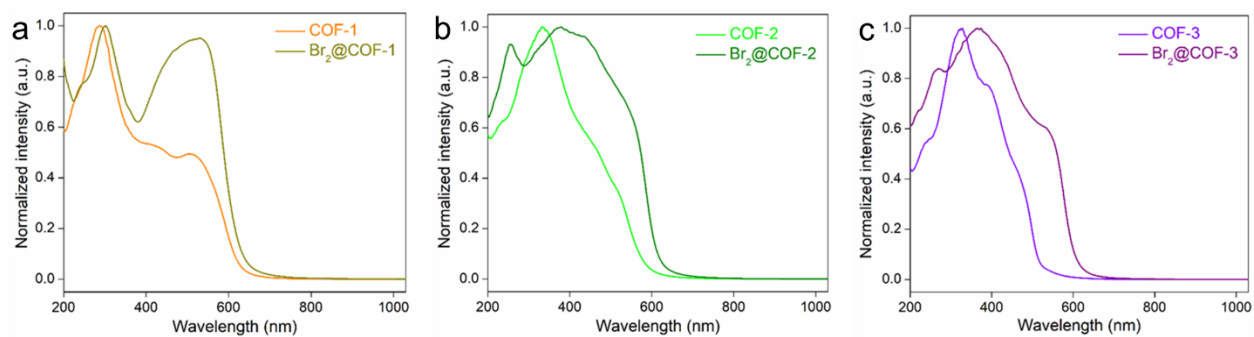
Figure S56: Solid-state UV-vis spectra of (a) COF-1, (b) COF-2, and (c) COF-3 before and after Br_2 absorption test.
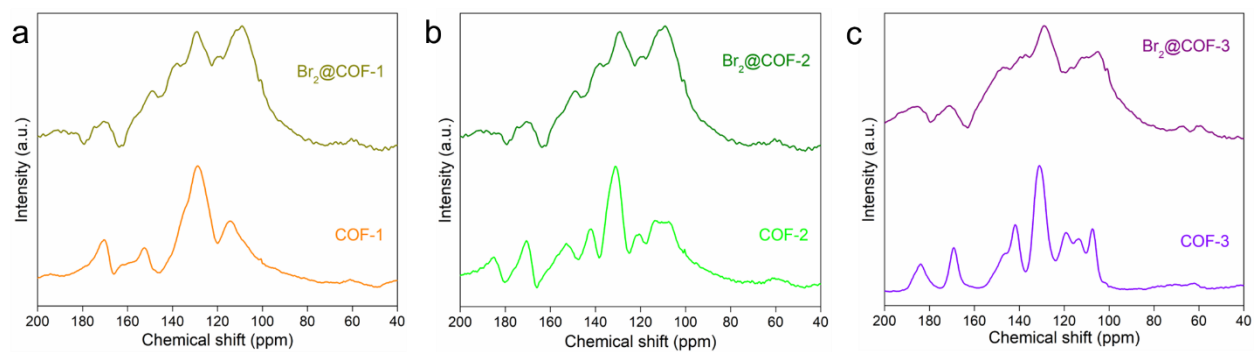
Figure S57: Solid-state ^{13}C CP-MAS NMR spectra of (a) COF-1, (b) COF-2, and (c) COF-3 before and after Br_2 absorption test.
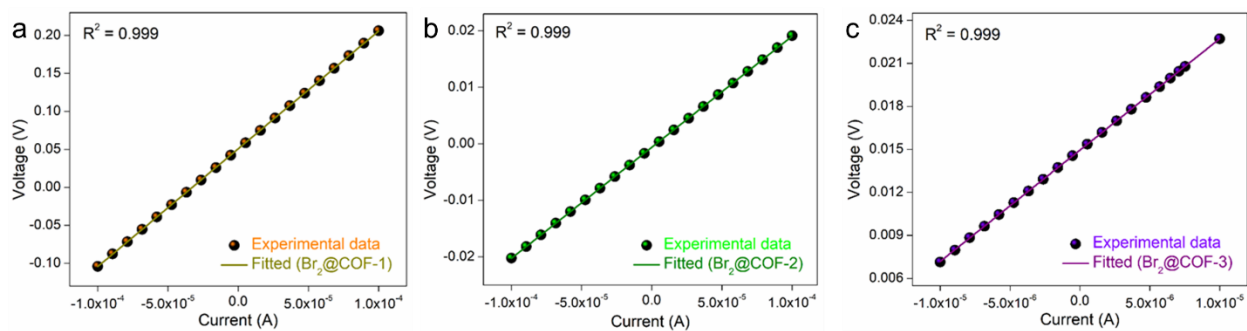
Figure S58: Conductivity measurement current-voltage (I-V) plots of (a) COF-1, (b) COF-2, and (c) COF-3 after Br₂ absorption test.
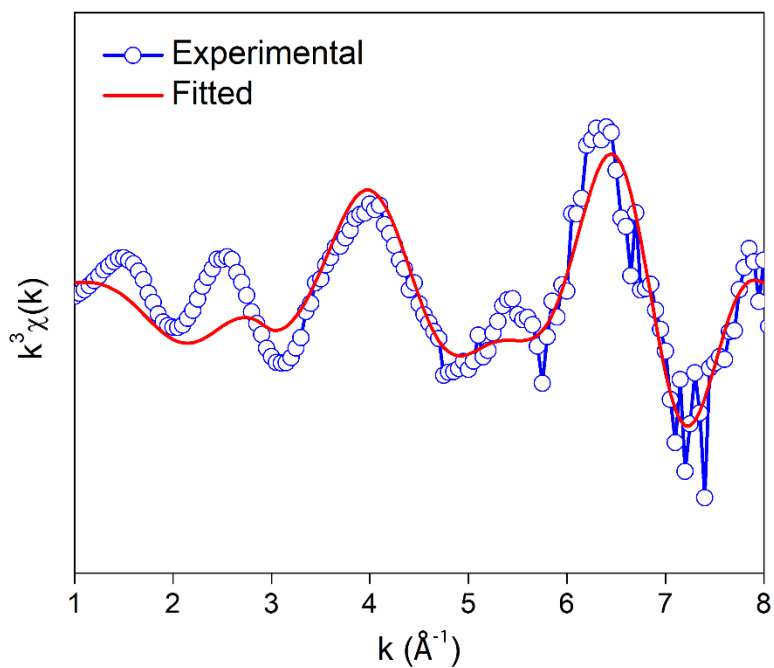
Figure S59: Br K-edge spectra of bromine loaded COF-2 sample.

Table S2: EXAFS fitting parameters at the Br K-edge for COF-2 sample after Br_2 adsorption.

Sample	Shell	N	R (Å)	σ^2 (Å^2)	ΔE_0 (eV)	R factor
Br_2@COF-2	Br-C1	1	1.869 +/- 0.018	0.002 +/- 0.001	0.222 +/- 3.553	0.0203
	Br-C1	2	2.842 +/- 0.026	0.009 +/- 0.004		
	Br-C2	4	3.032 +/- 0.018	0.002 +/- 0.001		
	Br-C2	2	3.167 +/- 0.032	0.004 +/- 0.004		

N: coordination number; R: bond distance; σ^2: Debye-Waller factor; ΔE_0: the inner potential correction. R factor: goodness of fit. S_0^2 was set as 0.85.
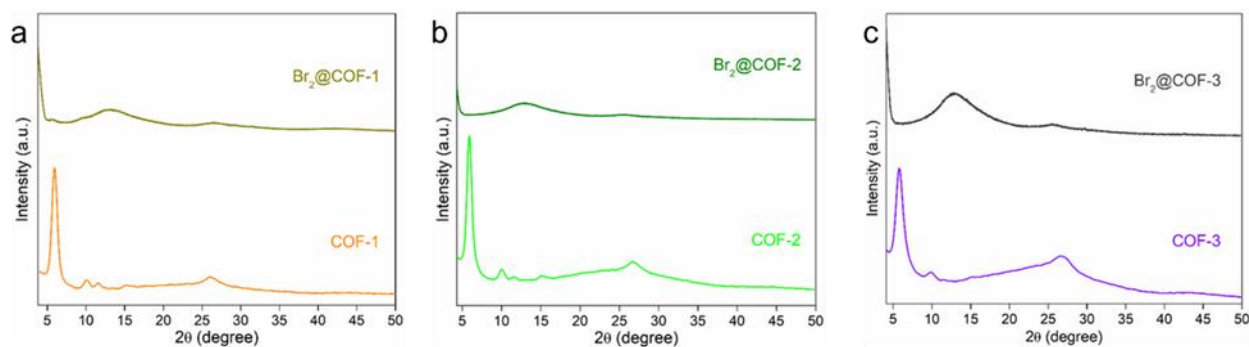
Figure S60: PXRD profiles of (a) COF-1, (b) COF-2, and (c) COF-3 before and after Br_2 absorption test.
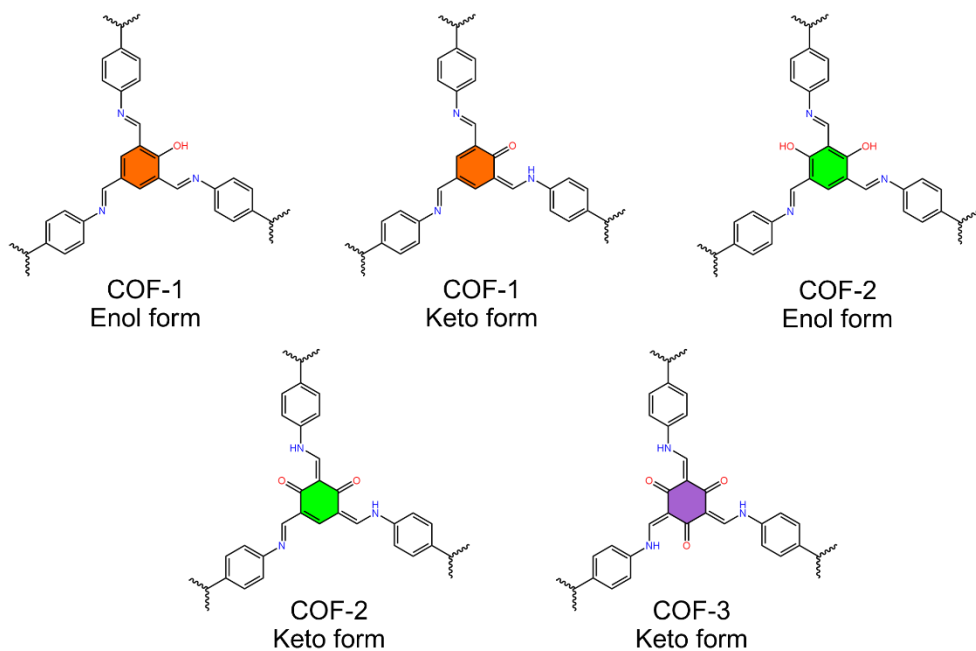
Figure S61: Chemical structures of representative units of COF-1, COF-2 and COF-3.
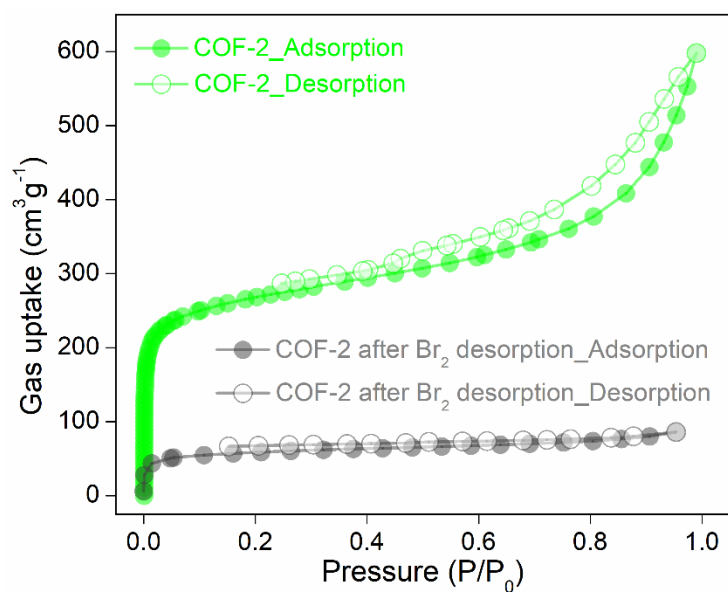
Figure S62: Nitrogen gas sorption data of pristine COF-2 and COF-2 after Br$_2$ desorption test.

Section S7: Theoretical calculation studies

Determination of electrostatic surface potential (ESP), binding sites and binding energy of different interactions:

Discovery Studio 2016 (Accelrys) have been used to perform the structural simulation to determine binding energy of interactions electrostatic – potential surface (ESP) and binding sites.[17, 18] Firstly, the molecular structure of the COFs unit was fully relaxed using DMOL3 using B3LYP hybrid function by keeping Multiplicity function in Auto mode, double numeric plus polarizing (DNP) basis set and water as solvent. Further, structural simulation on the relaxed structure was performed using single – point energy calculations at a fine-quality calculation level.

To locate the initial position of the bromine molecule in the monomer unit of COF-1, COF-2 and COF-3, simulated annealing technique was used. The static binding energies (ΔE) at 0 K in vacuum were calculated using the following expression

$$\Delta E = E_{COF+Bromine} - E_{COF+} - E_{Bromine}$$

where Ex refers, to the total energies of the COF + Bromine complex, the charged COF_+ alone, and the bromine molecule respectively.

The electrostatic potential (ESP) on the van der Waals (VDW) surfaces (isodensity = 0.001 a.u.) of units of COF-1, COF-2 and COF-3 were derived based on its ground state electron density.
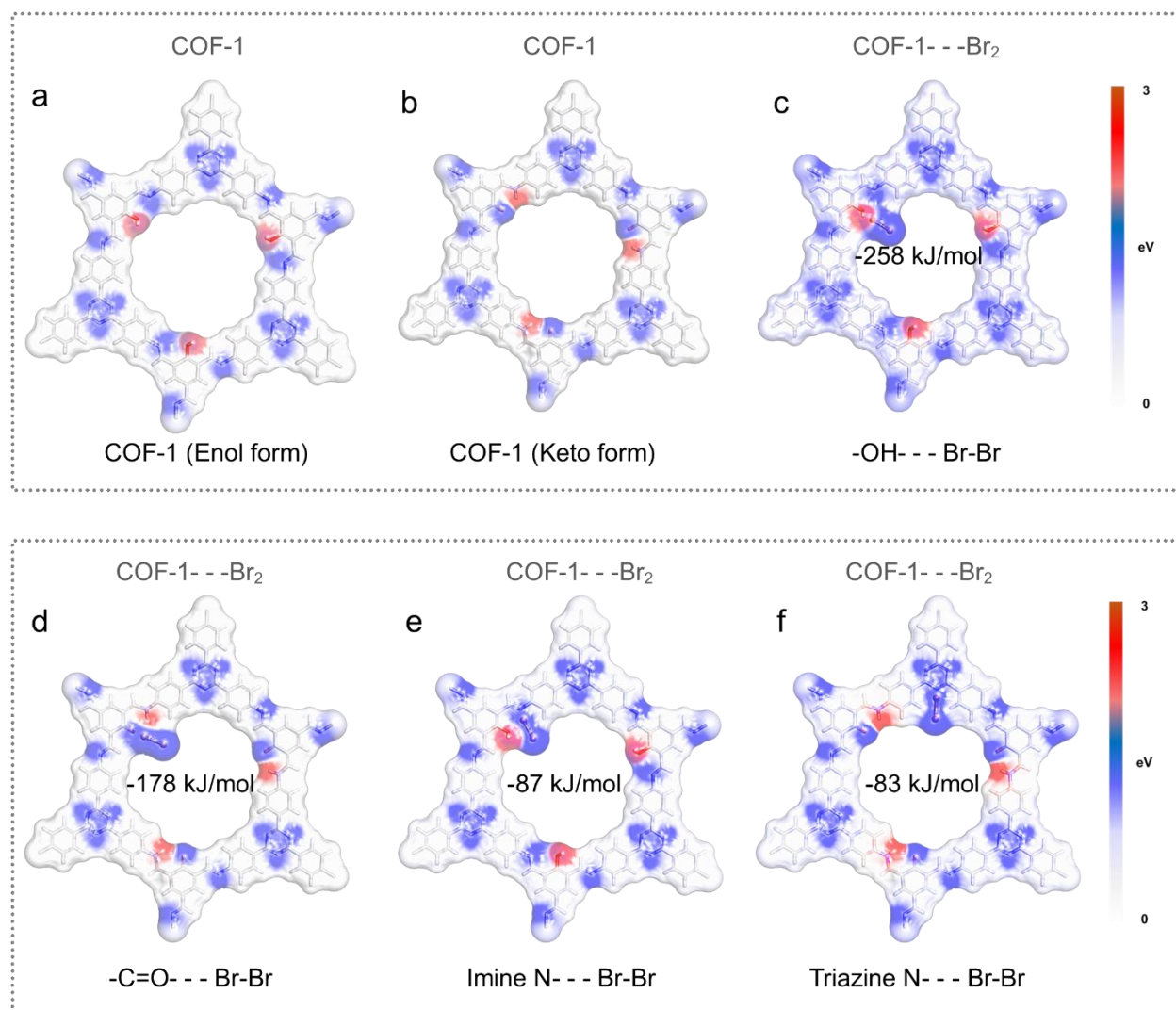
Figure S63: Electrostatic Potential (ESP) diagram of the DFT optimized structures with respective binding energies of different interactions between the structural units of COF-1 with bromine molecule. (a) COF-1 enol form, (b) COF-1 keto form, (c-f) Interaction between bromine and (c) –OH group, (d) –C=O group, (e) imine-N, (f) triazine-N of COF-1.
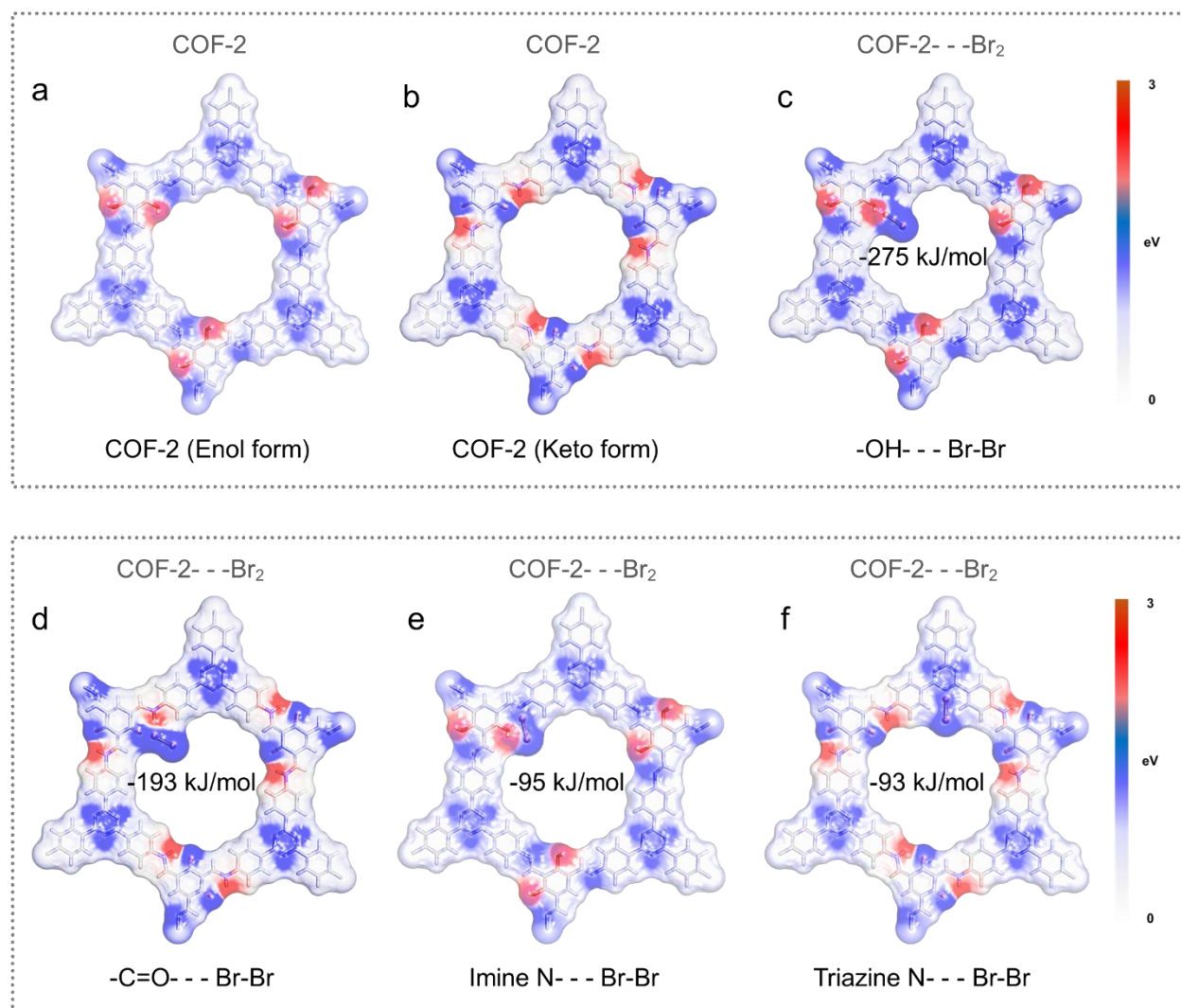
Figure S64: Electrostatic Potential (ESP) diagram of the DFT optimized structures with respective binding energies of different interactions between the structural units of COF-2 with bromine molecule. (a) COF-2 enol form, (b) COF-2 keto form, (c-f) Interaction between bromine and (c) –OH group, (d) –C=O group, (e) imine-N, (f) triazine-N of COF-2.
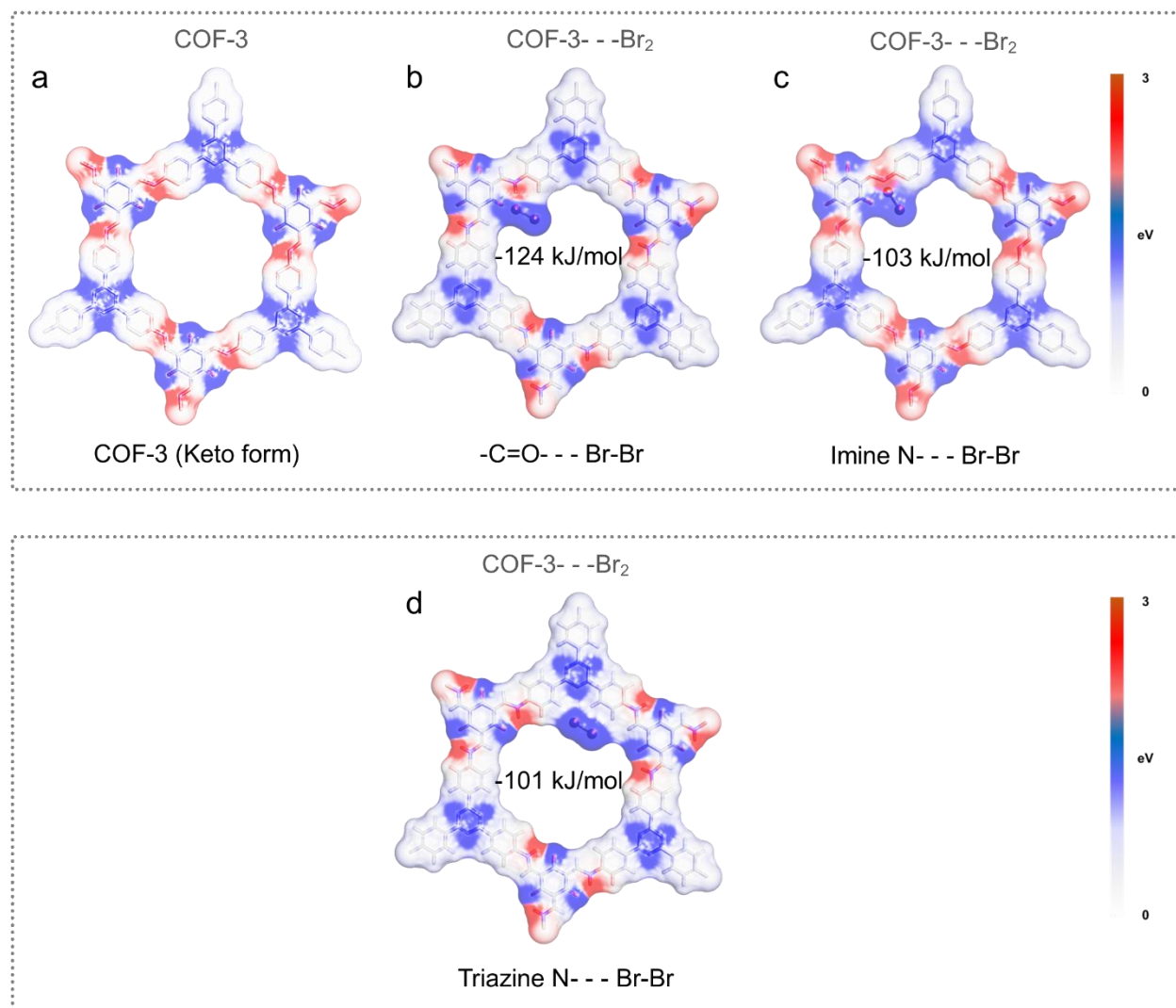
Figure S65: Electrostatic Potential (ESP) diagram of the DFT optimized structures with respective binding energies of different interactions between the structural units of COF-3 with bromine molecule. (a) COF-3 keto form, (b-d) Interaction between bromine and (b) –C=O group, (c) imine-N, (d) triazine-N of COF-3.

Section S8: Solution phase bromine capture studies
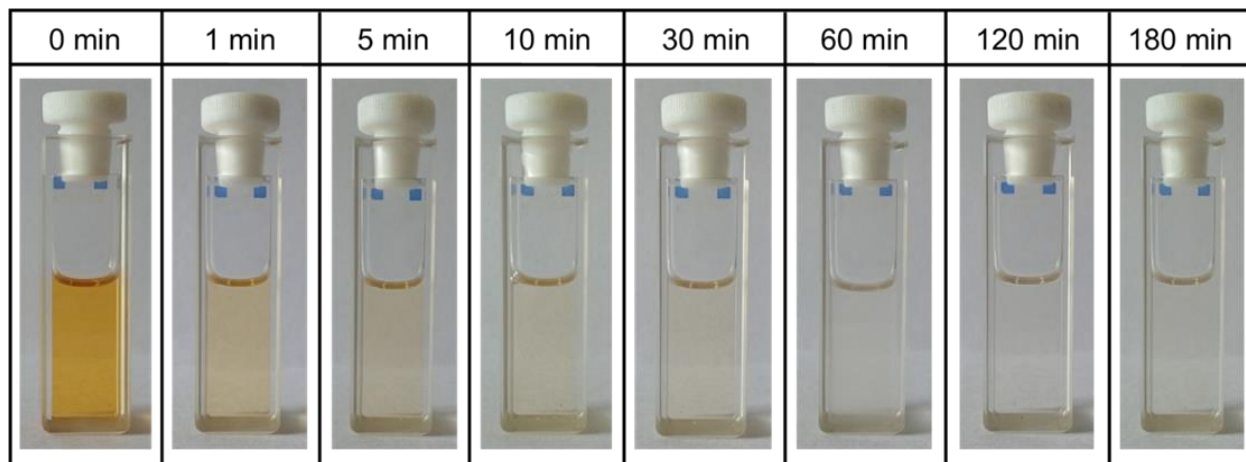
Figure S66: Digital images of decrease in the concentration of Br_2 in cyclohexane solution with time upon treatment with COF-2.
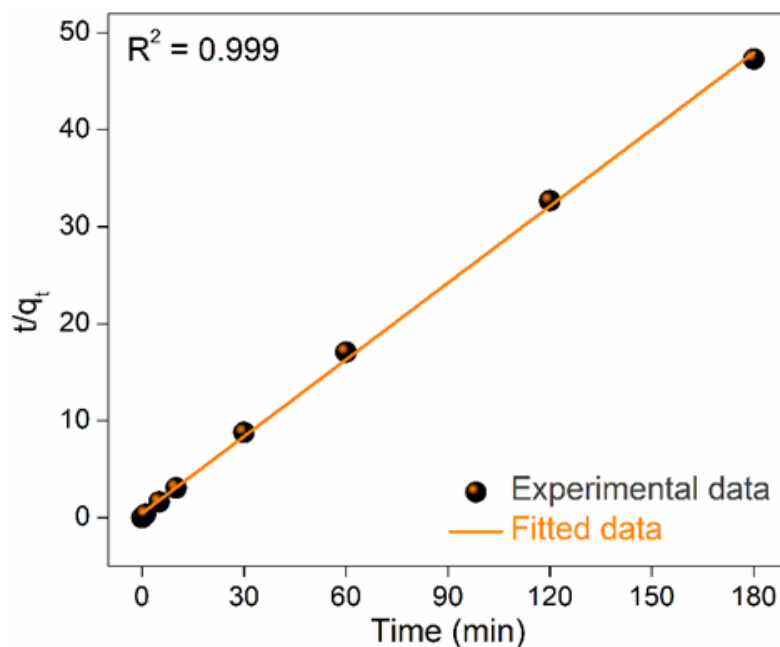
Figure S67: Pseudo-second-order kinetic model fitting plots for capture of bromine in cyclohexane solution by COF-2.
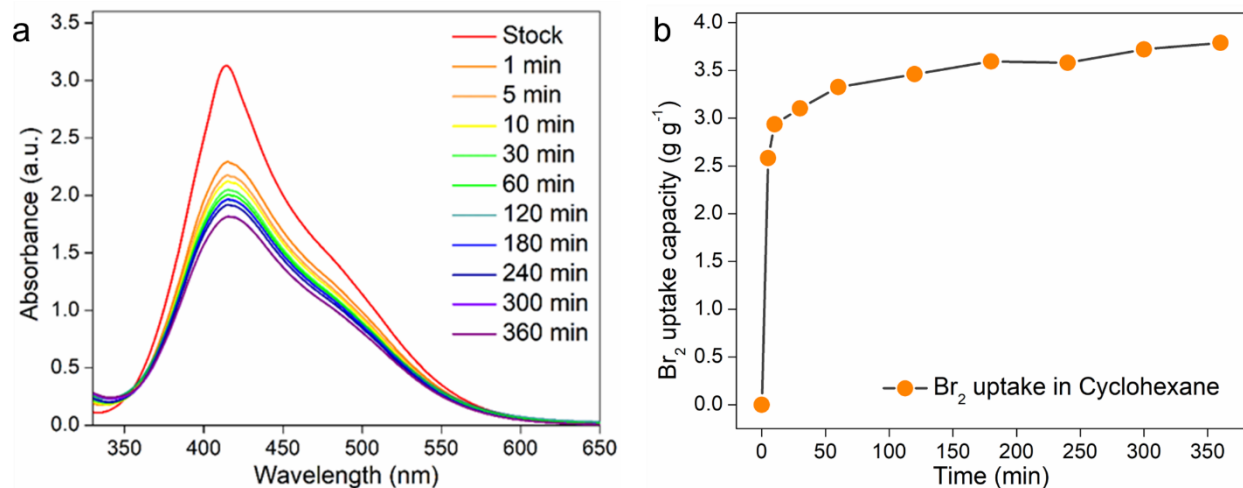
Figure S68: **(a)** Time-dependent UV-vis spectra of bromine (Br$_2$) in cyclohexane (20 milimolar) showing dismissing by the treatment of COF-2, (b) Br$_2$ uptake capacities in cyclohexane with incremental time.

Table S3: Comparison table of bromine adsorption capacities in cyclohexane for various adsorbents.

Adsorbents	Type of material	Capacity (g.g^{-1})	Reference
COF-2	COF	3.92	This work
C4P-POP	POP	3.4	*J. Am. Chem. Soc.* 2022, **144**, 16755-16760.
UiO-67	MOF	1.9	*Angew. Chem. Int. Ed.* 2017, **56**, 14622-14626.
PCN-700	MOF	2.6	*Angew. Chem. Int. Ed.* 2017, **56**, 14622-14626.
PCN-605-H	MOF	4.2	*Angew. Chem. Int. Ed.* 2017, **56**, 14622-14626.
PCN-606-OMe	MOF	3.7	*Angew. Chem. Int. Ed.* 2017, **56**, 14622-14626.
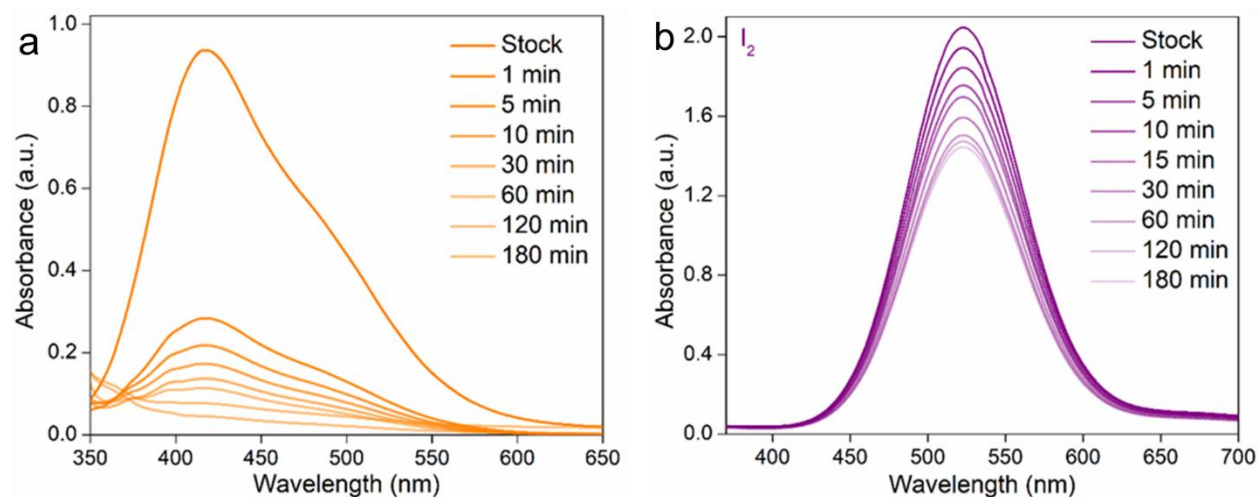
Figure S69: Time-dependent UV-vis spectra of (a) bromine (Br_2) and (b) iodine (I_2) in cyclohexane showing dismissing by the treatment of COF-2 with incremental time.
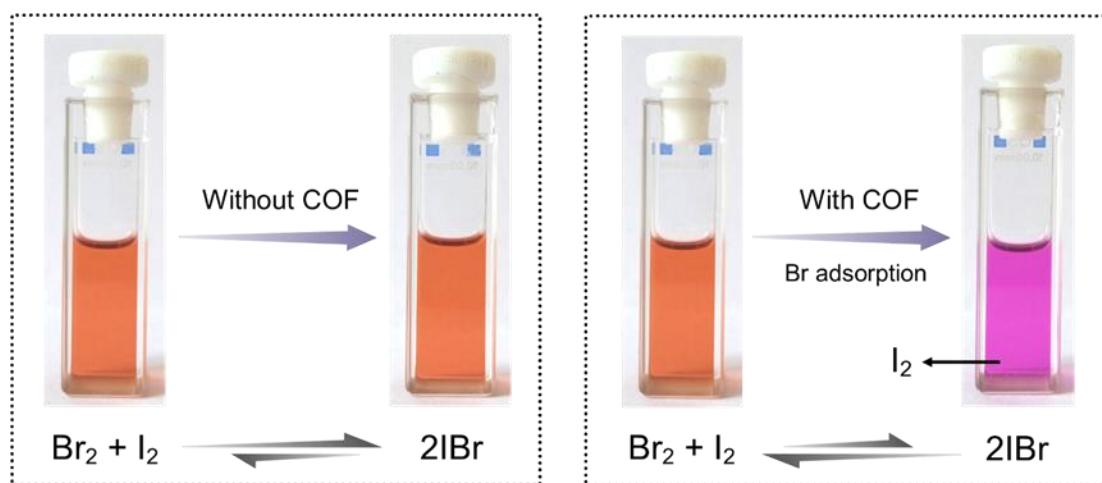
Figure S70: Digital images of color changes observed during selective Br_2 adsorption test from a mixture of Br_2+I_2+IBr solution in cyclohexane.
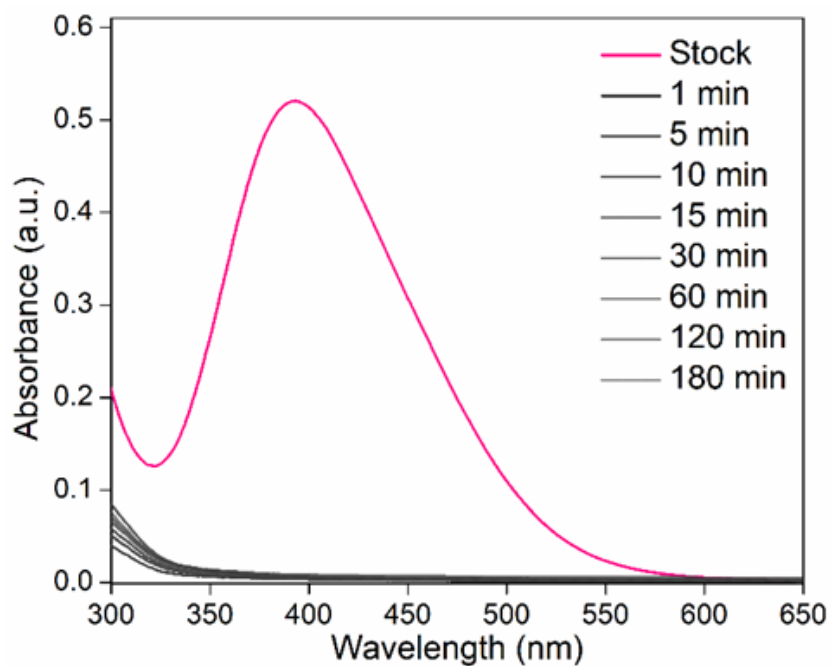
Figure S71: Time-dependent UV-vis spectra of bromine in water showing dismissing by the treatment of COF-2 with incremental time.
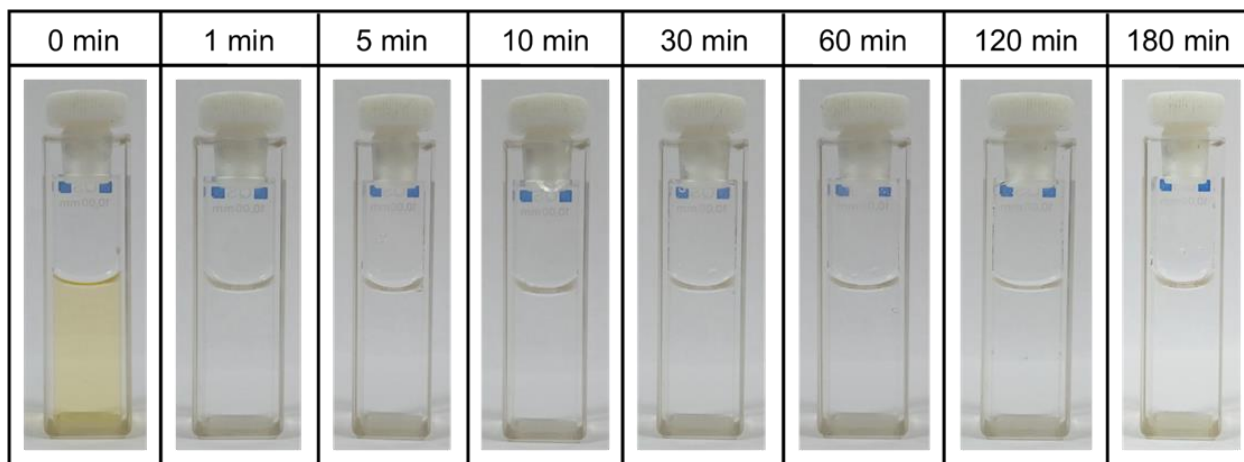
Figure S72: Digital images of decrease in the concentration of Br_2 in water with time upon treatment of COF-2.
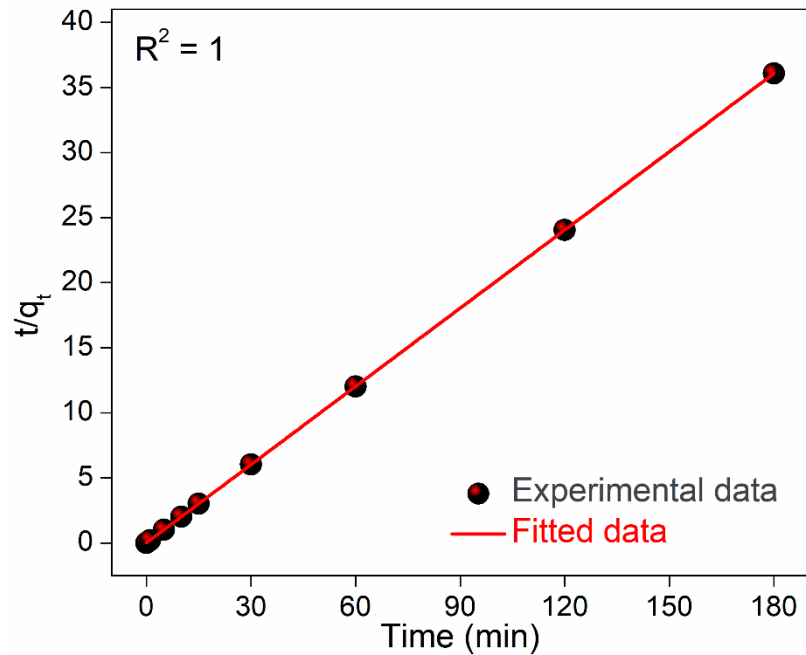
Figure S73: Pseudo-second-order kinetic model fitting plots for capture of bromine in water by COF-2.
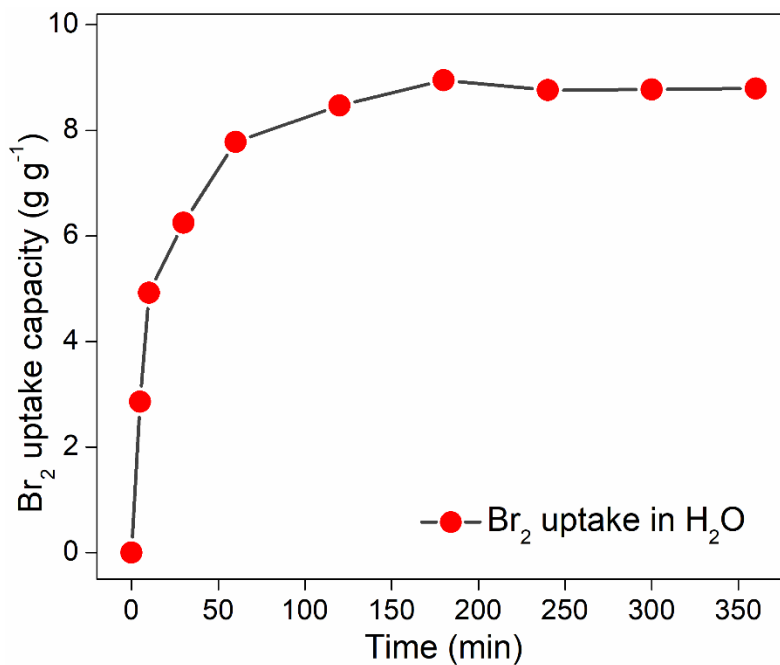
Figure S74: Br$_2$ uptake capacities in water with incremental time.
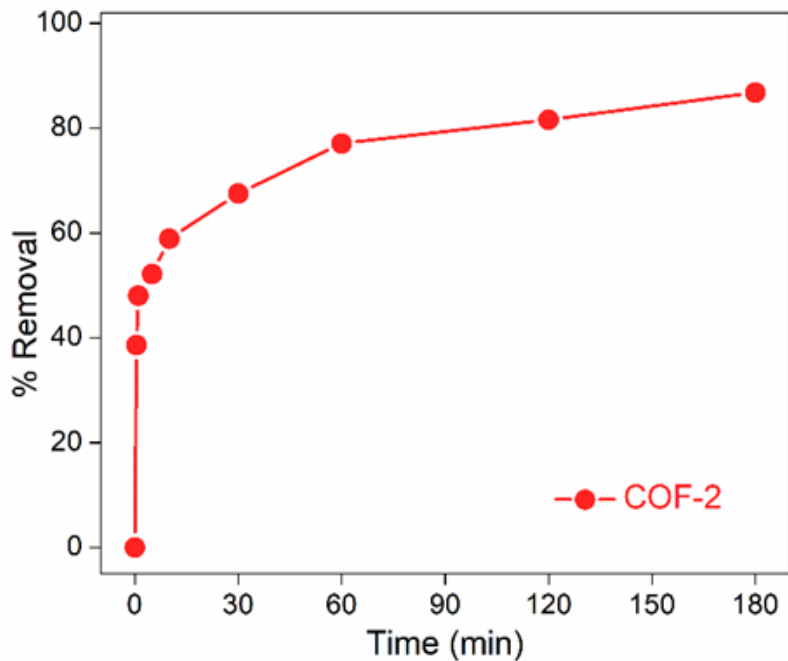
Figure S75: Low concentration Br_2 removal efficiency in water by COF-2 with incremental time.
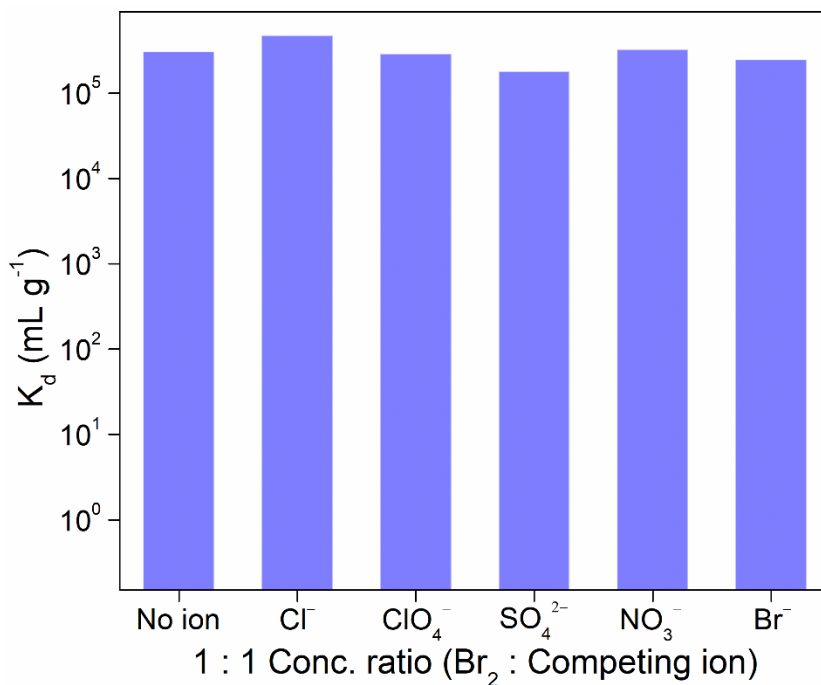
Figure S76: Distribution coefficient (K_d) data of COF-2 for Br_2 removal in water in the presence of other anions.

Section S9: Membrane preparation and characterizations

Synthesis of COF-2 thin-film/membrane: COF-2 membrane was prepared taking help from previously reported protocol by Ma et al.[3] At first, 19.4 mg (0.1 mmol) of 2,4-dihydroxybenzene-1,3,5-tricarbaldehyde (DHTA) was dissolved in 80 mL dichloromethane in a 250 mL glass beaker to give the aldehyde solution; then 3 M acetic acid solution was added slowly until the surface of aldehyde solution was completely covered. Thereafter, solution of 2,4,6-tris(4-aminophenyl)-1,3,5-triamine (TAPT) was prepared by dissolving 35.4 mg of TAPT in 50 mL DMF. Next, the solution amine was added dropwise to the surface of acetic acid + aldehyde solution. Following a three-day period at RT, the product was collected and properly cleaned using ethanol, dichloromethane, acetone, and DMF and used for further studies (Figure S77).
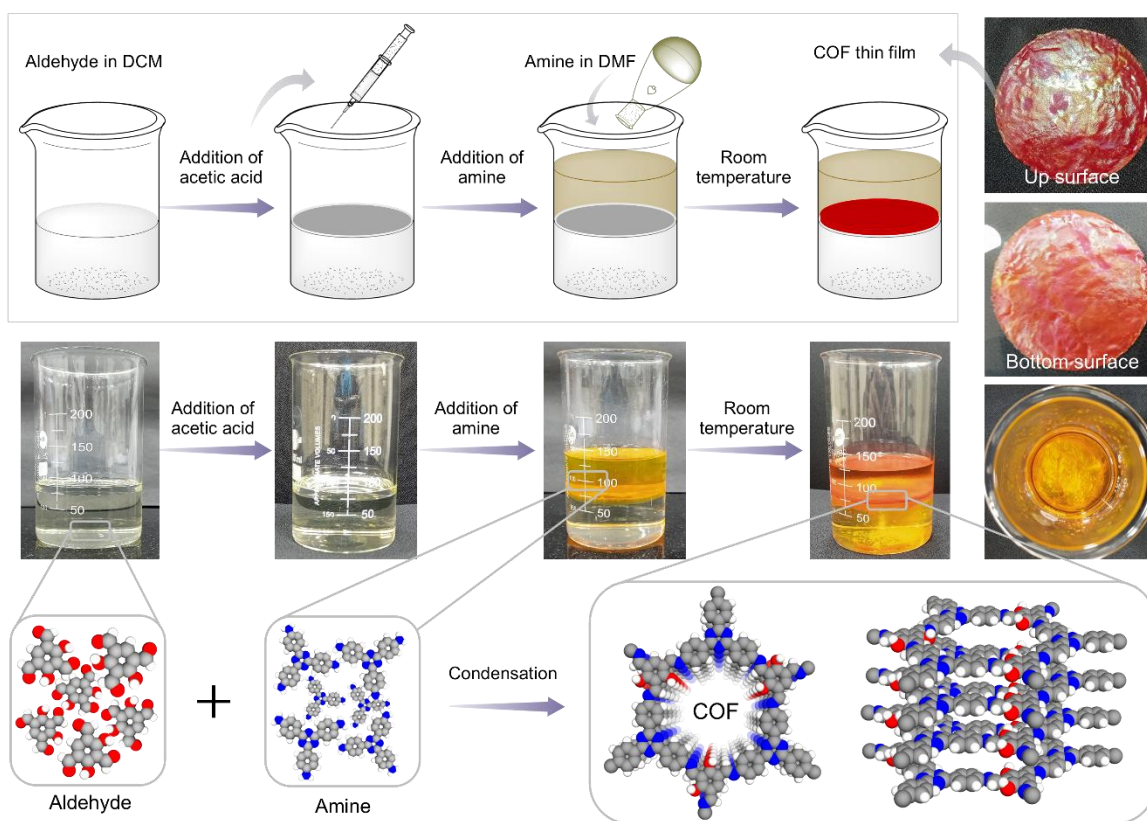
Figure S77: Schematic representation of fabrication of COF-2 based membrane via single step dual organic phase interfacial crystallization method.
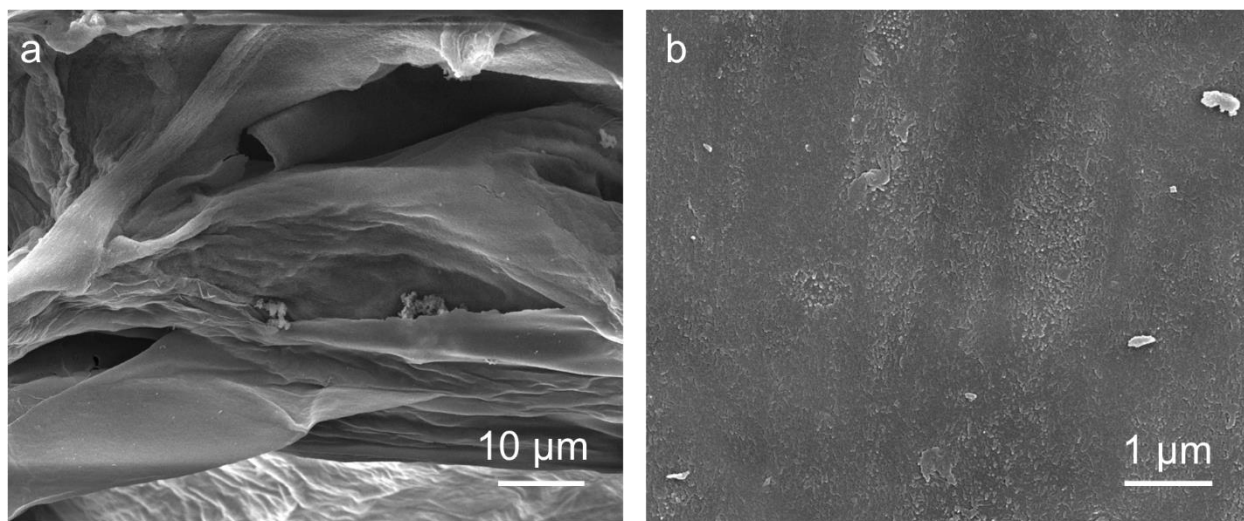
Figure S78: FESEM images of COF-2-TF, (a) cross-sectional view and (b) top view.
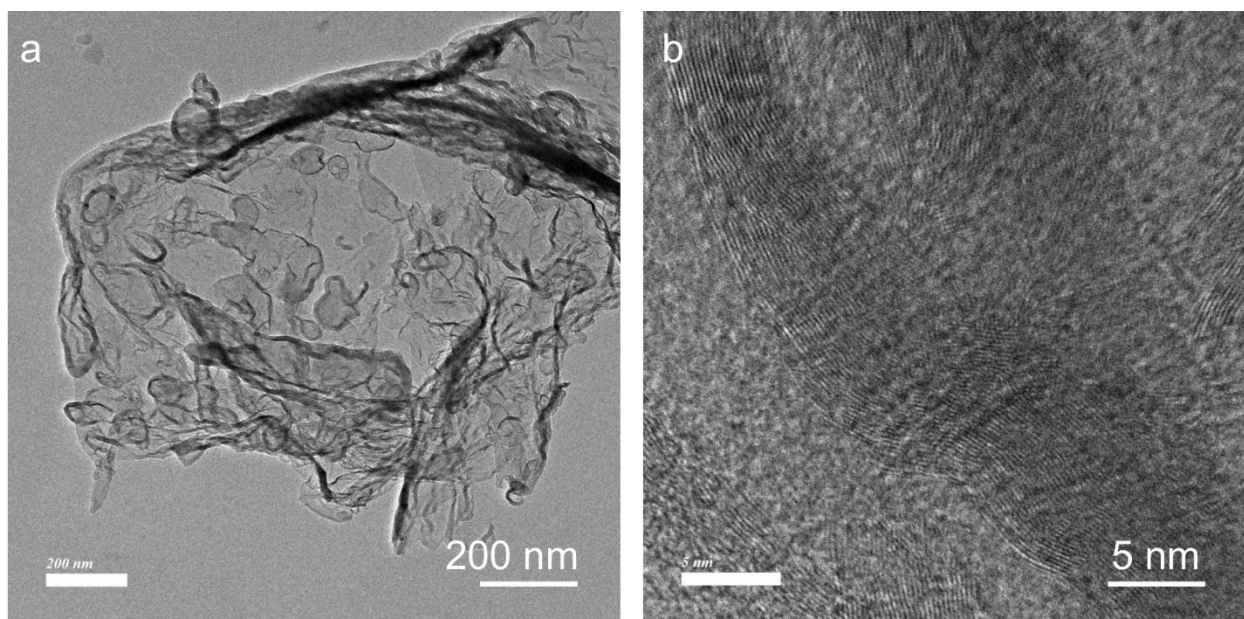
Figure S79: (a) TEM and (b) HRTEM images of COF-2-TF.
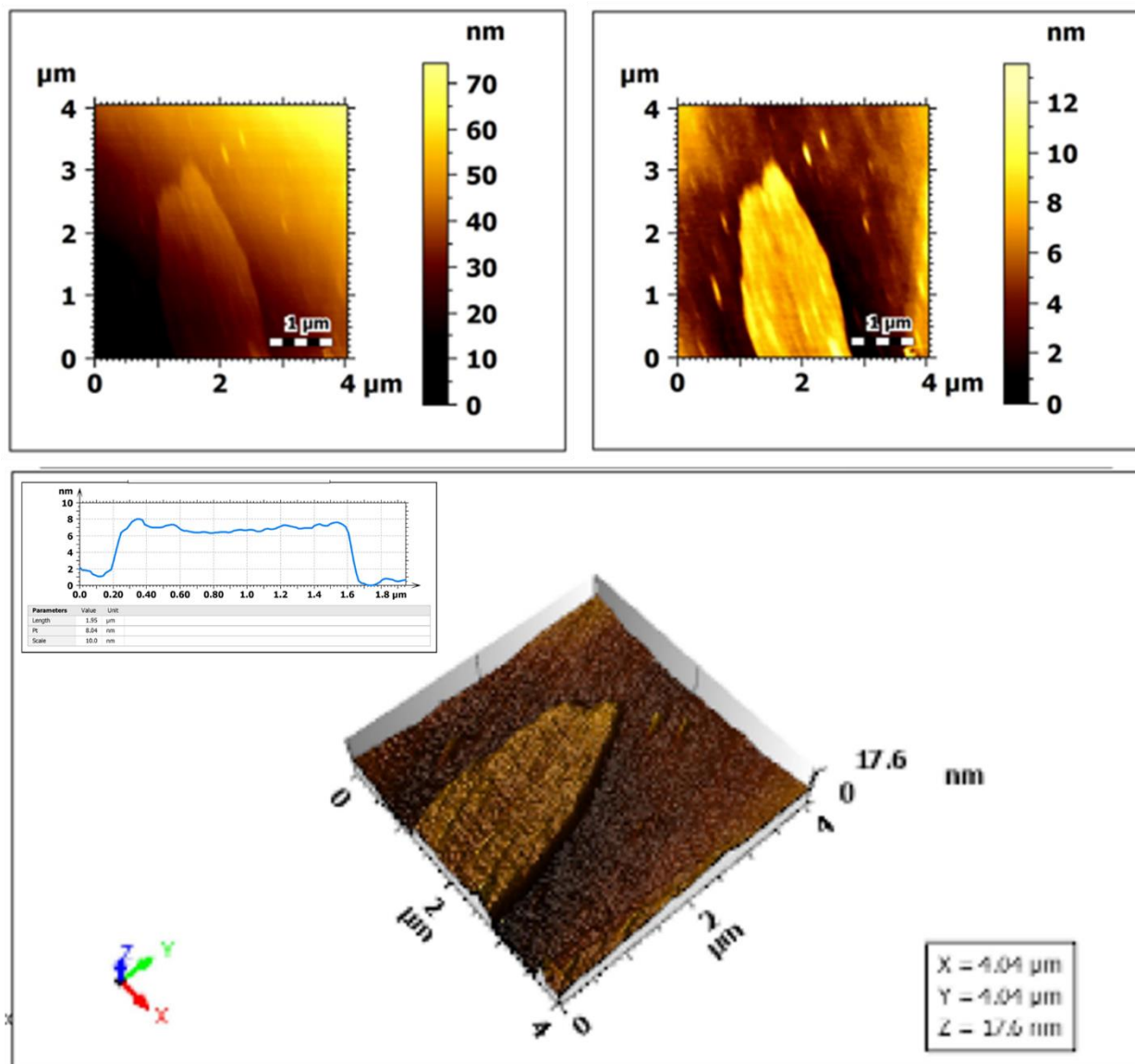
Figure S80: AFM images of COF-2-TF and its corresponding height profile.
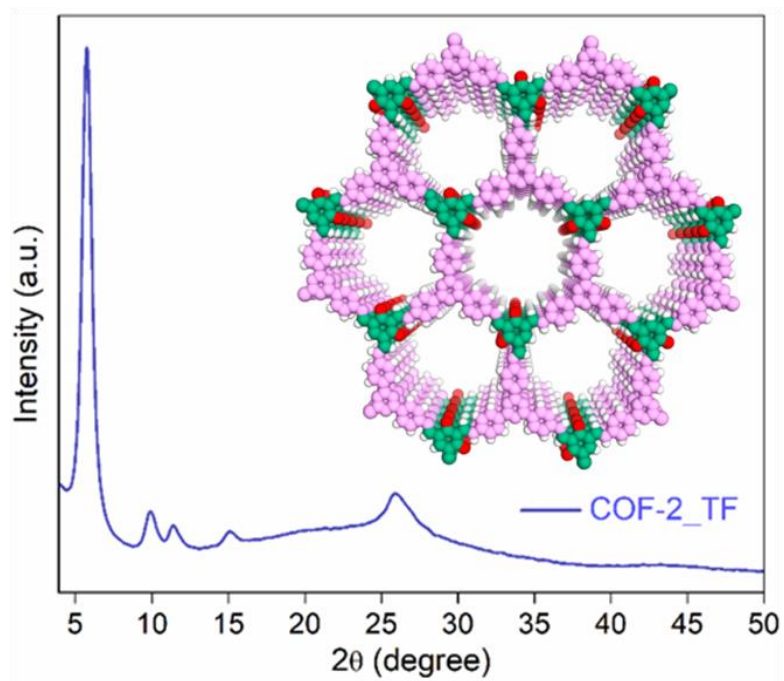
Figure S81: PXRD pattern of COF-2-TF.
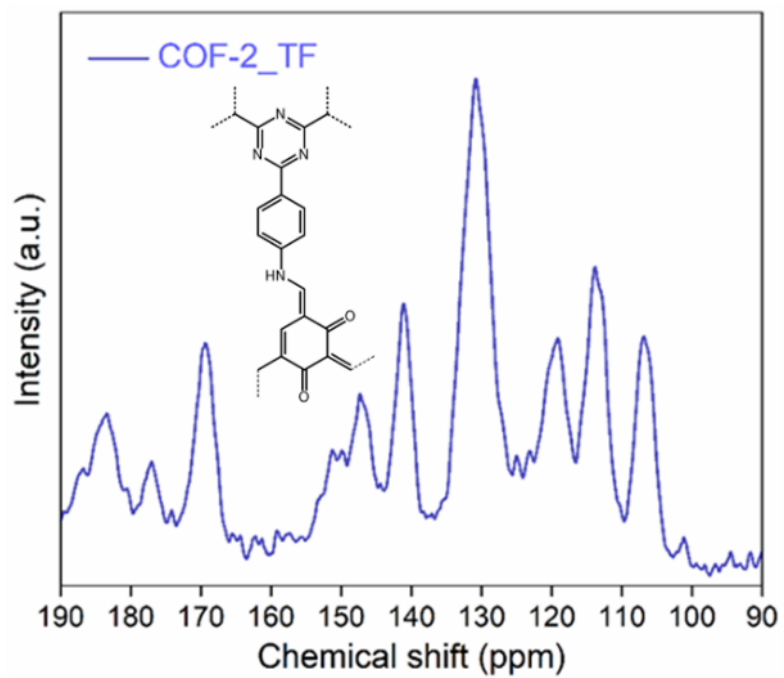
Figure S82: [13]C CP-MAS spectra of COF-2-TF.
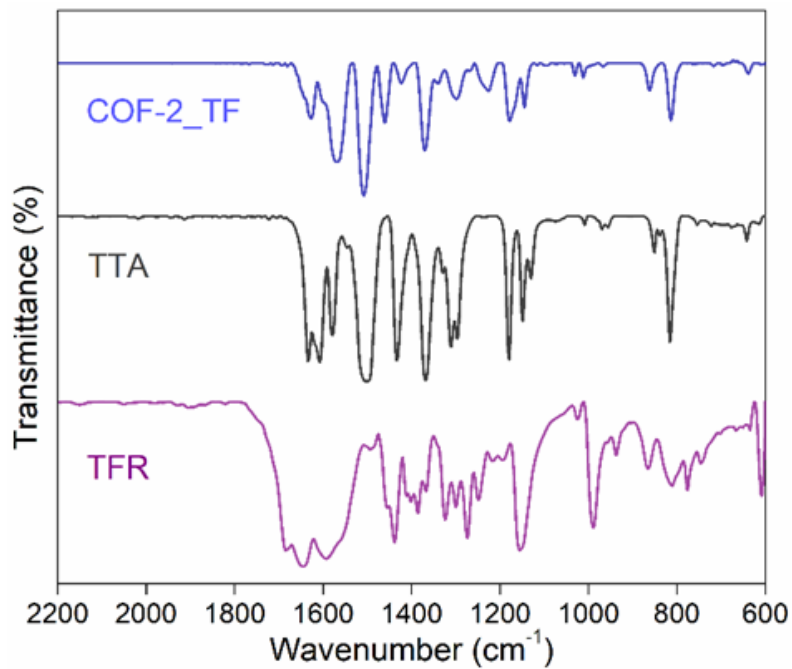
Figure S83: FT-IR spectra of COF-2-TF and its corresponding monomers.
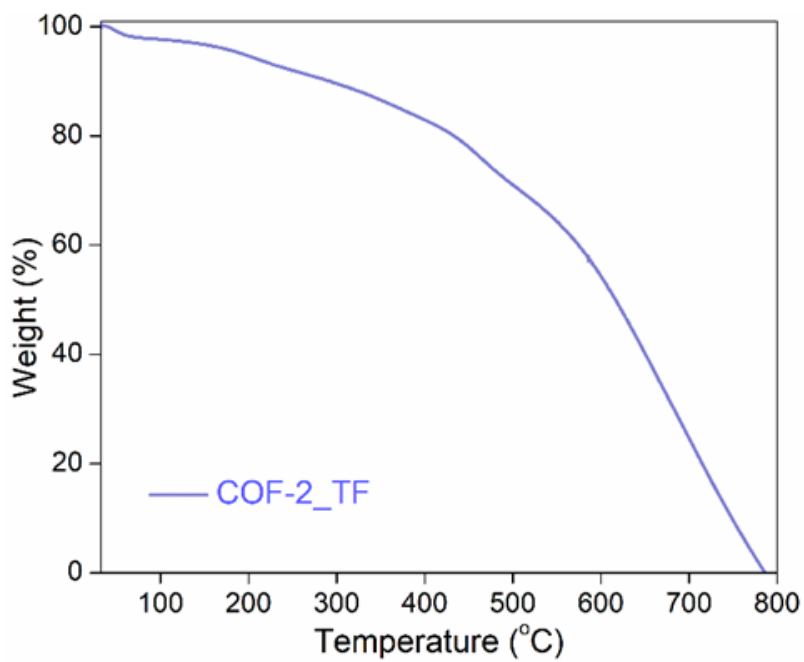
Figure S84: TGA profile of COF-2-TF.
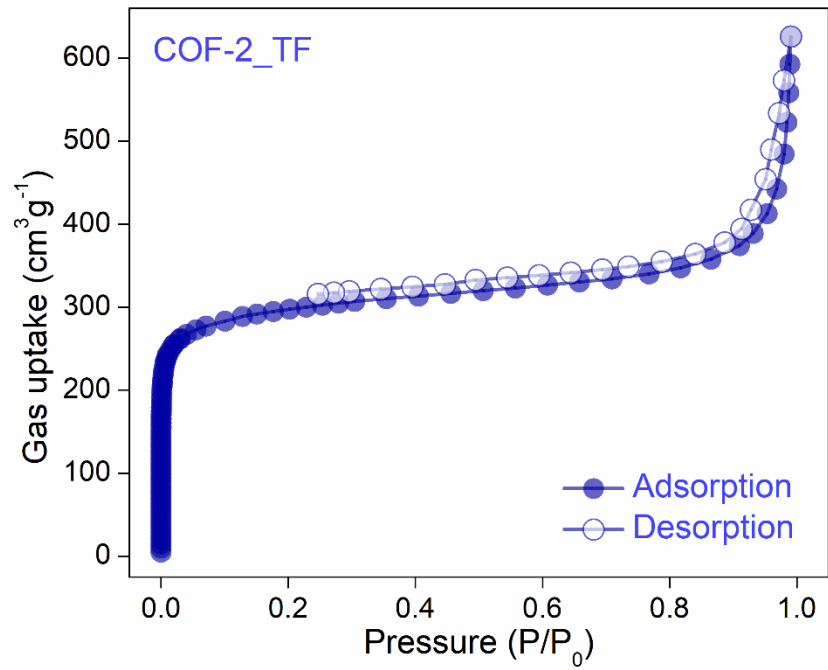
Figure S85: Nitrogen gas sorption data at 77 K of COF-2-TF.

Section S10: COF-2 based membrane preparation and flow-through bromine capture

Fabrication of COF-2 composite membrane: A vacuum-assisted self-assembly method was used to create the COF-2 composite membrane. Using a standard procedure, a portion of the as-synthesized COF-2 was mixed with about 100 mL of deionized water, and then the mixture was subjected to ultrasonic treatment for five to six hours to make a COF suspension. Then, using a vacuum-assisted self-assembly technique, the as-prepared COF colloidal suspension was transferred to a commercial nylon membrane to create the substrate-supported membrane (COF-2 composite membrane).
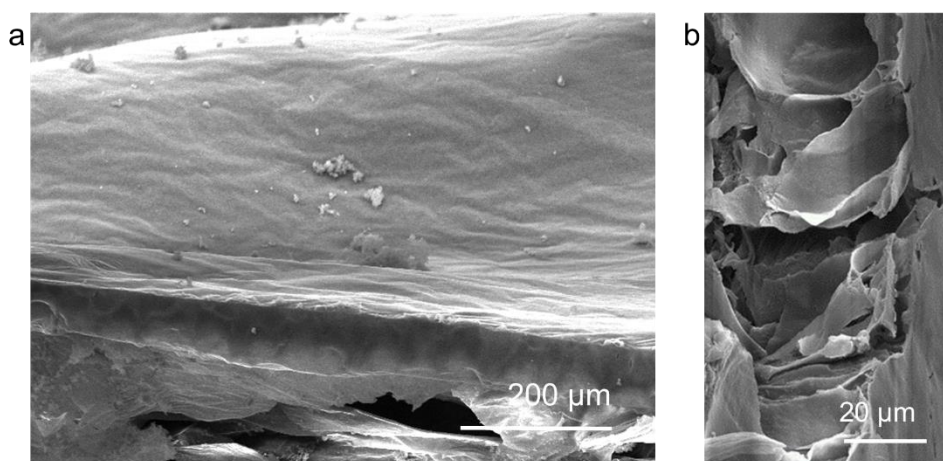
Figure S86: (a) Top-view and (b) cross-section FESEM images of COF-2 membrane.
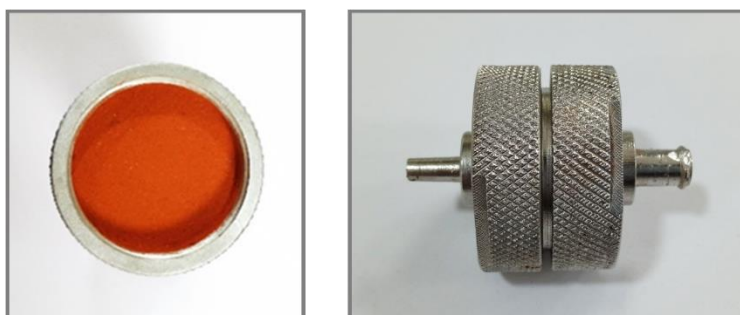
Figure S87: Image of COF-2 membrane installed in to a separation chamber.
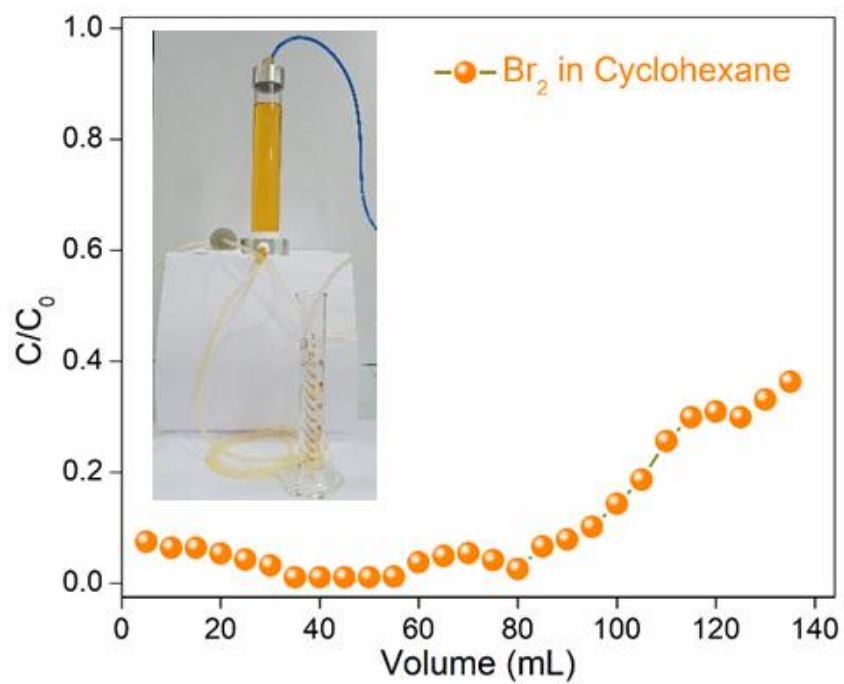
Figure S88: Result of dynamic Br$_2$ capture test in cyclohexane using COF-2-membrane.
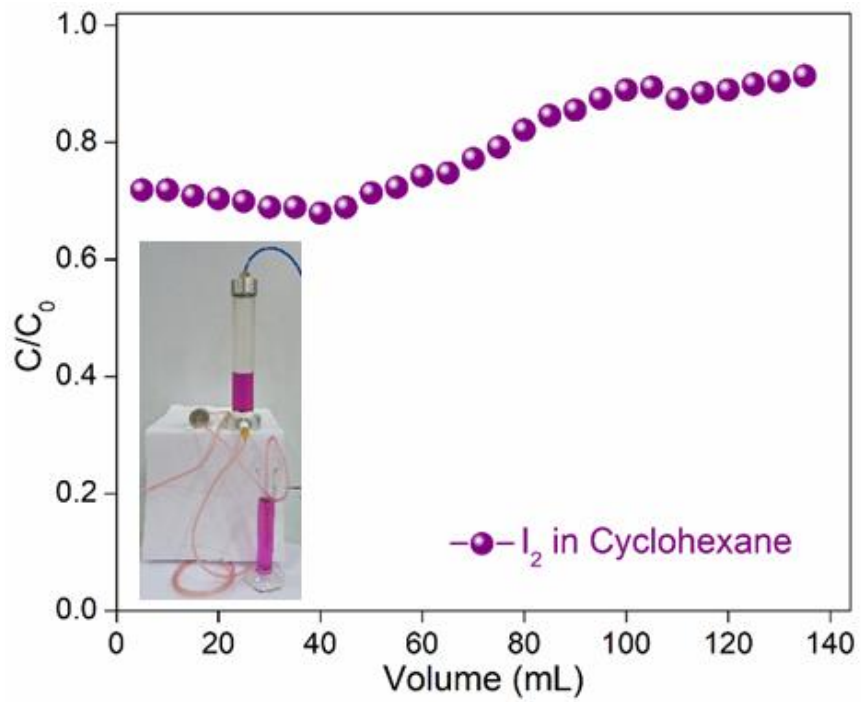
Figure S89: Result of dynamic I_2 capture test in cyclohexane using COF-2-membrane.
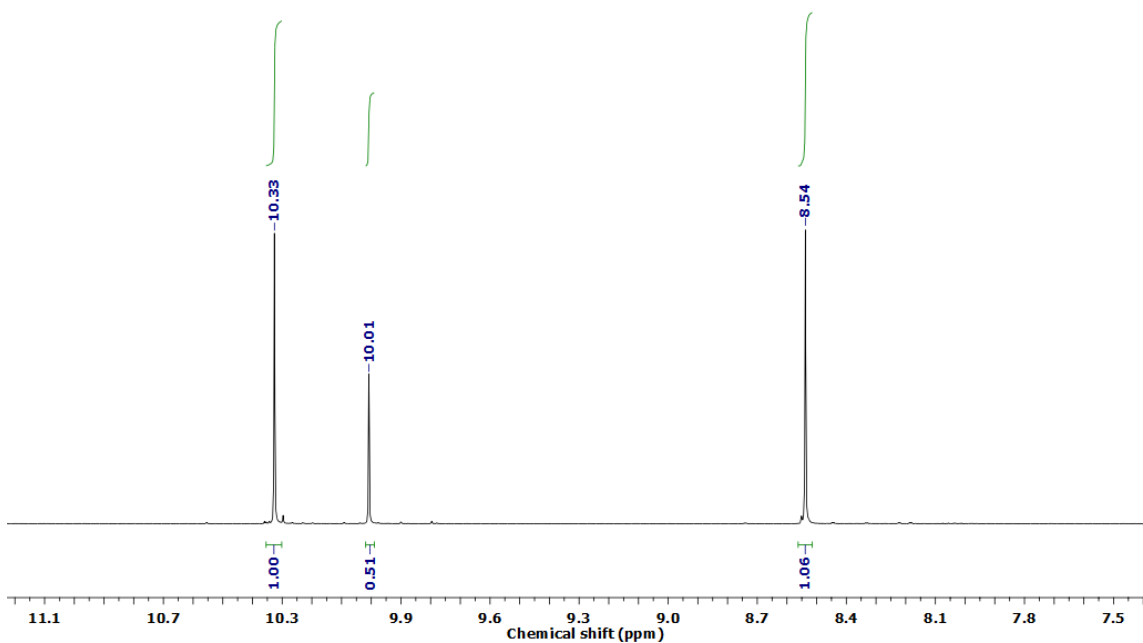
Figure S90: ^{1}H NMR spectrum of 2-hydroxybenzene-1,3,5-tricarbaldehyde (1-OH).
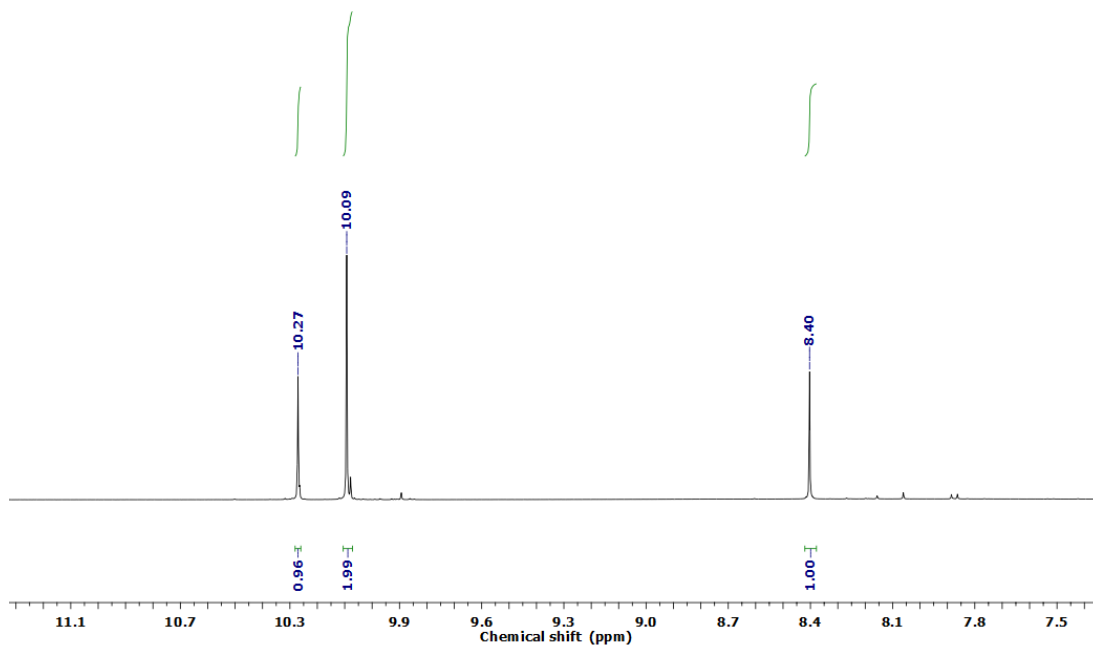
Figure S91: ^{1}H NMR spectrum of 2,4-dihydroxybenzene-1,3,5-tricarbaldehyde (2-OH).
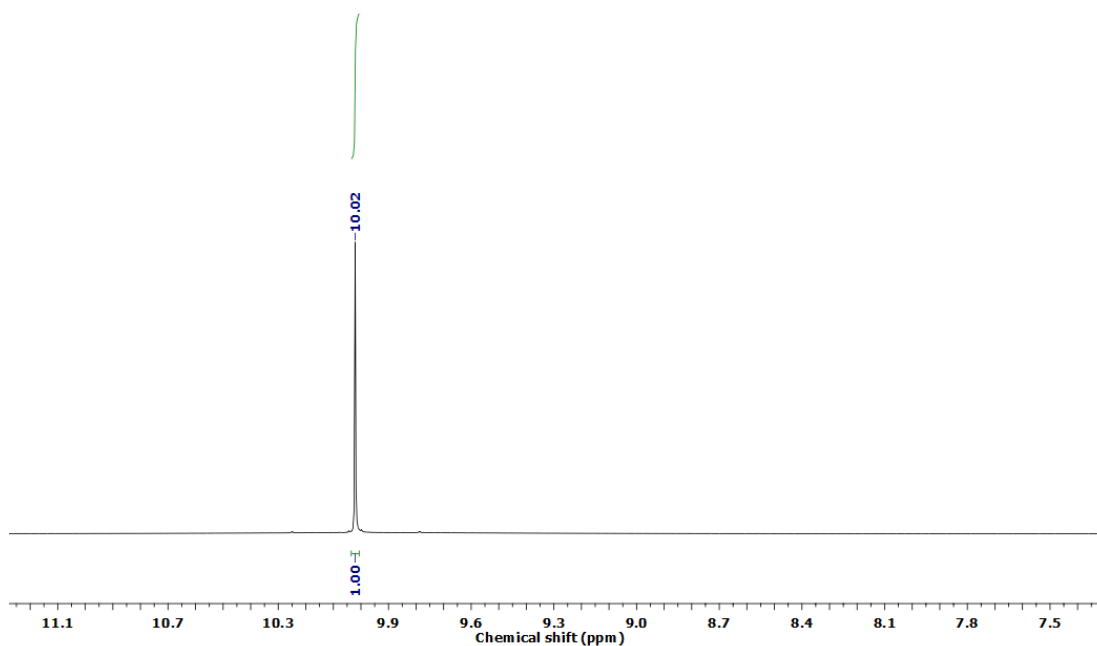
Figure S92: [^1]H NMR spectrum of 2,4,6-trihydroxybenzene-1,3,5-tricarbaldehyde (3-OH).
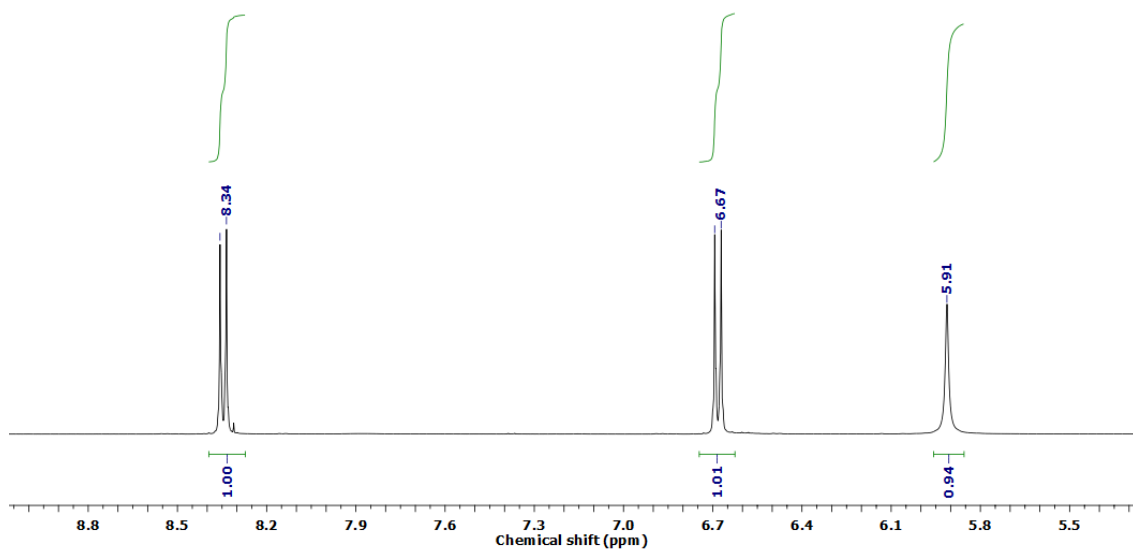
Figure S93: [^1]H NMR spectrum of 4,4',4"-(1,3,5-triazine-2,4,6-triyl)trianiline.

Section S11: References

[1] H. Wang, C. Qian, J. Liu, Y. Zeng, D. Wang, W. Zhou, L. Gu, H. Wu, G. Liu, Y. Zhao. *J. Am. Chem. Soc.* 2020, **142**, 4862−4871.

[2] K. Dey, M. Pal, K. C. Rout, S. Kunjattu, A. Das, R. Mukherjee, U. K. Kharul, R. Banerjee. *J. Am. Chem. Soc.* 2017, **139**, 13083−13091.

[3] S. Ruidas, A. Das, S. Kumar, S. Dalapati, U. Manna, A. Bhaumik. *Angew. Chem. Int. Ed.* 2022, **61**, e202210507.

[4] Y. Chen, X. Luo, J. Zhang, L. Hu, T. Xu, W. Li, L. Chen, M. Shen, S.-B. Ren, D.-M. Han, G.-H. Ning, D. Li. *J. Mater. Chem. A*, 2022, **10**, 24620–24627.

[5] F. Chu, G. Hai, D. Zhao, S. Liu, Y. Hu, G. Zhao, B. Peng, G. Wang, X. Huang. *ACS Catal.* 2023, **13**, 13167−13180.

[6] S. Kandambeth, K. Dey, R. Banerjee. *J. Am. Chem. Soc.* 2019, **141**, 1807– 1822.

[7] S. Kandambeth, A. Mallick, B. Lukose, M. V. Mane, T. Heine, R. Banerjee. *J. Am. Chem. Soc.* 2012, 134, 19524−19527.

[8] Y. Xie, T. Pan, Q. Lei, C. Chen, X. Dong, Y. Yuan, J. Shen, Y. Cai, C. Zhou, I. Pinnau, Y. Han. *Angew. Chem. Int., Ed.*, 2021, **60**, 22432–22440.

[9] Q. Song, W. D. Wang, X. Hu, Z. Dong, *Nanoscale*, 2019, **11**, 21513–21521.

[10] C. A. Coulson, G. N. Robertson. *Proc. R. Soc. London Ser. A*, 1975, **342**, 289–315.

[11] G. R. Satyanarayana, D. B. K. Kumar, K. Sujatha. *J. Mol. Liq.,* 2016, **216**, 526–537.

[12] Y. Li, Q. Wu, X. Guo, M. Zhang, B. Chen, G. Wei, X. Li, X. Li, S. Li, L. Ma. *Nat. Commun.* 2020, **11**, 599.

[13] S. Lee, I. Kevlishvili, H. J. Kulik, H.-T. Kim, Y. G. Chung and D.-Y. Koh, *J. Mater. Chem. A.*, 2022, **10**, 24802 —24812.

[14] A. L. Aguiar, E. B. Barros, V. P. Sousa Filho, H. Terrones, V. Meunier, D. Machon, Y. A. Kim, H. Muramatsu, M. Endo, F. Baudelet, A. San-Miguel and A. G. Souza Filho, *J. Phys. Chem. C*, 2017, **121**, 10609–10619.

[15] G. M. do Nascimento, T. Hou, Y. A. Kim, H. Muramatsu, T. Hayashi, M. Endo, N. Akuzawa and M. S. Dresselhaus. *Nano Lett.*, 2008, **8**, 4168–4172.

[16] X. Chen, M. A. Rickard, J. W. Hull Jr, C. Zheng, A. Leugers and P. Simoncic. *Inorg. Chem.*, 2010, **49**, 8684–8689.

[17] BIOVIA, Dassault Systèmes, [Discovery Studio], [V16.1.0.15350], San Diego: Dassault Systèmes, [2017].

[18] M. M. Shirolkar, R. Athavale, S. Ravindran, V. Rale, A. Kulkarni, R. Deokar. *Nano-Structures & Nano-Objects*, 2021, **25**, 100657.